



Pyrolysis of *hyphaene thebaica* shell over ceramic tile dust-derived catalysts and assessment of the produced bio-oil

Habu Iyodo Mohammed^{a,c}, Kabir Garba^{a,*}, Saeed I. Ahmed^a, Lawan G. Abubakar^b

^a Department of Chemical Engineering, Abubakar Tafawa Balewa University, P.M.B 0248, Bauchi, Nigeria

^b Department of Agricultural and Bioresource Engineering, Abubakar Tafawa Balewa University, P.M.B 0248, Bauchi, Nigeria

^c Department of Chemical Engineering, University of Maiduguri, P.M.B 1069, Maiduguri, Nigeria

ARTICLE INFO

Keywords:

Bio-oil
Catalysts
Coking
Hyphaene thebaica shell
Pyrolysis
ZSM-5 zeolite

ABSTRACT

The purpose of this study is to demonstrate the potential of ceramic tile dust (CTD)-derived ZSM-5 zeolite (CZ) and its monodispersed composite with metal oxides (MgO and Fe₂O₃) in the catalytic pyrolysis of *hyphaene thebaica* shell (HTS). The HTS was pyrolysed in a Fixed-bed reactor at 400–600 °C, and 100–300 mL/min N₂ flowrate. The maximum bio-oil production of 32 % was obtained at 500 °C and 150 mL/min N₂ flowrate, with bio-oils containing 50 % acid and octadecenoic acids, as well as esters, phenols, aldehydes, ketones, ethers, aromatics, and hydrocarbons. A carboxymethyl cellulose templating agent was employed for the mesoporous zeolite synthesis from CTD. This resulted in the mesoporous zeolite with a predominant ZSM-5 crystal phase, exhibiting pore diameters ranging from 1.8–6 nm, 229 m²/g surface area and 1145 μmol/g total acidity. The catalytic pyrolysis of HTS was conducted using the ZSM-5 zeolite (CZ) and metal-oxide (MgO, Fe₂O₃, and Fe₂O₃/FeO) modified CZ, as monodispersed composite catalysts. Under best thermal pyrolysis conditions, CZ-Fe₂O₃, CZ-MgO, and CZ-Fe₂O₃/MgO demonstrated 22–23 % bio-oil yields. Notably, the CZ-Fe₂O₃/MgO catalyst exhibited the highest hydrocarbon yield at 16 %, while the CZ-MgO favoured the production of phenolics, esters, and alcohols. CZ-MgO also displayed the highest coking level at 7.5 %, indicating faster deactivation than the other catalysts. The synthesised catalysts exhibited remarkable catalytic activity, resulting in a notable improvement in the quality of bio-oils obtained from the intermediate pyrolysis of *hyphaene thebaica* shells in a fixed-bed reactor.

Introduction

Concerns about the depletion of fossil fuels and greenhouse gas emissions have increased, as has interest in nontraditional fuel systems based on bio-renewable resources such as lignocellulosic materials. The global energy policy promotes net-zero carbon emissions by 2050. Currently, there is a significant gap between deployment and target. The requirement to attain this goal has prompted research into renewable energy production. In contrast to other thermochemical processes such as hydrothermal, gasification, and incineration, pyrolysis served as a viable technique for biomass conversion to high-value renewable energy precursors. Pyrolysis is characterised as slow, intermediate, fast, or flash (Šimáček et al., 2017). Hard-shell of *canarium schweinfurthii* fruit (Garba et al., 2023) sugarcane bagasse (Saif et al., 2020; Stegen and Kaporaju, 2020) and *hyphaene thebaica* shell (HTS) (Mohammed et al., 2022) are being researched for their pyrolysis potential in producing renewable resources such as bio-oil. Biomass can be converted into high-quality

bioenergy precursors based on their chemical composition using pyrolysis reactors. The biomass decomposition behaviours and process variables such as reaction temperature, heating rate, nitrogen flow rate, and pressure influence the distribution and yield of pyrolysis products (Gao et al., 2016; Uddin et al., 2018).

Different types of pyrolysis lead to product distributions and can even change the composition of the end products (Safdari et al., 2019). Slow pyrolysis generates more biochar and operates at low temperatures with a long residence time for vapours, fast pyrolysis produces more bio-oil and is conducted at 500 °C with a short residence time and a heating rate that exceeds 200 °C/s. Flash pyrolysis produces more gaseous products, but the reaction time is brief and the heating rate is higher, up to 1000 °C/s (Lee et al., 2019). Intermediate pyrolysis is preferred due to its balanced product distribution and high bio-oil yield.

Numerous authors (Zaman et al., 2018; El-Sayed and Khairy, 2015; Zinchik et al., 2018) have previously investigated how process conditions impact the bio-oil yield from various biomass species. Temperature

* Corresponding author at: Department of Chemical Engineering, Abubakar Tafawa Balewa University, P.M.B 0248, Bauchi, Nigeria.

E-mail addresses: gkabar@atbu.edu.ng, kbgarba.1214@gmail.com (K. Garba).

and heating rate are the significant factors that influence the composition and yield of bio-oil (El-Sayed and Khairy, 2015). Many studies have explored how pyrolysis temperature and heating rate affect bio-oil composition (El-Sayed and Khairy, 2015; Waluyo et al., 2018). One study (Aguilar et al., 2015) examined the effects of pyrolysis temperature on the yield of bio-oil from coconut shells. They found that a temperature of 575 °C, a heating rate of 20 °C/min, and a particle size of 5 mm produced the maximum bio-oil yield of 75.74 wt% (which includes water). Another study (Hani and Hailat, 2016) reported a bio-oil yield of 42.28 % at 500 °C, with a heating rate of 100 °C/min and a particle size of 91–106 µm for the pyrolysis of an empty oil palm fruit bunch. In a study by Li et al. (2019), the impact of temperature and heating rate on the pyrolysis of corn stalks was examined at a range from 400 to 600 °C. By heating at a rate of 20 °C/min, the highest bio-oil yield of 37.1 % was achieved at 550 °C. Wu et al. (2020) also explored the temperature and heat rate effects on the pyrolysis of corn stover-polypropylene blend and pulp residue. The research analysed temperature variations from 450 to 650 °C, with the maximum bio-oil yield of 44.8 % being obtained at 550 °C. The temperature at which the highest bio-oil yield is generated varies with the biomass type due to differences in their compositions. Therefore, examining the effects of operational conditions on the yield and composition of bio-oil from HTS is pertinent.

Furthermore, catalysts have been identified as key to producing high-grade bio-oil and bio-chemical precursors (Dutta et al., 2018; Kabir et al., 2017). Catalysts facilitate secondary reactions such as depolymerisation, deoxygenation, hydrogenation of unsaturated bonding, coupling, and cracking of C–C bonds, and branching (Dawes et al., 2015). Several authors (Naqvi and Naqvi, 2017; Na et al., 2018) have investigated the performance of several zeolite-based catalysts. The zeolite-based catalysts were reported to be the most effective for upgrading pyrolysis vapour to high-grade bio-oil (Zheng et al., 2017). A comparison of efficacy among zeolite base catalysts such as Zeolite Socony Mobil-5 (ZSM-5), Santa Barbara Amorphous-15 (SBA-15), Institute de Technologie Quinzi-2 (ITQ-2), MCM, Mesoporous cellular Foam (MCF), and Mesoporous Nano-materials (MSN) was conducted by Naqvi et al. (2015). ZSM-5-based catalysts perform better in upgrading pyrolysis vapour. ZSM-5/Fe₂O₃ composite performs even better (Na et al., 2018; Mohabeer et al., 2019). Despite the enhanced performance of ZSM-5 base catalysts in upgrading biomass pyrolysis vapour, they are characterised by a short life on stream.

Researchers (Liu et al., 2014; Zheng et al., 2020) have developed composite catalysts to improve the performance of bulk zeolite in biomass pyrolysis. These catalysts are formulated to overcome the coking issue and provide superior catalytic performance (Özçakar and Karaduman, 2021). By combining metallic oxide and zeolite, their synergistic effects can enhance the overall catalytic performance.

Investigators (Wibowo et al., 2023; Kholkina et al., 2019) have been exploring ways to produce bio-oil at a lower cost by using waste and less expensive biomass and catalyst precursors. One current trend is to use waste or less valuable resources to create value-added downstream precursors. Ceramic tile dust (CTD) and iron ore dust (IOD) are particulate residues generated during the ceramic tile and iron ore processing. Some studies showed that the blast and electric furnace slag-rich zeolite and iron materials were effective catalysts in biomass pyrolysis by improving the bio-oil value (Kholkina et al., 2019; Nasuha et al., 2017). By combining CTD-derived zeolite with IOD-derived Fe₂O₃ and MgO, cheaper and higher-value catalysts for biomass catalytic pyrolysis can potentially be synthesised. Therefore, further investigation is needed to determine their catalytic performance in the pyrolysis of HTS.

The study aims to repurpose ceramic tile dust (CTD), iron ore dust (IOD), and other metal oxide (MgO) as raw materials for producing zeolite ZSM-5 from CTD and metal-oxide-modified ZSM-5 to serve as catalysts to enhance the quality of bio-oils obtained from the intermediate pyrolysis of *Hyphaene thebaica* shells in a fixed-bed reactor. The ultimate goal is to produce sustainable, renewable energy and chemicals.

Materials and methods

Preparation characterisation of *hyphaene thebaica* shell for pyrolysis

The *hyphaene thebaica* shell (HTS) was supplied from a market in Borno State Nigeria. The endocarp-free HTS nut was cracked to separate the kernel from the shell. After sun-drying, the HTS nut was crushed to an average diameter of 10 mm, and ground in an attrition grinding machine. The grinder is a five-horsepower electric motor attrition grinder manufactured by the University Centre of Industrial Studies in Nigeria and then sieved to achieve a range of particle sizes. The HTS particles that passed through a 300-µm sieve were oven-dried at 105 °C for 24 h and stored in an airtight container for characterisation, pre-treatment, and pyrolysis studies.

Extensive characterisation of HTS for bio-oil production via pyrolysis was pioneered in the literature (Mohammed et al., 2022). The CHNS/O and proximate analysis of the sample used in this study was conducted.

Preparation of ceramic tile dust for ZSM-5 zeolite synthesis

The CTD was collected from a tile production site in Bauchi State, Nigeria, thoroughly washed, oven-dried at 105 °C until a constant weight was achieved, and then stored in a desiccator. Rigaku NEX DE EDXRF with Rigaku RPF-SQX software characterise the dried CTD sample using X-ray fluorescence. The inorganic metal oxide compositions of the CTD for the zeolite catalyst synthesis precursor were determined.

Synthesis of ZSM-5 zeolite from ceramic tile dust

A precise 16.56 g of silica gel beads (Qingdao Haiyang Chemical Co., Ltd., China, analytical grade) were mixed with 15 ml of deionised water and 20 g of NaOH. The mixture was heated to 90 °C while being stirred until beads formed a gel. About 30 g of CTD and 20 g of NaOH were mixed thoroughly in 15 ml of distilled water until a suspension was produced. The silica gel and CTD suspension were mixed and stirred for 30 min. Following the preparation of the suspensions, the two halves were mixed and subjected to mechanical stirring with a magnetic stirrer. This was followed by 48 h of agitation. The silica gel and CTD suspension mass ratio have a 5:4 and 30Si/Al ratio.

The carboxymethylcellulose (CMC) at a CMC/SiO₂ ratio of 0.3 equivalent to 15 g was prepared and used as a templating agent in the CTD-derived ZSM-5 (CZ) zeolite synthesis. The pH of the gel obtained from the formulation was adjusted in the range of 11–12. The mixture of the gels was transferred into an autoclave lined with Teflon. The autoclave containing the gel was placed in an oven, set to 180 °C, and allowed to react for 24 h. The crystals formed were washed until neutrality was achieved. The crystals obtained were calcined at 550 °C for 6 h, refluxed with 1 M of ammonia solution at 90 °C for 2 h, dried in an oven, and stored in a desiccator.

Furthermore, reagent-grade nanosized Fe₂O₃ and MgO respectively synthesised from IOD (see composition in Table 1) and Mg(NO₃)₂·6H₂O were dispersed in CZ to form monodispersed composite catalysts. The composites of CZ-Fe₂O₃ (CZ-F), CZ-MgO (CZ-M), and CZ-Fe₂O₃-MgO (CZ-FM) in equal proportion, formed the monodispersed composite catalysts. The catalysts were stored in an airtight container and desiccated for characterisation and HTS catalytic pyrolysis.

Table 1
XRF compositions of Iron ore dust (IOD).

Compounds	SiO ₂	Al ₂ O ₃	Fe ₂ O ₃	CaO	MgO	Others	Total
	wt.% (Dry basis)						
IOD	1.05	2.31	81.81	0.53	0.01	14.29	100
Precipitated Fe ₂ O ₃	0.02	0.03	99.91	0.02	0.00	0.02	100

Characterisation of the ceramic tile dust derived ZSM-5 zeolite

Several methods were used to examine the properties of the CTD-derived ZSM-5 (CZ) zeolite. The morphology and elemental composition were determined using Zeiss and Phenom-World scanning electron microscopy/electron dispersive (SEM/EDX) techniques. The surface functional groups and fingerprints were examined using Fourier transform infrared (FTIR) spectroscopy on a PerkinElmer Spectrum 100. X-ray diffraction spectroscopy (XRD) was used on a PANalytical/Rigaku software diffractometer to determine the crystal structure and phase of the CZ, and the results were compared to standard data in the International Zeolite Association database. The acid sites on the CZ zeolite were investigated using ammonia temperature-programmed desorption (NH₃-TPD) and in situ diffuse reflectance infrared Fourier transform spectroscopy of pyridine adsorption (pyridine DRIFTS). The surface area and pore dispersion were determined using nitrogen adsorption-desorption tests on the Horiba SA-9600.

Thermal pyrolysis of *hyphaene thebaica* shell

The pyrolysis of HTS (sieved through 250–500 µm mesh) was conducted in a vertical fixed-bed reactor (50 cm length, 2.2 cm diameter) enclosed by an electric furnace using heating elements capable of reaching temperatures up to 1300 °C. The reactor is cylindrical and made of stainless steel, equipped with a K-type thermocouple connected to an Omron controller for monitoring and controlling the temperature. The pyrolysis rig is presented in Fig. 1.

The reactor was fed with about 10 g of HTS powder and heated electrically at a rate of 2 °C/s to 500 °C under a N₂ gas flow rate of 250 mL/min for 30 min, during which no significant release of non-condensable gas (py-gas) was observed. The pyrolysis experiment was repeated at 450, 500, and 550 °C. The experiment was conducted at 500 °C with N₂ flow rates of 100, 150, 200, and 300 mL/min. The resulting pyrolysis vapour was condensed in a condenser operating under icy conditions. The bio-oil and biochar were collected at the end of each experiment after the reactor had cooled to room temperature. They were then weighed, and the bio-oil was characterised. The pyrolysis gas (py-gas) yield was calculated from the biochar and liquid yields using Equation (3), while the yields of other components were evaluated using Equations (1) and (2). The composition of the bio-oil obtained was

examined through gas chromatography and mass spectrometry (GC-MS).

$$Y_{char} = \frac{W_{char}}{W_s} \times 100 \quad (1)$$

$$Y_{bio-oil} = \frac{W_{bio-oil}}{W_s} \times 100 \quad (2)$$

$$Y_{gases} = 100 - Y_{char} - Y_{bio-oil} \quad (3)$$

where W_{char} (g) and $W_{bio-oil}$ (g), are the weight of various products recovered, and Y_i (%) are yields of the corresponding products. W_s (g) is the weight of the solid biomass.

Catalytic pyrolysis of *hyphaene thebaica* shell

The HTS was pyrolysed in a fixed-bed reactor enclosed in an electrical heating furnace, as depicted in Fig. 1. The catalytic pyrolysis experiments employed 10 g of HTS and CZ (sieved through a 0.63 µm mesh) at a mass ratio of 10:1. In a typical catalytic pyrolysis experiment, CZ was introduced into the reactor before 10 g of HTS, resulting in a two-layered bed. To create an inert atmosphere, N₂ was charged into the reactor for 15 min before heating the two-layered bed of HTS and CZ to the required pyrolysis reaction temperature and maintaining it for 30 min. The pyrolysis vapour produced by the decomposition of HTS flowed constantly through the CZ bed and into a condenser maintained at −5 °C, with nitrogen used as a sweeping gas. The condenser used two liquid collectors connected in series to condense the vapours into bio-oil, while non-condensable gases were discharged into the atmosphere. At the end of each experiment, the heating was turned off while the reactor was allowed to cool to ambient temperature with a constant supply of N₂ gas to maintain the reactor's inert condition. The bio-oil, biochar, and py-gas produced during pyrolysis were measured and analysed after each experiment. The chemical composition of the resulting bio-oil was evaluated using gas chromatography-mass spectrometry (GC-MS).

Furthermore, HTS pyrolysis experiments were carried out concurrently within the pyrolysis reactor using metal oxide-modified CZ.

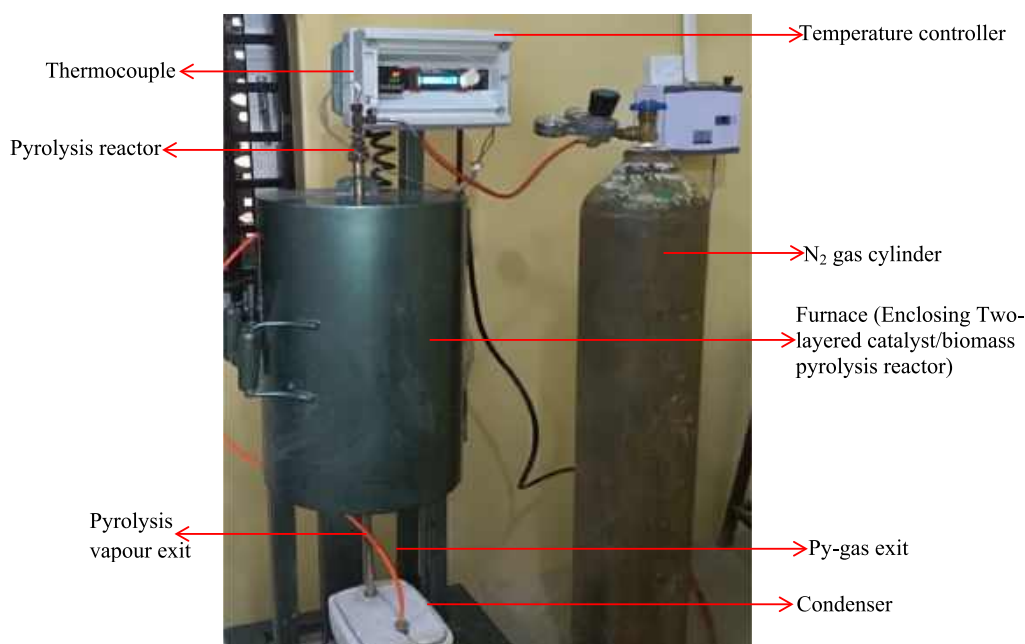


Fig. 1. Pyrolysis rig for pyrolysis of *hyphaene thebaica* shell.

Characterisation of hyphaene thebaica shell bio-oil

Some selected bio-oils derived from the pyrolysis of HTS were characterised using methods reported by Kabir et al. (2022). The chemical compositions of the resultant bio-oils were determined using a gas chromatograph-mass spectrometer (GC–MS) system, an Agilent 8890 GC and 5977 MSD equipped with the NIST-EPA_NIH-2014 library. The bio-oil sample was dissolved in acetone at a 1:10 ratio and centrifuged before analysis. The prepared bio-oil solution was injected into the GC injection port maintained at 160 °C and a split ratio of 6:1 by an in-built GC program. A fused-silica-glass HP-INNOWAX capillary column with helium serving as carrier gas was employed to separate the bio-oil vapour into different compounds for the GC–MS analysis. The quantity of each compound was determined by matching retention time and mass spectral data with the authentic standards of the National Institute of Standards and Technology (NIST) present in a PC database system. The identification process was based on spectrum peaks and followed the standard mass spectrum library of the NIST. The bio-oil compositions were presented as a percentage of the total peak area under the GC chromatogram. Furthermore, an FTIR spectrometer (Cary 400, Agilent) was employed to examine the functional groups and fingerprints of the bio-oil compounds derived from HTS pyrolysis.

The ultimate analysis of the HTS bio-oils was performed on a Perkin-Elmer CHNS/O analyzer model 2400 Series. The HHV and degree of deoxygenation (DOD) were obtained from CHNS/O data using Eqs. (4) and (5), respectively.

$$DOD = \frac{[O]_{HTS} - [O]_{bio-oil}}{[O]_{HTS}} \times 100 \tag{4}$$

$$HHV[33] \left(\frac{MJ}{kg} \right) = -1.3675 + (0.3137 \times \%C + 0.7009 \times \%H + 0.0318 \times \%O) \tag{5}$$

Results and Discussions

The results of the proximate, ultimate analysis of HTS and ash elemental composition of HTS are presented in Table 2.

The HTS has volatile matters of 74.31 %, and ash content of 8.753 %. The volatile matter is a combination of bio-oil and non-condensable gases. The high volatile matter and low ash content signify the great potential of HTS as feedstock for bio-oil production (Mohammed et al., 2022).

X-ray fluorescence composition of ceramic tile dust

Silica and alumina compositions are required to serve as a precursor for zeolite preparation (Aguilar-Mamani et al., 2014). Table 3 compares

Table 2
Proximate and ultimate analysis of hyphaene thebaica shell (Mohammed et al., 2022).

Parameters	Value
Proximate (wt.%)	
Moisture content	4.97
Volatile matters	74.31
Fixed carbon	11.96
Ash content	8.75
Ultimate Analysis (wt.%)	
Carbon	42.52
Hydrogen	5.50
Nitrogen	0.55
Sulphur	1.17
Oxygen	50.26
O/C Molar ratio	0.89
H/C Molar ratio	1.55

Table 3
Ceramic tile dust (CTD) chemical composition from XRF analysis.

Metal oxides	Composition (wt%)	
	CTD (This study)	Kaolin (Krisnandi et al., 2019)
SiO ₂	74.80	55.0
Al ₂ O ₃	12.40	35.2
Na ₂ O	5.44	0.36
K ₂ O	4.60	1.18
MgO	0.21	0.21
CaO	1.27	0.66
Fe ₂ O ₃	0.83	0.82
TiO ₂	0.11	0.08
MnO	0.02	—
P ₂ O ₅	0.11	—

the chemical composition of the CTD from XRF analysis to kaolin, which was used for zeolite synthesis. The CTD is high in silica and low in alumina and can be used to synthesise various zeolites.

FTIR analyses of CTD and CTD-derived zeolite

Fig. 2 shows the FTIR spectra of CTD and CTD-derived zeolite (CZ). The smoothness of the spectrum indicates a three-dimensional framework. The intensity of the CTD spectrum differs from that of CZ, which revealed the changes caused by reactions promoted by the hydrothermal treatment. The variation in dipole moment regarding distance and the interaction of unit cells with their surroundings caused the changes in intensity and band. The CZ interacts more with the unit cells around it, whereas the CTD has fewer interactions.

The presence of two or more peaks indicates the presence of crystals. The internal vibration of the tetrahedral Si-O-Al asymmetric stretching is shown by the first peak at 808–1237 cm⁻¹. The symmetrical stretch of Si-O-Si or Al-O-Al, which corresponds to the double ring vibration from the framework of the MFI-type zeolite, causes the second peak at 700 cm⁻¹ (Mozgawa et al., 2011). This relates to a characteristic property of zeolite with a three-dimensional framework in which two tetrahedral shared oxygen molecules. The vibration of external linkages in unit cells resulted in the peak around 650 cm⁻¹ band. The 1050–1150 cm⁻¹ band corresponds to a pore opening (Karge, 2001). These are required for zeolites to have a framework structure and interconnected cavities occupied by cations and water molecules.

Morphology of CTD-derived ZSM-5 zeolite

Fig. 3 shows an SEM image of a 4000x magnification of the CTD-derived zeolite (CZ). Spherical sponge-like particles characterise the morphology with a highly porous surface and an intra-pore network. The findings are consistent with those published in the literature (Yunusa et al., 2020; Ding et al., 2015). The consistency in the morphology of the synthesised zeolite from the CTD indicates excellent crystallisation. The polycrystalline particles consist of tiny primary crystals tightly packed together.

Table 4 displays the composition of the CZ using EDX. Also, the compositional spectra are presented in Fig. S1 as supplementary. Silicon, aluminium, and sodium are the main constituents of zeolite materials. The components stem from the mineral compounds and ash precursors employed in the production of zeolites (Yue et al., 2015). The presence of these metals might give the zeolite multi-functionality, which is critical in most catalytic pyrolysis reactions. For instance, KCl and Cs play notable roles in the demethylation and demethoxylation of pyrolysis vapour, thereby increasing phenol content by removing the R group from the ring (Liu et al., 2017).

XRD analysis of CTD-derived ZSM-5 zeolite

Fig. 4 shows the XRD pattern for the CZ zeolite synthesised from CTD using CMC as a templating agent. The diffraction pattern exhibited primary peaks between 10° and 20° to 30°, corresponding to the described diffraction pattern for the ZSM-5 crystal phase (Yunusa et al.,

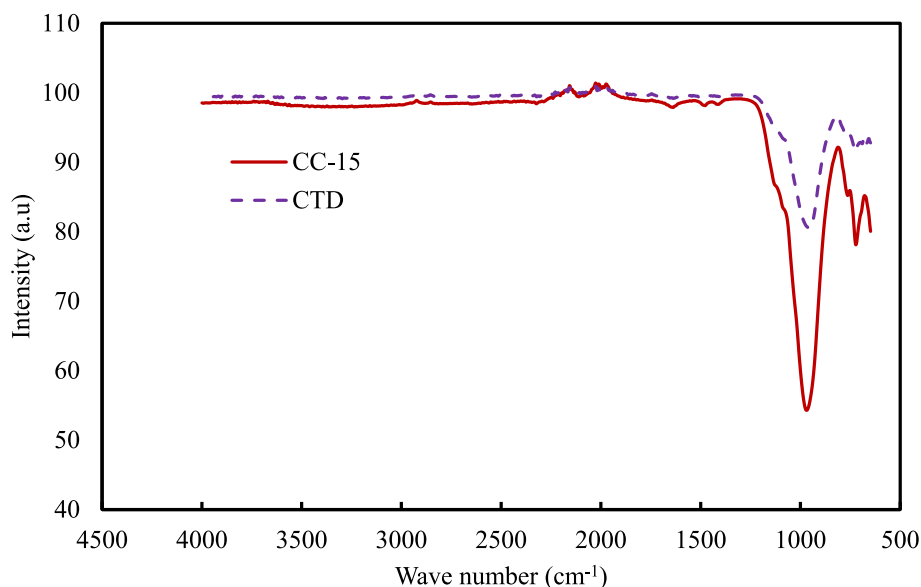


Fig. 2. FTIR of CTD and CTD-derived ZSM-5 zeolite.

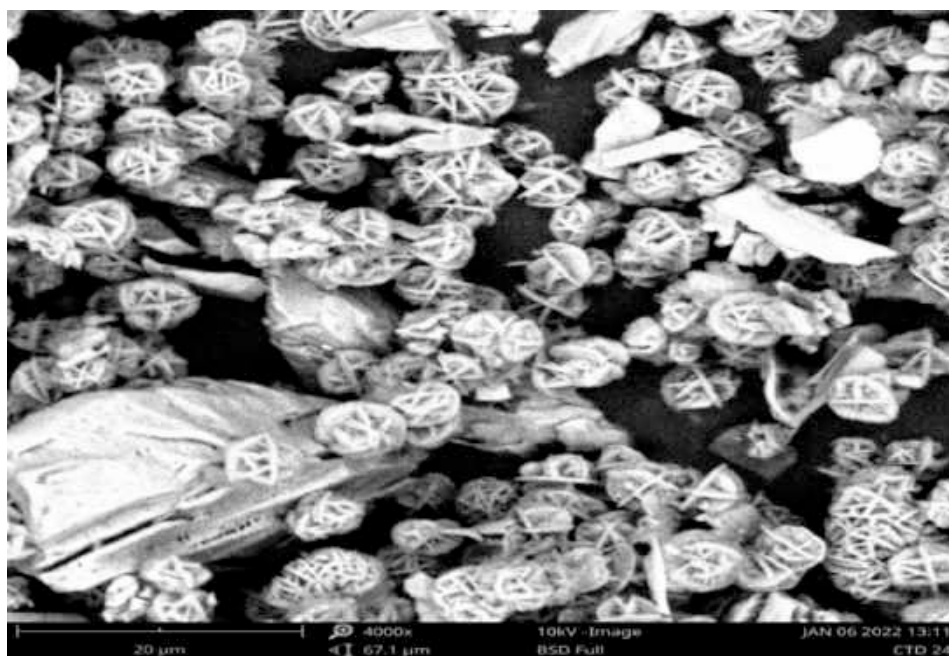


Fig. 3. SEM image of CTD-derived zeolite.

2020; Soltanali and Darian, 2018). This inferred that ZSM-5 (MFI-type zeolite) was synthesised from the CTD. Furthermore, the crystallite size and d-spacing determined using Scherrer and Bragg's methods is depicted in Fig. 5. The size of the CZ crystallite is associated with d-spacing, which ranges from 5 to 100 Å in the crystal system. This implies that CZ has a larger pore diameter demonstrating its ability to withstand various compounds produced during biomass pyrolysis.

Textural characteristics of CTD-derived ZSM-5

The textural characteristics were determined using the Brunauer-Emmett-Teller (BET), Barrett-Joyner-Halenda (BJH), Dubinin-Astakhov (DA), and Dubinin-Radushkevich (DR) methods. Fig. 6 (a) and (b) illustrate the N₂ adsorption-desorption isotherm and pore size distributions of CZ, respectively. Table 5 shows the pore diameter, pore volume, and specific surface area of CZ compared with reagent-grade

ZSM-5 zeolite (Smail et al., 2019) and that of ZSM-5 synthesised from Grahamstone Kaolin (Mohiuddin et al., 2016). The CZ exhibited a type IV isotherms (IUPAC system) and an H₂ hysteresis loop, which confirms its mesoporous nature as presented in Fig. 6 (b). The catalyst has a hierarchical micro-mesoporous structure (pore sizes range from 1.85 to 6.92 nm). The textural property confirmed the micro-mesopore category's dominance over micropores, indicating a hierarchical micro- and mesoporous zeolite material (Takahashi and Fuji, 2002). The BET-specific surface area was 229.1 m²/g, comparable to the 279 m²/g of reagent-grade ZSM-5 with a 23 Si/Al ratio (Smail et al., 2019). The low adsorption energy indicated that unstable compounds were on the catalyst's surface and that the reaction products were easily removed from the catalyst's surface.

Table 4
EDX composition of CTD-derived zeolite at different points.

ElementNumber	ElementSymbol	ElementName	Atomic Concentration	Weight Concentration
Point1				
14	Si	Silicon	51.46	53.38
13	Al	Aluminium	36.76	36.62
11	Na	Sodium	11.78	10.00
Point 2				
8	O	Oxygen	33.83	7.92
14	Si	Silicon	23.75	9.76
74	W	Tungsten	14.35	38.61
35	Br	Bromine	8.95	10.47
19	K	Potassium	7.84	4.49
95	Am	Americium	6.98	24.82
11	Na	Sodium	2.52	0.85
47	Ag	Silver	0.94	1.48
55	Cs	Caesium	0.83	1.62

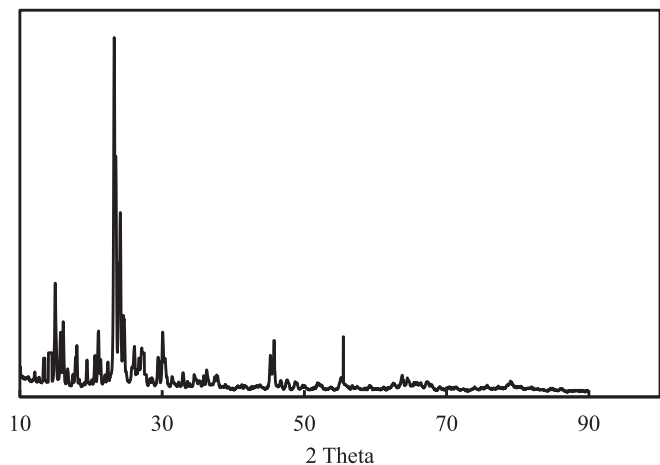


Fig. 4. XRD diffractogram of CTD-derived ZSM-5 zeolite.

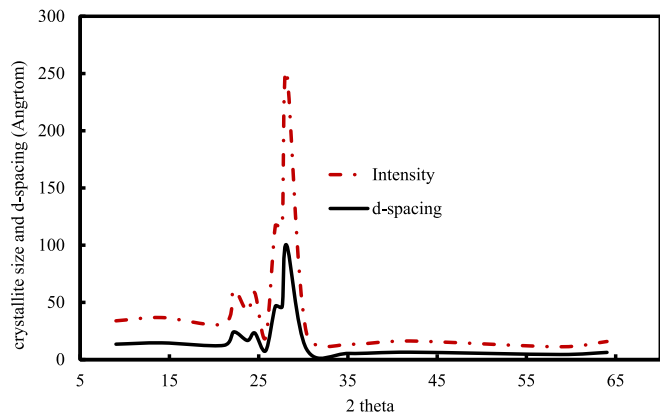


Fig. 5. Crystallite size and d-spacing of CTD-derived ZSM-5 zeolite.

NH₃-TPD pattern of CTD-derived ZSM-5 zeolite

Fig. 7 displays the NH₃-TPD pattern of the CZ zeolite. The pattern shows two distinct peaks at around 200 °C and 380 °C, corresponding to the desorption of physisorbed and chemisorbed NH₃. The peak observed at lower temperatures suggested the presence of weak acidic sites, whereas the peak at higher desorption temperatures indicated the presence of strong acidic sites. The CZ zeolite with a 30 Si/Al ratio has a total acidity of 1145 μmol/g and an acid site density of 3.11 μmol/m², determined by pyridine DRIFTS and NH₃ adsorption studies.

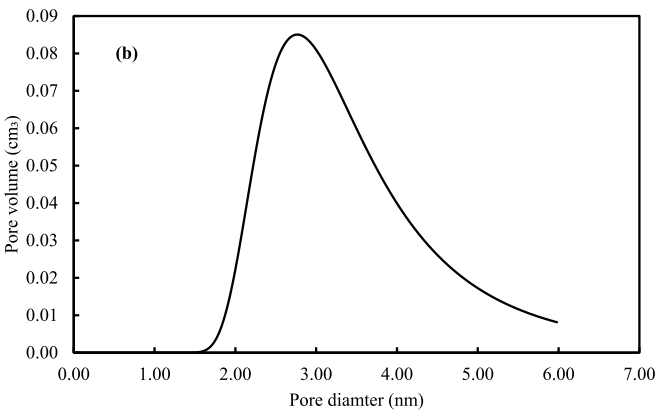
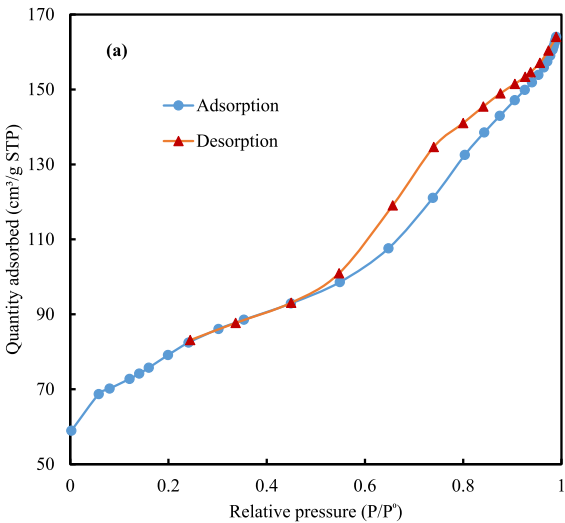


Fig. 6. (a) Adsorption-desorption isotherm and (b) pore distribution of CTD-derived ZSM-5 zeolite.

Product distributions of hyphaene thebaica shell pyrolysis

Product distribution for pyrolysis operating temperature and nitrogen flowrate conducted between 400 to 600 °C and 100 to 300 mL/min are presented in Figs. 8 and 9, respectively. There is no regular trend in bio-oil yield concerning temperature changes. The maximum bio-oil yield was 30 % at 500 °C, while the minimum yield of 18 % occurs at 600 °C. This conforms to the findings reported by some investigators (Lugovoy et al., 2019; Fermanelli et al., 2020). The maximum yield of bio-oil at 500 °C might be due to the

Table 5
Textural characteristics of CTD-derived ZSM-5 zeolite.

Parameters	CZ, ZSM-5 (This study)	Commercial ZSM-5 (S/A 23) (Smail et al., 2019)	Grahamstone kaolin ZSM-5 (Mohiuddin et al., 2016)
Specific surface area by multi-point BET (m^2/g)	229.1	279	280
Total pore volume by BJH method (cm^3/g)	0.1507	0.18	0.16
BJH mesopore diameter (nm) (Average)	5.50	1.7	4.9
DR mesopore diameter (nm) (maximum)	6.93	—	—
DA micropore diameter (nm) (Minimum)	2.76	—	—
DA adsorption energy (kJ/mol)	0.91	—	—
DR adsorption energy (kJ/mol)	3.75	—	—

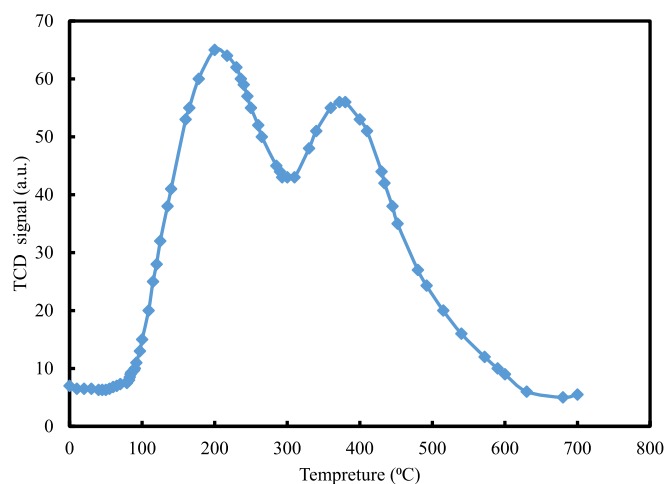


Fig. 7. NH_3 -TPD of CTD-derived ZSM-5 zeolite.

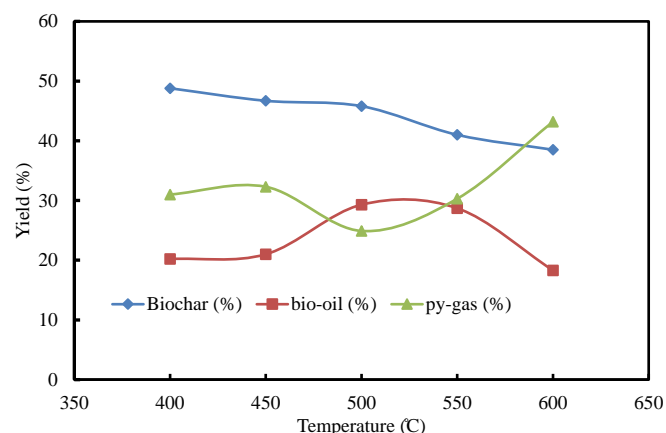


Fig. 8. Effect of temperature on *hyphaene thebaica* shell pyrolysis product distribution.

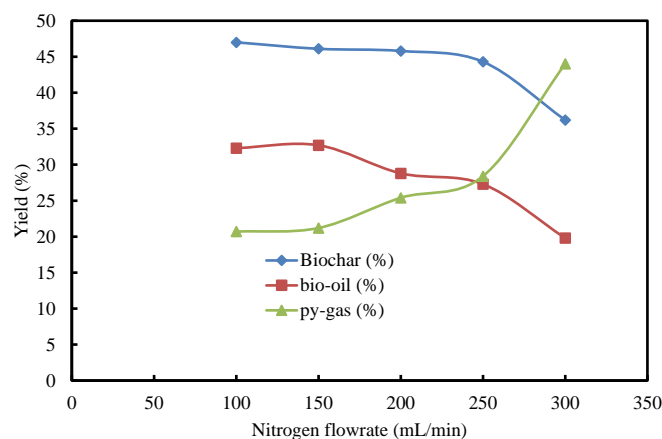


Fig. 9. Effect of nitrogen flowrate on *hyphaene thebaica* shell pyrolysis product distribution.

decomposition of the HTS macrostructure, and polymerisation of lighter components to form liquid products. The decrease in the liquid product at 600 °C might be due to the cracking of parts of the components that make up the liquid to non-condensable gaseous parts. The biochar decreases with an increase in the set operating temperature, while the py-gas decreases with an increase in temperature. This might be due to the decomposition of the macrostructure of the HTS and subsequent cracking of the vapour phase to non-condensable gases. Similar findings were reported in the literature (Li et al., 2019).

Furthermore, the effects of nitrogen flowrate on product distribution were investigated at 500 °C. Fig. 9 presents the findings of varying nitrogen flowrate from 100 to 300 mL/min on pyrolysis product distribution.

The bio-oil yield increased from 32.3–32.7 % with the increase in nitrogen flowrate from 100–150 mL/min. This may be attributed to the increasing pressure force that drives out the pyrolysis vapour into the condenser, which maximises condensation of the vapour phase to the liquid product (Wu et al., 2020). As the flowrate increases from 150–300 mL/min the bio-oil yield decreases to 19 %, while the gaseous product increases by 20–40 %. The continuous increase in the gaseous product may be attributed to the short residence time of the vapour phase in the condenser (Gao et al., 2016). On the other hand, the biochar decreases with an increase in flowrate. This might be attributed to the increasing sweeping pressure of the nitrogen gas, which removes the decomposed vapour phase from the solid components.

Effects of catalysts on product distribution on pyrolysis of *hyphaene thebaica* shell

The effect of CZ as ZSM-5 on the product distribution of HTS pyrolysis was also investigated. Also depicted, Fig. 10 compares the product yields from thermal and catalytic pyrolysis at 500 °C. The bio-char yield remained unchanged with the CZ catalyst. However, the bio-oil yield decreases from 32.7 to 22.3 %, and the py-gas increases from 21 to 30 %. These changes are due to secondary reactions such as cracking and decarboxylation caused by the catalysts, which convert heavier vapour components to non-condensable lighter ones. The findings conform to intermediate catalytic pyrolysis of palm kernel shell using a commercial zeolite catalyst (Waluyo et al., 2018).

The effects of nano- Fe_2O_3 and nano- MgO proportions monodispersed in the CZ zeolite as composite catalysts were also understood to affect the distribution of pyrolysis products. The bio-oil yield decreases and the py-gas yield increases substantially with an increase in the proportion of iron oxide in the catalyst's samples. The biochar yield decreases slightly when using composite catalysts. The presence of MgO also decreased the bio-oil yield, but not as iron ore dust. The CZ-F further reduces the bio-

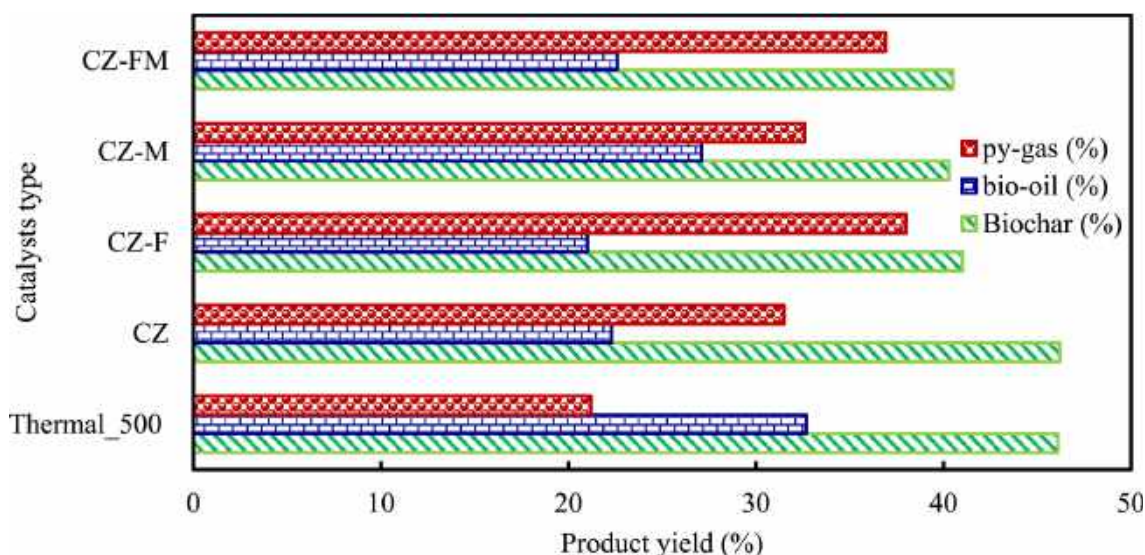


Fig. 10. Comparison of product distribution of HTS pyrolysis.

oil yield to 21 % and char to 41 %, while py-gas increases to 38 %. The bio-oil increased to 22.6 % from using CZ-FM, whereas the py-gas yield is 36.9 %. The bio-oil yield was 27 % when CZ-M catalysts were used. Secondary reactions of pyrolysis vapour, such as cracking, decarboxylation, decarbonylation, and hydrodeoxygenation, contribute to the increase in py-gas yield and decrease in bio-oil. Similar findings have already been reported by authors in the literature (Sanna and Andréßen, 2012).

Fig. 11 depicts the carbon balance of the HTS pyrolysis products, which is used to investigate the influence of various catalysts in HTS pyrolysis. The study found that the carbon content in the organic phase ranges from 25.30–26.50 %, py-gas from 36.50–40 %, and biochar from 18–19 %. Catalyst-assisted secondary reactions caused the carbon shift from organic and aqueous phases to py-gas. Consequently, the bio-oil contained 42–44.50 % of the carbon in the original feedstocks among the pyrolysis products. By comparison, catalytic pyrolysis bio-oils contain less carbon than non-catalytic bio-oils (HB-500). The bio-oil (HB-CZ-FM) produced by HTS pyrolysis using the CZ-FM catalyst had the lowest carbon content of 42 %, with 23 % and 19 % carbon in the organic and aqueous phases respectively. This suggests that the CZ-FM has higher catalytic activity than other catalysts, CZ, CZ-F, and CZ-M, due to the synergistic interaction of ZSM-5, Fe_2O_3 , and MgO with the pyrolysis vapour.

Characterisation of hyphaene thebaica shell bio-oils

The chemical compositions revealed by Fourier transform infrared (FTIR), GC/MS, and CHNS/O analyses are presented in the subsequent sections.

FTIR analyses of hyphaene thebaica shell bio-oils

The FTIR spectra of bio-oils produced through HTS thermal and catalytic pyrolysis are shown in Fig. 12. More peaks were visible during catalytic pyrolysis. This implies that the catalyst alters the reaction path. The bands are predominantly composed of functional groups for alcohol ($3570\text{--}3200\text{ cm}^{-1}$), carbonyl compounds such as esters, carboxylic acids ($1725\text{--}1700\text{ cm}^{-1}$), aromatics ($1615\text{--}1580\text{ cm}^{-1}$), alkane and alkene (Gibril et al., 2020; Asadieraghi and Daud, 2015). The FTIR peaks indicate the presence of a bonded hydroxyl group for thermal and catalytic reactions, suggesting an abundance of alcohol and phenols.

The peaks at 1513.3 , $1410\text{--}1310$, 1267.3 , and 1021 cm^{-1} for both bio-oil derived from thermal and catalytic pyrolysis of HTS indicate C—H bending vibration, Phenol, or tertiary alcohol OH bend, Aromatic ether, or aryl —O stretch, Primary amine, C—N stretch, respectively.

Distinct from the bio-oil, HB-500, derived from thermal pyrolysis at 500°C , the bio-oil, HB-CZ, derived from catalytic pyrolysis of HTS, has peaks at 3000 , 2929.7 , 1595.3 , 1699.7 cm^{-1} 752.9 , and 693.3 , which

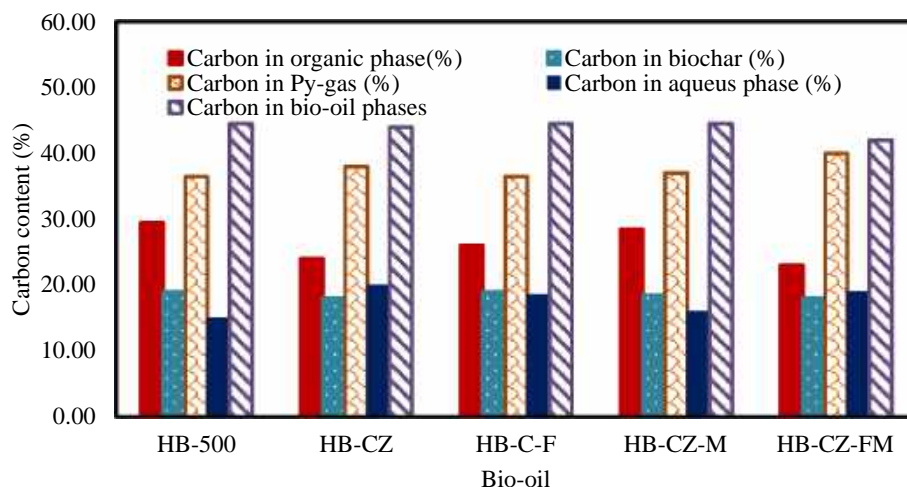


Fig. 11. Carbon balance of hyphaene thebaica shell pyrolysis products.

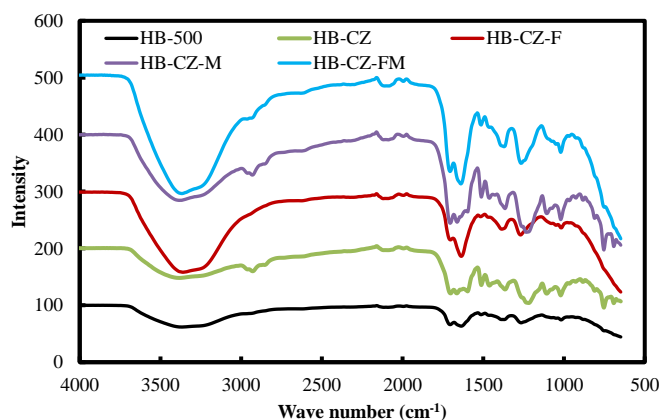


Fig. 12. FTIR of pyrolytic bio-oils from *hyphaene thebaica* shell.

correspond to C–H stretch, Methylene C–H asymmetric/symmetric stretch, secondary amine, >N–H bend, C–H aldehyde and ketone, C=O stretch, 2-Disubstitution (ortho substitution), Alcohol, and OH out-of-plane bend, respectively. The variation in bio-oil fingerprints could be attributed to secondary reactions helped by catalysts, such as cracking and esterification, which result in the synthesis of alkene Methylene C–H asymmetric/symmetric stretch. The spectra revealed the functional groups and distinctive bonds of the chemical groups found in HTS bio-oils. The FTIR shows several peaks, indicating the bio-oil's complexity. Table S1 shows the specific bands from FTIR spectroscopy related to functional groups and fingerprints of bio-oil chemical structure. The spectra illustrate how the catalysts change the reaction route. The bands are predominantly composed of functional groups for alcohol (3570–3200 cm^{-1}), carbonyl compounds such as esters, carboxylic acids (1725–1700 cm^{-1}), aromatics (1615–1580 cm^{-1}), alkane and alkene (Gibril et al., 2020; Asadieraghi and Daud, 2015). The FTIR peaks for all three catalysts-driven bio-oils demonstrate the existence of a bonded hydroxyl group, indicating an abundance of alcohol and phenols. Peaks at 1513.3, 1410–1310, 1267.3, and 1021 cm^{-1} bands suggest C–H bending vibration, phenol, or tertiary alcohol OH bend, aromatic ether, or aryl-O stretch for all bio-oils generated from catalytic pyrolysis.

The bio-oil derived from HTS pyrolysis using CIM as catalyst has peaks at 2109.7, 1595.3, 1699.7, 752.9, and 693.3 cm^{-1} bands, which correspond to C–H stretch, Methylene C–H asymmetric/symmetric stretch, primary amine, >N–H bend, C–H aldehyde and ketone, C=O stretch, 2-Disubstitution (ortho substitution), alcohol, and OH out-of-plane bend, respectively. The difference in bio-oil fingerprints might be due to secondary reactions aided by catalysts.

Chromatographic composition of bio-oils from *hyphaene thebaica* shell pyrolysis

GC/MS analysis revealed the compounds in bio-oil from the HTS thermal and catalytic pyrolysis. This analysis indicated complex mixture compounds in eight different functional groups, as shown in Fig. 13, encompassing approximately thirty-nine (39) types of compounds, as presented in supplementary, Table S1. The bio-oils of HTS samples consisted of unsaturated acids, with octadecenoic acids dominating at 45 %. Nevertheless, esters, phenols, aldehydes, ketones, ethers, aromatics, and hydrocarbons were also detected. These chemicals are well known to be the primary products of lignocellulosic biomass pyrolysis (Palamanit et al., 2019; Ahmad et al., 2014), which are formed by the cleavage of ether linkages between cellulose, hemicellulose, and lignin-building units (Den et al., 2018). Applying the catalysts CZ, CZ-F, CZ-M, and CZ-FM to the pyrolysis alters the composition of the bio-oils in comparison to thermal pyrolysis. For example, CZ changes the acid composition and enhances the ester yields from 5 to 31 %, with diethyl phthalate dominating at 6 %. The alcohol yield increases slightly from 10 to 12 %, whereas the benzene derivative compounds and the synthesis of aldehydes and ketones decrease. Other compounds, such as ether, furan, and furfural, have reduced concentration due to the catalyst facilitating the cracking and hydrodeoxygenation of pyrolysis vapour. The chemical composition of biomass, particularly the breakdown of cellulose and hemicellulose through pyrolysis, has a pronounced impact on the acid content (45 %) in bio-oil. The introduction of catalysts results in the presence of ester and alcohol in the resulting bio-oil from the condensing pyrolysis vapour, a phenomenon attributed to the catalysts' secondary activities on the chemical compounds ether, furan, and furfural associated with the decomposition of cellulose and hemicellulose in the resulting pyrolysis vapour.

The phenolic compounds are dominated by complex compounds such as 1H-Pyrrolo [3, 4-d]. Pyrimidine-2,5-dione, 4,6-bis(4-

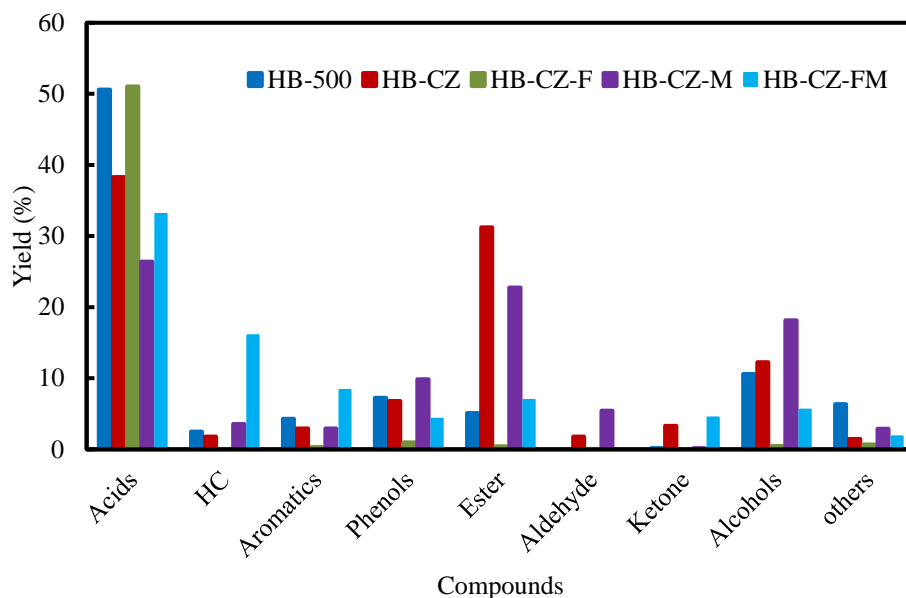


Fig. 13. Compounds of bio-oils from *hyphaene thebaica* shell pyrolysis. HB-500 is bio-oil derived from thermal pyrolysis without catalysts, while HB-CZ, HB-CZ-F, HB-CZ-M, and HB-CZ-FM are bio-oils from pyrolysis of *Hyphaene thebaica* shell using CZ, CI, CM, and CIM, as catalyst, respectively.

hydroxyphenyl)-1-methyl-3,4,6,7-tetrahydro- in thermal pyrolysis reduced to ethanamine, 2-phenoxy-, 5 % and 2,4-dimethoxyphenol, about 2 %. The cleavage of the macrostructure molecule is evidence of the catalytic cracking performance of CZ, which is characteristic of zeolite catalysts (Krisnandi et al., 2019; Liu et al., 2014).

The fact that bio-oil obtained using the CTD zeolite-Fe₂O₃-MgO (CZ-FM) composite as a catalyst contains the highest hydrocarbon (16 %) indicates the prospects of CZ-FM as a bioenergy catalyst. The CZ-FM displays activity towards deoxygenation; this might be due to the cracking nature of zeolite and iron, while magnesium aids in deal-koxylation and decarboxylation (Lazaridis et al., 2018). The bio-oil obtained using the CZ, CTD-derived zeolite and MgO (CZ-M) composite as catalyst comprises more esters, alcohols, aldehydes, and phenols. The primary characteristics of the nano-MgO-zeolite composite contribute to the esterification of the acids, which leads to a decrease in the percentage composition of acids and a significant appreciation of esters in the bio-oil.

The phenolic compounds in bio-oil catalysed by the CZ-F, CZ-M, and CZ-FM differ. The bio-oil produced by the catalytic pyrolysis of HTS with CZ-M as a catalyst has the most phenolic compounds, around 10 %, with over 80 % phenol. Because of the synergy between zeolite and nano-MgO, the pure phenol produced by the catalyst can facilitate secondary reactions such as cracking, demethylation, and demethoxylation reactions. These are the properties of alkaline earth metals with zeolite composites (Liu et al., 2017). The CZ-M can serve as a catalyst in chemical and bioenergy production from biomass pyrolysis.

Elemental composition of bio-oils from *hyphaene thebaica* shell pyrolysis

Table 6 presents the elemental composition of the bio-oil along with HHV and degree of deoxygenation (DOD). There was a drastic reduction in nitrogen from 1.14 to 0.39 % when CZ was used as the catalyst. The CZ facilitated the cracking of complex nitrogenous compounds that liberate molecular nitrogen, or ammonia, in the gaseous phase. It is worth noting that carbon and hydrogen slightly decrease. This might be due to the loss of hydrogen and carbon in cracking, hydro-deoxygenation, decarboxylation, and decarbonylation processes, which are characteristics of zeolite-based catalysts (Naqvi et al., 2015; Lazaridis et al., 2018).

It can be observed that there is an increase in nitrogen composition from 1.14 in the previous study to approximately 1.8 % due to reactions of the pyrolysis with nitrogen-producing nitrogenous compounds. It is worth noting that carbon and hydrogen slightly decrease. Furthermore, the composite catalysts extensively affected the pyrolysis reactions by increasing the DOD to higher than when CZ was the catalyst. The HHV of the respective bio-oils concurrently increased to values higher than that of the precursor biomass, HTS. The CZ-M demonstrates a better degree of deoxygenation, about 45.16 %, and the HHV is approximately 23 MJ/kg for the bio-oils. This is attributed to cracking, and deoxygenations reactions such as hydrodeoxygenation, decarboxylation, and decarbonylation reactions that are characteristics of zeolite-based catalysts in pyrolysis decomposition of biomass (Naqvi et al., 2015; Lazaridis et al., 2018).

Table 6
Elemental composition of *hyphaene thebaica* shell (HTS) bio-oils.

Component	C	H	N	S	O	DOD	HHV (MJ/kg °C)
	wt%						
HTS biomass	42.52	5.50	0.55	1.17	50.26	0	17.42.
HB-500	67.45	3.57	1.14		27.84	44.61	23.18
HB-CZ	66.9	3.32	0.39		29.39	41.52	22.88
HB-C-F	66.31	3.69	1.83		28.17	43.95	23.27
HB-CZ-M	66.5	4.11	1.83		27.56	45.16	23.07
HB-CZ-FM	66.14	4.01	1.75		28.1	44.09	23.08

HB-500 is bio-oil derived from HTS pyrolysis without catalysts, while HB-CZ, HB-CZ-F HB-CZ-M, and HB-CZ-FM are bio-oils from HTS pyrolysis using CZ, CZ-F, CZ-M, and CZ-FM, as catalyst, respectively.

Relative extent of coking on spent catalysts

Carbon is the primary source of zeolite-based catalyst deactivation in biomass pyrolysis valorisation for bio-oil production because it blocks the active sites. EDX is a semi-quantitative method that can reveal the presence of coke in the form of elemental carbon on various catalyst samples (Kholkina et al., 2019; Murkute et al., 2011). The analysis revealed the amount of carbon, as coke on the spent catalysts. Fig. 14 shows an EDX spectrum expressing the extent of coke on the catalysts used in this study. The EDX revealed no carbon as coke on the CZ and its metal-oxides composite catalysts before their use in the HTS pyrolysis.

The percentage composition of carbon on the spent CZ-F, CZ-M, and CZ-FM is 4.5, 7.5, and 3.1 %, respectively. The coke impaired the catalysts' active sites and clogged the catalysts' pores, limiting hydrogen transfer, condensation, aromatisation, decarboxylation, decarbonylation, dehydro-deoxygenation, and the cyclisation reaction of oxygenates. The coking often occurs on the active sites, where the reactions occur (Jia et al., 2017). CZ-M has the highest coked, with carbon of about 7.4 % relative composition. This indicates that CZ-M can deactivate faster than the other composite catalysts, CZ-F and CZ-FM. The CZ-FM has the lowest relative carbon content after usage, which signifies that the CZ-FM can have a longer life span during pyrolysis reactions than the CZ-F and CZ-FM catalysts.

Conclusion

The study volarised the use of CTD, IOD-derived Fe₂O₃, and MgO as precursors for the production of ZSM-5 and metal-oxides (MgO, Fe₂O₃, and Fe₂O₃/MgO) modified ZSM-5 for the HTS pyrolysis in a fixed-bed reactor. At 500 °C and 150 mL/min, the HTS thermal pyrolysis achieved a maximum yield of 32 % bio-oil. The bio-oils are laden with acids, with 45 % octadecenoic acids. In addition to esters, the bio-oil contained phenols, aldehydes, ketones, ethers, aromatics, and hydrocarbons. The CTD resulted in a mesoporous zeolite using carboxymethyl cellulose as a templating agent. The zeolite contains a prominent ZSM-5 crystal phase, with pore sizes ranging from 1.8–6 nm, 229 m²/g surface area, and 1145 μmol/g total acidity. Through pyrolysis, the CZ profoundly affected the composition of HTS bio-oil. Phenolics and acids are the compounds that saturate the various bio-oils. The acids were lowered under catalytic pyrolysis conditions, while ester yields increased from 5–31 %. Also, the nitrogen compounds in the bio-oil decreased from 1.14–0.34 %. The dispersion of the metal oxides positively altered the CZ catalytic activity and selectivity during the pyrolysis. The CZ, CZ-F, CZ-M, and CZ-FM have improved the quality of the bio-oils. Furthermore, CZ-F, CZ-M, and CZ-FM have coke contents of 4.5, 7.5, and 3.1 %, respectively. Because CZ-M has the most coke (7.4 %), is likely to deactivate faster than CZ-F and CZ-FM. The study demonstrated that using CTD, zeolite, ZSM-5, and metal-oxides modified ZSM-5 (CZ-M, CZ-F, and CZ-FM) as catalysts in the pyrolysis of HTS increased the quality of the resulting bio-oils. Further studies will focus on detailed characterisations of the synthesised catalysts to develop reaction mechanisms to understand the reactions leading to the bio-oil compounds.

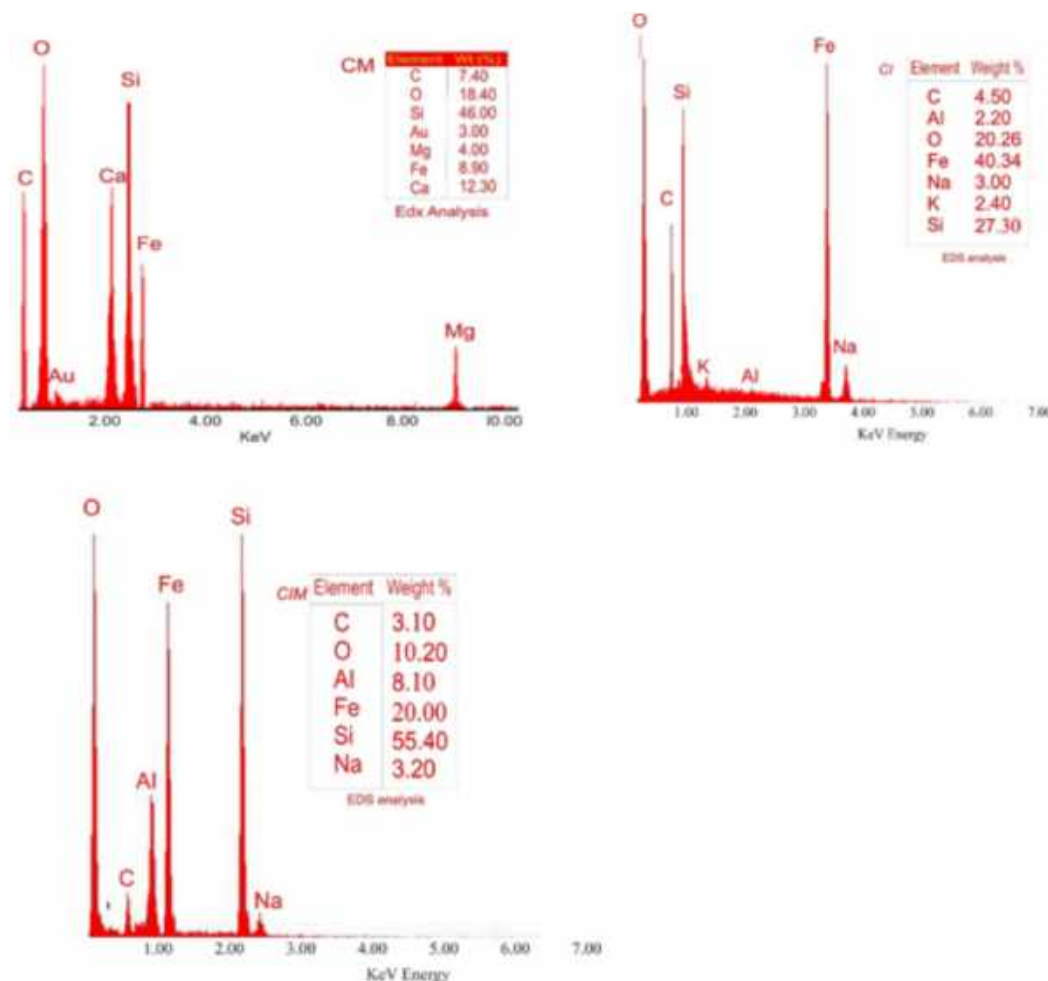


Fig. 14. EDX elemental composition of the spent catalysts.

CRedit authorship contribution statement

Habu Iyodo Mohammed: Writing – review & editing, Writing – original draft, Validation, Methodology, Investigation, Formal analysis, Data curation. **Kabir Garba:** Writing – review & editing, Supervision, Project administration, Methodology, Investigation, Funding acquisition, Formal analysis, Data curation, Conceptualization. **Saeed I. Ahmed:** Supervision. **Lawan G. Abubakar:** Writing – review & editing, Supervision, Project administration, Funding acquisition.

Declaration of competing interest

The authors declare that they have no known competing financial interests or personal relationships that could have appeared to influence the work reported in this paper.

Acknowledgement

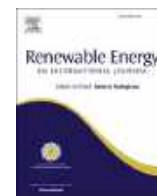
The authors gratefully acknowledged the support of the Tertiary Education Fund of Nigeria under the National Research Grant (Project No: TETFund/DR&D/CE/NRF/2019/STI/49).

References

Aguilar, G., Muley, P.D., Henkel, C., Boldor, D., 2015. Effects of biomass particle size on yield and composition of pyrolysis bio-oil derived from Chinese tallow tree (*Triadica sebifera* L.) and energy cane (*Saccharum complex*) in an inductively heated reactor. *AIMS Energy*. 3, 838–850. <https://doi.org/10.3934/energy.2015.4.838>.

- Aguilar-Mamani, W., García, G., Hedlund, J., Mouzon, J., 2014. Comparison between leached metakaolin and leached diatomaceous earth as raw materials for the synthesis of ZSM-5. *Springerplus*. 3, 1–10. <https://doi.org/10.1186/2193-1801-3-292>.
- Ahmad, R., Hamidin, N., Ali, U.F.M., Abidin, C.Z.A., 2014. Characterization of bio-oil from palm kernel shell pyrolysis. *J. Mech. Eng. Sci.* 7, 1134–1140. <https://doi.org/10.15282/jmes.7.2014.12.0110>.
- Asadieraghi, M., Daud, W.M.A.W., 2015. In-depth investigation on thermochemical characteristics of palm oil biomasses as potential biofuel sources. *J. Anal. Appl. Pyrolysis*. 115, 379–391. <https://doi.org/10.1016/j.jaap.2015.08.017>.
- Dawes, G.J.S., Scott, E.L., Le Nôtre, J., Sanders, J.P.M., Bitter, J.H., 2015. Decarboxylation and Decarbonylation – a review. *Green Chem.* 2015, 3231–3250. <https://doi.org/10.1039/c5gc00023h>.
- Den, W., Sharma, V.K., Lee, M., Nadadur, G., 2018. Lignocellulosic biomass transformations via greener oxidative pretreatment processes: access to energy and value-added chemicals. *Front. Chem.* 6, 1–23. <https://doi.org/10.3389/fchem.2018.00141>.
- Ding, K., Corma, A., Macia, J.A., Hu, J.G., Kra, S., Stair, P.C., Stucky, G.D., 2015. Constructing hierarchical porous zeolites via kinetic regulation. *Journal of the American Chemical Society*. <https://doi.org/10.1021/jacs.5b06791>.
- Dutta, A., Iisa, K., Mukarakate, C., Griffin, M., Tan, E.C.D., Schaidle, J., Humbird, D., Wang, H., Hartley, D., Thompson, D., Cai, H., Dutta, A., Iisa, K., Mukarakate, C., Griffin, M., Tan, E.C.D., Schaidle, J., Humbird, D., Wang, H., Hartley, D., Thompson, D., Cai, H., 2018. Ex situ catalytic fast pyrolysis of lignocellulosic biomass to hydrocarbon fuels: 2018 state of technology and future research. *Natl. Renew. Energy Lab.* 1–43.
- El-Sayed, S.A., Khairy, M., 2015. Effect of heating rate on the chemical kinetics of different biomass pyrolysis materials. *Biofuels*. 6, 157–170. <https://doi.org/10.1080/17597269.2015.1065590>.
- Fermanelli, C.S., Córdoba, A., Pierella, L.B., Saux, C., 2020. Pyrolysis and copyrolysis of three lignocellulosic biomass residues from the agro-food industry: a comparative study. *Waste Manag.* 102, 362–370. <https://doi.org/10.1016/j.wasman.2019.10.057>.
- Gao, Y., Yang, Y., Qin, Z., Sun, Y., 2016. Factors affecting the yield of bio-oil from the pyrolysis of coconut shell. *Springer plus*. 5, 1–8. <https://doi.org/10.1186/s40064-016-1974-2>.

- Garba, K., Yakub, I., Makarfi, Y., Garba, L., Abdalla, Y., Hameed, B.H., 2023. Pyrolysis of Canarium schweinfurthii hard-shell: thermochemical characterisation and pyrolytic kinetics studies. *Heliyon*. 9, e13234. <https://doi.org/10.1016/j.heliyon.2023.e13234>.
- Gibril, M.E., Zhang, N., Yi, Y., Liu, P., Wang, S., Tesfaye, T., Kong, F., 2020. Physicochemical characterization and future beneficiation routes of wild fruit waste (Hyphaene Thebaica seed) as a source to extract mannan. *J. Clean. Prod.* 267, 121949. <https://doi.org/10.1016/j.jclepro.2020.121949>.
- Hani, F.F.B., Hailat, M.M., 2016. Production of Bio-oil from pyrolysis of olive biomass with/without catalyst. *Adv. Chem. Eng. Sci.* 06, 488–499. <https://doi.org/10.4236/aces.2016.64043>.
- Jia, L.Y., Raad, M., Hamieh, S., Toufaily, J., Hamieh, T., Bettahar, M.M., Mauviel, G., Tarrighi, M., Pinard, L., Dufour, A., 2017. Catalytic fast pyrolysis of biomass: Superior selectivity of hierarchical zeolites to aromatics. *Green Chem.* 19, 5442–5459. <https://doi.org/10.1039/c7gc02309j>.
- Kabir, G., Mohd Din, A.T., Hameed, B.H., 2017. Pyrolysis of oil palm mesocarp fiber catalyzed with steel slag-derived zeolite for bio-oil production. *Bioresour. Technol.* 249, 42–48. <https://doi.org/10.1016/j.biortech.2017.09.190>.
- Kabir, G., Mohammed, I.Y., Abakr, Y.A., Hameed, B.H., 2022. Intermediate pyrolysis of desert date shell for conversion to high-quality biomaterial resources. *Chem. Eng. Technol.* 1–11. <https://doi.org/10.1002/ceat.202200095>.
- Karge, H.G., 2001. Characterization by IR spectroscopy, in Robson, H., Lillerud, K. P., (Eds.), *Verified Syntheses of Zeolitic Materials*. Elsevier Science B.V. pp.69–71. <https://doi.org/10.1016/B978-044450703-7/50113-7>.
- Kholkina, E., Kumar, N., Ohra-aho, T., Lehtonen, J., Lindfors, C., Perula, M., Peltonen, J., Salonen, J., Murzin, D.Y., 2019. Synthesis and characterization of novel catalytic materials using industrial slag: influence of alkaline pretreatment, synthesis time and temperature. *Top. Catal.* 62, 738–751. <https://doi.org/10.1007/s11244-019-01162-5>.
- Krisnandi, Y.K., Saragi, I.R., Sihombing, R., Ekananda, R., 2019. Synthesis and characterization of crystalline NaY-Zeolite from belitung kaolin as catalyst for n-hexadecane cracking. *Crystals*.
- Lazaridis, P.A., Fotopoulos, A.P., Karakoulia, S.A., 2018. Catalytic fast pyrolysis of kraft lignin with conventional, mesoporous and nanosized ZSM-5 zeolite for the production of alkyl-phenols and aromatics. *Front. Chem.* 6, 1–21. <https://doi.org/10.3389/fchem.2018.00295>.
- Lee, S.Y., Sankaran, R., Chew, K.W., Tan, C.H., Krishnamoorthy, R., Chu, D.-T., Show, P.-L., 2019. Waste to bioenergy: a review on the recent conversion technologies. *BMC Energy*. 1, 1–23. <https://doi.org/10.1186/s42500-019-0004-7>.
- Li, Y., Wang, X., Song, H., Shao, J., Ma, H., Chen, H., 2019. Phenols production from online catalytic conversion of corn stalk pyrolysis vapors using Char in-situ. *BioResources*. 13, 4884–4896. <https://doi.org/10.15376/biores.13.3.4884-4896>.
- Liu, Z., Jenkins, B.M., Li, Y., Yi, W., 2017. Influence of alkali and alkaline earth metallic species on the phenolic species of pyrolysis oil. *BioResources*. 12, 1611–1623.
- Liu, J., Jiang, G., Liu, Y., Di, J., Wang, Y., Zhao, Z., Sun, Q., Xu, C., Gao, J., Duan, A., Liu, J., Wei, Y., Zhao, Y., Jiang, L., 2014. Hierarchical macro-meso-microporous ZSM-5 zeolite hollow fibers with highly efficient catalytic cracking capability. *Scientific Reports* 1–6. <https://doi.org/10.1038/srep07276>.
- Liu, C., Wang, H., Northwest, P., Sun, J., Wang, Y., Liu, C., Wang, H., Northwest, P., Sun, J., 2014. Catalytic fast pyrolysis of lignocellulosic biomass. *R. Soc. Chem.* 43. <https://doi.org/10.1039/c3cs60414d>.
- Lugovoy, Y.V., Chalov, K.V., Kositsov, Y.Y., Sulman, E.M., Mikhail, G., 2019. Pyrolysis of agricultural waste in the presence of Fe-subgroup metal-containing. *Catalysts* 76, 1453–1458. <https://doi.org/10.3303/CET1976243>.
- Mohabeer, C., Reyes, L., Abdelouahed, L., Marcotte, S., Taouk, B., 2019. Pyrolysis Investigating catalytic de-oxygenation of cellulose, xylan and lignin bio-oils using HZSM-5 and Fe-HZSM-5. *J. Anal. Appl. Pyrolysis*. 137, 118–127. <https://doi.org/10.1016/j.jaap.2018.11.016>.
- Mohammed, H.I., Garba, K., Ahmed, S.I., Abubakar, L.G., 2022. Thermodynamics and kinetics of Doum (*Hyphaene thebaica*) shell using thermogravimetric analysis: a study on pyrolysis pathway to produce bioenergy. *Renew. Energy*. 200, 1275–1285. <https://doi.org/10.1016/j.renene.2022.10.042>.
- Mohiuddin, E., Isa, Y.M., Mdeleni, M.M., Sincadu, N., Key, D., Tshabalala, T., 2016. Synthesis of ZSM-5 from impure and beneficiated Grahamstown kaolin: effect of kaolinite content, crystallisation temperatures and time. *Appl. Clay Sci.* 119, 213–221. <https://doi.org/10.1016/j.clay.2015.10.008>.
- Mozgawa, W., Król, M., Barczyk, K.M., 2011. Science, FT-IR studies of zeolites from different structural groups. *CHEMIK*.
- Murkute, A.D., Jackson, J.E., Miller, D.J., 2011. Supported mesoporous solid base catalysts for condensation of carboxylic acids. *J. Catal.* 278, 189–199. <https://doi.org/10.1016/j.jcat.2010.12.001>.
- Na, C., De, D., Mohabeer, C., Chetna, D.D., Mohabeer, 2018. Bio-oil production by pyrolysis of biomass coupled with a catalytic de-oxygenation treatment. *Catal. Normandie Univ.* 1–207.
- Naqvi, S.R., Naqvi, M., 2017. Catalytic fast pyrolysis of rice husk: Influence of commercial and synthesized microporous zeolites on deoxygenation of biomass pyrolysis vapors. *Int. J. Energy Res.* 2017, 1–11. <https://doi.org/10.1002/er.3943>.
- Naqvi, S.R., Uemura, Y., Yusup, S., Sugiur, Y., Nishiyama, N., Naqvi, M., 2015. The role of zeolite structure and acidity in catalytic deoxygenation of biomass pyrolysis vapors. *Energy Procedia*. 75, 793–800. <https://doi.org/10.1016/j.egypro.2015.07.126>.
- Nasuha, N., Ismail, S., Hameed, B.H., 2017. Activated electric arc furnace slag as an effective and reusable Fenton-like catalyst for the photodegradation of methylene blue and acid blue 29. *J. Environ. Manage.* 196, 323–329. <https://doi.org/10.1016/j.jenvman.2017.02.070>.
- Özçakır, G., Karaduman, A., 2021. Effect of metal doped zsm-5 catalyst on aromatic yield and coke formation in microalgal bio-oil production. *Bartın Univ. Int. J. Nat. Appl. Sci.* 4, 20–32.
- Palamanit, A., Khongphakdi, P., Tirawanichakul, Y., Phusunti, N., 2019. Investigation of yields and qualities of pyrolysis products obtained from oil palm biomass using an agitated bed pyrolysis reactor. *Biofuel Res. J.* 6, 1065–1079. <https://doi.org/10.18331/BRJ2019.6.4.3>.
- Safdari, M.S., Amini, E., Weise, D.R., Fletcher, T.H., 2019. Heating rate and temperature effects on pyrolysis products from live wildland fuels. *Fuel*. 242, 295–304. <https://doi.org/10.1016/j.fuel.2019.01.040>.
- Saif, A.G.H., Wahid, S.S., Ali, M.R.O., 2020. Pyrolysis of sugarcane bagasse: the effects of process parameters on the product yields. *Mater. Sci. Forum*. 1008, 159–167. <https://doi.org/10.4028/www.scientific.net/MSF.1008.159>.
- Sanna, A., Andrésén, J., 2012. Bio-oil deoxygenation by catalytic pyrolysis: new catalysts for the bio-oil deoxygenation by catalytic pyrolysis: novel catalysts for the conversion of biomass into densified and deoxygenated bio-oil. *ChemSusChem*. <https://doi.org/10.1002/cssc.2001>.
- Šimáček, P., Biernacki, J.J., Northrup, S., Mohammad, A.S., 2017. Biomass pyrolysis kinetics: a review of a review of molecular-scale modeling contributions. *Brazilian J. Chem. Eng.* 34, 1–18.
- Smail, H.A., Rehan, M., Shareef, K.M., Ramli, Z., 2019. Synthesis of uniform mesoporous zeolite ZSM-5 catalyst for friedel-crafts acylation. *ChemEngineering*. 3, 1–11. <https://doi.org/10.3390/chemengineering3020035>.
- Soltanali, S., Darian, J.T., 2018. Synthesis and characterization of ZSM-5 zeolite from dealuminated and fragmented bayat- klaten natural zeolite synthe. *J. Phys. Conf. Ser.* 1–6.
- Stegen, S., Kaparaju, P., 2020. Effect of temperature on oil quality obtained through pyrolysis of sugarcane bagasse. *Fuel*. 276, 118112. <https://doi.org/10.1016/j.fuel.2020.118112>.
- Takahashi, M., Fuji, M., 2002. Synthesis and fabrication of inorganic porous materials: from nanometer to millimeter sizes. *KONA Powder Part. J.* 20, 84–97. <https://doi.org/10.14356/kona.2002011>.
- Uddin, M.N., Techato, K., Taweekun, J., Rahman, M.M., Rasul, M.G., Mahlia, T.M.I., Ashrafur, S.M., 2018. An overview of recent developments in biomass pyrolysis technologies. *Energies*. 11. <https://doi.org/10.3390/en11113115>.
- Waluyo, J., Makertihartha, I., Susanto, H., 2018. Pyrolysis with intermediate heating rate of palm kernel shells: effect temperature and catalyst on product distribution pyrolysis with intermediate heating rate of palm kernel shells: effect temperature and catalyst on product distribution. *AIP Conf. Proc.* 1977, 020026.
- Wibowo, W.A., Cahyono, R.B., Rochmadi, R., Budiman, A., 2023. Kinetics of in-situ catalytic pyrolysis of rice husk pellets using a multi-component kinetics model. *Bulletin of Chemical Reaction Engineering & Catalysis* 18, 85–102. <https://doi.org/10.9767/bcrec.17226>.
- Wu, F., Ben, H., Yang, Y., Jia, H., Wang, R., Han, G., 2020. Effects of different conditions on co-pyrolysis behavior of corn stover and polypropylene. *Polymers (Basel)*. 12. <https://doi.org/10.3390/POLYM12040973>.
- Yue, Y., Liu, H., Yuan, P., Yu, C., Bao, X., 2015. One-pot synthesis of hierarchical FeZSM-5 zeolites from natural aluminosilicates for selective catalytic reduction of NO by NH₃. *Sci. Rep.* 5, 1–10. <https://doi.org/10.1038/srep09270>.
- Yunusa, S., Ahmed, A.S., Yusuf, M., Abubakar, M., Bawa, S.G., 2020. Characterization of synthesized zeolite socony mobil 5 (ZSM-5) from bularafa diatomite. *Arid Zo. J. Eng. Technol. Environ.* 16, 717–724.
- Zaman, K.K., Balasundram, V., Ibrahim, N., Samsudin, M.D.M., Kasmani, R.M., Hamid, M.K.A., Hasbullah, H., 2018. Effect of particle size and temperature on pyrolysis of palm kernel shell. *Int. J. Eng. Technol.* 7, 118–124. <https://doi.org/10.14419/ijet.v7i4.35.22339>.
- Zheng, A., Jiang, L., Zhao, Z., Huang, Z., Zhao, K., Wei, G., 2017. Catalytic fast pyrolysis of lignocellulosic biomass for aromatic production: chemistry, catalyst and process. *WIREs Energy Environ.* 6, 1–18. <https://doi.org/10.1002/wene.234>.
- Zheng, Y., Wang, J., Liu, C., Lu, Y., Lin, X., Li, W., Zheng, Z., 2020. Catalytic copyrolysis of metal impregnated biomass and plastic with Ni-based HZSM-5 catalyst: synergistic effects, kinetics and product distribution. *Int. J. Energy Res.* 44, 5917–5935. <https://doi.org/10.1002/er.5370>.
- Zinchik, S., Klinger, J.L., Westover, T.L., Donepudi, Y., Hernandez, S., Naber, J.D., Bar-Ziv, E., 2018. Evaluation of fast pyrolysis feedstock conversion with a mixing paddle reactor. *Fuel Process. Technol.* 171, 124–132. <https://doi.org/10.1016/j.fuproc.2017.11.012>.



Thermodynamics and kinetics of Doum (*Hyphaene thebaica*) shell using thermogravimetric analysis: A study on pyrolysis pathway to produce bioenergy

Habu Iyodo Mohammed^{a,c}, Kabir Garba^{a,*}, Saeed I. Ahmed^a, Lawan G. Abubakar^b

^a Department of Chemical Engineering, Abubakar Tafawa Balewa University, P.M.B, 0248, Bauchi, Nigeria

^b Department of Agricultural and Bioresource Engineering, Abubakar Tafawa Balewa University, P.M.B 0248, Bauchi, Nigeria

^c Department of Chemical Engineering, University of Maiduguri, P.M.B, 1068, Maiduguri, Nigeria

ARTICLE INFO

Keywords:

Doum (*Hyphaene thebaica*) shell

Kinetics

Pyrolysis

Thermodynamics

Thermogravimetric analysis

ABSTRACT

Doum (*Hyphaene thebaica*) palm pulp used to produce local beverages left behind enormous, difficult to manage *Hyphaene thebaica* Shell (HTS) wastes. To pioneer the determination of HTS bioenergy potential, compositional and thermogravimetric analyses to determine the kinetic and thermodynamic characteristics were employed. The HTS had 5.50 wt% hydrogen, 42.50 wt% carbon, and 74.31 wt% volatile matter. The FTIR functional groups matched those found in other recognised biomass sources. Thermogravimetry revealed that HTS pyrolysis occurred in three stages. In total, nearly 70% of the biomass was lost between 32 and 900 °C, with 50% of the loss in the active pyrolysis zone. The average activation energies for the Iso-conversional methods' Kissinger-Akahira-Sunose, Flynn-Wall-Ozawa, and Starink models respectively, were 118.15, 142.81 and 139.56 kJ/mol. The Flynn-Wall-Ozawa technique best fit the pyrolysis data according to the Akaike information criterion (AIC). The multi-step pyrolysis reactions were controlled by the diffusion and contraction mechanisms of Coats-Redfern method, with activation energies of 38.83 and 16.62 kJ/mol, respectively. According to the AIC, the pyrolysis can be accurately predicted by the Gistling-Brounshtein kinetic model. The pyrolysis reactions have a high-degree of disorder, are endothermic, irreversible, and non-spontaneous. The outcome of the study ascertained the HTS viability for bioenergy production.

1. Introduction

Due to the finite nature of fossil fuels and the related environmental damage, there has been a need for alternative fuels, which resulted in the development of renewable fuels from biomass. This sparked greater investigation into sustainable and workable feedstock as well as technology for renewable energy sources. Food products are used as feedstock for first-generation biofuels [1]. Food insecurity is threatened by biofuel made from food sources, which is why non-food sources are being sought after as bioenergy feedstock [2]. The main sources of lignocellulosic biomass used to produce second-generation biofuels are forest and agricultural wastes [3,4]. Typically, countries in the European Union recommend that biofuels make up 25% of transportation fuel in order to reduce their reliance on fossil fuels by 30% by 2030 [5], and other emerging nations are following suit. The viability of biomass as a source of energy must be examined in order to assess their performance.

Recently, attention has been shifted to identifying suitable biomass sources and conversion routes that can provide high energy outputs and bio-based materials to complement conventional fossil fuels. Lignocellulosic biomass residues are widely favoured as potential feedstocks for bio-based materials that are least competitive [6]. The biomass residues are often sourced from agro-waste, forest by-products, industrial bio-wastes, and so on. Nigeria is a country with a wide variation in vegetation distribution, ranging from semi-arid to rain-forest belts. Most available lignocellulosic biomass residues are mostly of agricultural origin like rice straw, sugar cane bagasse, rice husk, corn stover, corn-stalk, and oil palm residues, among others [7]. The bioenergy potentials of the biomass residues are comprehensively studied through thermochemical conversion processes such as pyrolysis, gasification, and hydrothermal processes, which are widely used to convert biomass to quality bioenergy precursors. The conversion processes curtailed the environmental nuisance and pollution associated with the poor handling

* Corresponding author.

E-mail addresses: kgabir@atbu.edu.ng, kbgarba.1214@gmail.com (K. Garba).

<https://doi.org/10.1016/j.renene.2022.10.042>

Received 13 June 2022; Received in revised form 28 September 2022; Accepted 10 October 2022

Available online 15 October 2022

0960-1481/© 2022 Elsevier Ltd. All rights reserved.

of the biomass residues [8].

Biochemical and thermochemical processes are the most common methods for converting biomass into bioenergy. Producing value-added products from lignin-free biomass has been greatly aided by biochemical processing [9]. The lignin included in lignocellulosic biomass resists microbial conversion to its monomeric unit. The present method for converting lignocellulosic biomass into bioethanol uses wet chemical hydrolysis, which is harmful to the environment [10]. This renders the lignocellulosic biomass transformation by biochemical process unsuitable. On the other hand, lignocellulosic biomass can be converted to energy, biofuels, and chemicals by a thermochemical process that includes combustion, hydrothermal liquefaction, gasification, and pyrolysis.

Biomass is burned directly to produce energy in a thermochemical process known as direct combustion. In some situations, such as home applications and biomass-based steam power plants, raw biomass is used as fuel [11]. In terms of energy savings and environmental protection, gasification is thought to use syngas far more effectively than combustion [12]. Through a series of thermochemical reactions, biomass is partially oxidised into a combustible gas mixture during the process of “gasification” (800–1000 °C) [13]. Syngas, a blend of CO, H₂, CO₂, N₂, and CH₄, is produced by the gasification of biomass in the presence of oxygen and steam [13]. Syngas can be burned directly or utilized as a fuel for gas engines or gas turbines because it has a high heating value (HHV) of 4–6 MJ/m³. Tar is produced throughout the process, but it cannot be applied directly or utilized as fuel. It necessitates additional treatments, which raises the overall cost of the procedure. Wet biomass material can be transformed into liquid fuel by a process called hydrothermal liquefaction [14]. Thermochemical liquefaction, which produces bio-oil, is a high pressure (5–20 MPa) and low temperature (300–350 °C) process helped by a catalyst when hydrogen is present [15]. The system is excessively expensive due to the high pressure and hydrogen atmosphere. Although hydrothermal liquefaction offers the advantage of being able to turn wet biomass into energy [14], it also has the drawback of requiring complicated and expensive equipment [16]. Pyrolysis is the conversion of biomass to biochar, bio-oil, and gas at temperatures from 350 to 700 °C in the absence of oxygen [17]. Pyrolysis has the advantage of ability to control products distribution. The conversion of biomass by pyrolysis invariably results in the generation of volatile matter, biochar, and gas, similar to products obtained in a conventional refinery. The volatile matter condensed into bio-oil that could serve as a viable feedstock for fuels and chemicals [18,19].

The use of a thermogravimetric approach to evaluate the bioenergy potential of biomass via pyrolysis is well established [20]. The procedures for characterising the biomass as an energy resource via pyrolysis were previously reported; this includes thermogravimetric analysis, chemical composition analysis, and proximate and ultimate analysis [21,22]. Further understanding of the decomposition behaviour and detailed energy analysis are critical in assessing the bioenergy viability of the biomass. This includes a detailed kinetic study and reaction pathways, which are significant during the scale-up of pyrolysis reactors and the development of mathematical models [23]. Thermogravimetric analysis (TGA) is extensively used and reported in the literature [24,25]. The kinetics and thermodynamic data obtained from the devolatilisation of lignocellulosic biomass are important because the data can be used for the design and operation purposes of the pyrolysis reactors. Kinetic parameters are obtained by model-free methods and model-fitting approaches [26,27]. Iso-conversional methods are the widely reported model-free methods used in estimating the kinetic parameters and the extent of conversion [28]. White [29], recommends the use of various Iso-conversional methods for evaluating kinetic parameters, including Flynn-Wall-Ozawa (FWO), Kissinger-Akahira-Sunose (KAS), and Starink [30,31]. Wang et al. [32], have used model-fitting methods to describe the kinetic behaviour of cotton stalk and seaweed. The Coats-Redfern Method is a model-fitting approach that is frequently used because of its robustness [33]. The technique involves predicting reaction order

from a single weight loss curve. To fit experimental T profiles, the method employs well-established theoretical reaction models such as power laws and shrinking core models [29]. Thus, the models yield a set of activation energy and pre-exponential factors. Furthermore, the methods for evaluation of thermodynamics parameters for thermal decomposition of biomass was previously reported in the literature [34, 35], the thermodynamics variables include changes in enthalpy, entropy and Gibb's free energy.

In a world that is in constant need of resources for renewable energy and materials, the ongoing search and analysis of emerging biomass to determine their potential for bioenergy is required. Different lignocellulosic biomass, such as oil palm remnants [36] and forest residues [24], are being researched for the pyrolysis-based production of biofuel precursors. Oil palm frond (OPF), oil palm trunk (OPT), empty fruit bunches (EFB), palm kernel shell (PKS), rice husk (RH), rice straw (RS), and kenaf biomass (K) were all investigated using thermogravimetry by Sohni et al. [37]. The amount of volatile matter was in the order of EFB (83.42%) > K (82.70%) > OPT (81.46%) > OPF (76.98%) > RS (76.42%) > PKS (69.66%) > RH (66.65%). RH has the highest ash content (18.82%), however, PKS has the highest heating value. The biomass collection has a high potential for bio-based material synthesis. Thermogravimetric analysis of wheat straw, wheat dust, and corn cobs reveals that weight loss occurs between 250 and 400 °C, with about 75% loss of the initial mass and the activation energy of decomposition of 113–131 kJ/mol [38]. Thermal decomposition analysis of sugar cane bagasse shows that activation energy varies between 91.64 kJ/mol and 104.43 kJ/mol, the maximum weight loss of about 77% occurs between 300 and 400 °C [39]. Analysis of the thermal decomposition of poplar wood reveals that activation energy varies, with activation energy between 107.86 and 209.49 kJ/mol and maximum weight loss occurring between 500 and 800 K [40].

However, the results on the energy potential of many available biomass sources are still lacking, such as the shells of Doum (*Hyphaene thebaica*) fruit. The fruit has high nutraceutical (food and medicinal) values [41,42]. The usage of the pulp for beverages and the nut as vegetable ivory [43] generates a large quantity of the *Hyphaene thebaica* shell (HTS) as solid waste. The growing concern about waste management and the use of shell residue has inspired research in a variety of engineering fields. Seth et al. [44], and Alabi et al. [45], studied the potential of the shell powder as a filler for polymer composite material. The potential of activated shell used directly for heavy metals adsorption was also studied by Samaila, [46]. Activated carbon suitable for heavy metals adsorption was developed from the shell [47]. Moreover, the energy potential of the HTS as fuel for direct combustion was evaluated by Mani Kongnine et al. [48]. When biomass is burned directly for residential and industrial energy use, harmful greenhouse gases are typically released into the atmosphere. This necessitates evaluating the biomass for other thermochemical processes, like pyrolysis. It is important to highlight that, according to our review of the literature, there is little information available on the composition, decomposition behaviour, kinetics, thermodynamics, and potential bioenergy of HTS.

This paper reports for the first time the physico-chemical characteristics, investigates the thermogravimetric pyrolysis of the HTS, and calculates the kinetic and thermodynamic parameters using Coats Redfern and Iso-conversional techniques. The parameters would make it easier to scale up the woody shell pyrolyser system to produce biochar and bio-oils as high-value bioenergy precursors.

2. Materials and methods

2.1. Acquisition and preparation of *Hyphaene thebaica* shell

The fruit known as the Doum (*Hyphaene thebaica*) was supplied by a local vendor in Maiduguri, Borno State, Nigeria. The fruit's endocarp (woody shell) and endosperm (seed), which together make up 80% of the fruit's weight, are inedible and discarded as waste after the

mesocarp has been removed [49]. After the seed was removed, a locally built attrition grinding machine was used to crush and pulverise the woody shell named the Doum (*Hyphaene thebaica*) shell (HTS). As a result, a drying oven at 105 °C was used to dry the HTS powder with 75 m mesh particles for 24 h. The oven-dried powder was kept for future use in an airtight plastic bag.

2.2. Proximate and ultimate analyses of *Hyphaene thebaica* shell

PerkinElmer's 2400 Series II CHNO/S analyser was used for ultimate analysis to determine the compositions of carbon, hydrogen, nitrogen, and sulphur. The oxygen content was calculated by difference. The proximate analysis was carried out on a STA-8000, a PerkinElmer thermogravimetric analyser to examine the ash, fixed carbon, moisture and volatile matter on the HTS. The analyser had a precision temperature measurement of ± 5 °C and microbalance sensitivity of less than 1.0 μ g. A weighed sample in an aluminium crucible was placed on a microbalance in the analyser furnace. The analyser was calibrated for the analysis, performed based on the set heating profiles specified by the manufacturer. Under a dynamic temperature program with a heating rate of 10 °C/min, the thermogravimetric analyses were carried out in inert conditions using nitrogen (99% pure) as the carrier gas. The analysis's temperature programme was ramped up from 30 to 800 °C. The carrier gas was changed from nitrogen gas to oxygen gas (99% pure) at the end of the analysis in order to burn the residual biochar to ash. The American Society for Testing and Materials procedures recommended by the equipment manufacturer were performed for both the proximate and ultimate analyses. The high heating value (HHV), which was previously presented in the literature [50], was finally determined using Eq. (1).

$$\text{HHV (kcal/kg)} = 81(\text{C}) + 342.5(\text{H}-\text{O}/8) + 22.5(\text{S}) - 6(9\text{H}-\text{W}) \quad \text{Eq.1}$$

2.3. Inorganic elemental composition of *Hyphaene thebaica* shell

Energy dispersive X-ray (EDX) spectroscopy in a field-emission SEM (LEO SUPRA 35VPFESEM) SEM-EDAX equipment was used to examine the percentage elemental composition of the HTS.

2.4. Fourier transform infra-red (FTIR) analysis of *Hyphaene thebaica* shell

A PerkinElmer infrared spectrometer was used to conduct FTIR spectroscopy studies on the HTS functional groups and bond structure. An adequate 1:100 mixture of KBr powder and a small amount of oven-dried material was uniformly mixed before being compacted into a transparent pellet to produce a spectrum with distinct peaks. With a step size of 4 cm^{-1} and a scanning rate of 40, scanning was performed in a band between 4000 and 400 cm^{-1} . The spectrometer displayed an absorption spectrum with peaks corresponding to particular kinds of functional groups and bonds because the HTS absorbed infrared radiation from various bands. The absorption bands of the functional groups were matched with the catalogued spectra of known materials using an inbuilt reference library program installed in a computer database system. Then, the functional groups were identified in terms of spectrum peaks.

2.5. Thermogravimetric analysis *Hyphaene thebaica* shell

In this study, a thermogravimetric analyser TGA 50 (Shimadzu) was used for the analysis. Inside the analyser furnace, a microbalance was set up with an HTS weighted sample (approximately 10 mg) inside an aluminium crucible. A thermocouple that was directly attached to the crucible and placed close to the sample allowed for temperature measurement. The furnace was heated under an inert atmosphere created by

N₂ supplied at a flow rate of 50 mL/min and a temperature ramping from 30 to 900 °C at 10 °C/min. Pyris Software, a proprietary thermal software developed by PerkinElmer, controlled the thermogravimetric analyser's operations. The data acquired by the software was shown as weight loss profiles and derivative weight loss in terms of time and temperature. The experiments were repeated with heating rates of 15 and 20 °C/min. The HTS decomposition kinetics and thermodynamics parameters were calculated using the profiles.

2.6. Decomposition kinetic models of biomass

The stoichiometry and kinetics model for isothermal devolatilisation of biomass presented as Eqs. (2) and (3) respectively, was previously reported in the literature [33,51].

$$\text{B}_{(\text{s})} \rightarrow \text{V}_{(\text{g})} + \text{C}_{(\text{s})} \quad \text{Eq.2}$$

$$\frac{d\alpha}{dt} = k(T)f(\alpha) \quad \text{Eq.3}$$

The conversion (α) of biomass is expressed as Eq. (4).

$$\alpha = \frac{m_0 - m_t}{m_0 - m_f} \quad \text{Eq.4}$$

The unconverted biomass is calculated from $(1 - \alpha)$. The rate equation, Eq. (3) is expressed in the inform of reaction order model, previously presented by Ref. [33].

$$\frac{d\alpha}{dt} = (1 - \alpha)^n k(T) \quad \text{Eq.5}$$

Where $k(T)$ is defined using Arrhenius equation as follows:

$$k(T) = A \exp\left(-\frac{E_a}{RT}\right) \quad \text{Eq.6}$$

Combining Eqs. (5) and (6), yields Eq. (7).

$$\frac{d\alpha}{dt} = A \exp\left(-\frac{E_a}{RT}\right) f(\alpha) \quad \text{Eq.7}$$

Where: t is the time (s), T is the temperature (°C), α is the extent of reaction and $f(\alpha)$ is reaction model. The various integral and differential reaction model for solid reaction processes is previously reported by Ref. [29].

$$g(\alpha) = A \exp\left(-\frac{E_a}{RT}\right) f(\alpha) t \quad \text{Eq.8}$$

Where A is the pre-exponential factor and E_a is the activation energy are the Arrhenius parameters, whereas R is the gas constant.

Under non-isothermal condition, where pyrolysis is conducted at a constant heating rate (β).

$$\beta = \frac{dT}{dt} = \text{constant} \quad \text{Eq.9}$$

The rate equation, Eq. (7) is transformed to Eqs. (10) and (11):

$$\frac{d\alpha}{dT} = \frac{A}{\beta} \exp\left(-\frac{E_a}{RT}\right) f(\alpha) \quad \text{Eq.10}$$

$$g(\alpha) = \frac{d\alpha}{f(\alpha)} = A \exp\left(-\frac{E_a}{RT}\right) dT \quad \text{Eq.11}$$

Eq. (11) is solved based on two assumptions: (i) Regarding Coats-Redfern method, where activation energy is constant throughout the biomass conversion process, and (ii) Iso-conversional methods, where the activation energy varies with the degree of the conversion, each conversion has individual activation energy, respectively.

The solution of Eq. (11) for Coats-Redfern method was reported in Eq. (12) [52].

$$\ln \frac{g(\alpha)}{T^2} = \ln \left(\frac{AR}{\beta E} \right) - \frac{E_a}{RT} \quad \text{Eq.12}$$

Where, T is the temperature (°C), α is the extent of reaction, β is the heating rate (°C/min) and $g(\alpha)$ is reaction model in integral form. The various integral and differential reaction models for solid reaction processes were previously presented by Ref. [29].

2.6.1. Coats-Redfern method and iso-conversional methods of kinetics parameters

The Coats-Redfern method requires the plot of $\ln[g(\alpha)/T^2]$ against $1/T$ to determine the activation energy, reaction order and pre-exponential factor. The model that best fits the observed data is considered the reaction model. It is known that biomass devolatilisation occurs in a pyrolysis atmosphere through intricate reactions that involve several simultaneous reactions. The pyrolysis kinetics cannot be adequately described by a single kinetic model, such as the Coats-Redfern method. Determining the kinetics based on the change in activation energy with conversion during the pyrolysis process can therefore be done using model-free methods as trustworthy alternatives. Iso-conversional techniques like the Flynn-Wall-Ozawa (FWO), Kissinger-Akahira-Sunose (KAS), and Starink are chosen for investigating the kinetics of biomass pyrolysis. Each conversion from 0.1 to 0.8 results in the determination of the activation energy.

Eq. (13) is produced when Eq. (10) is solved.

$$g(\alpha) = \frac{A}{\beta} \cdot \frac{RT_m^2}{E_a} \exp(-E_a/RT) \quad \text{Eq.13}$$

The KAS model is presented as Eq. (14) [53] obtained from rearranging and taking natural logarithm of Eq. (13).

$$\ln \left(\frac{\beta}{T^2} \right) = \ln \left(\frac{AE_a}{Rg(\alpha)} \right) - \frac{E}{RT} \quad \text{Eq.14}$$

From the plot of $\ln \left(\frac{\beta}{T^2} \right)$ against $1/T$, the activation energy (E_a) is obtained from the slope $\left(-\frac{E_a}{R} \right)$.

Furthermore, the FWO method is based on Doyle's approximation for temperature integration, expressed as shown below:

$$g(\alpha) = \frac{A}{\beta} 0.00484 \exp \left(-1.052 \frac{E_a}{RT} \right) \quad \text{Eq.15}$$

Subsequently, taking natural log of both sides resulted in Eq. (16):

$$\ln(\beta) = \ln \frac{AE_a}{Rg(\alpha)} - 5.331 - 1.052 \frac{E_a}{RT} \quad \text{Eq.16}$$

Starink method is yet another approximation method using integral rate equation for biomass decomposition, which is expected to be more precise than KAS and FWO methods. The Starink model is expressed in the form of Eq. (17) [31].

$$\ln \left(\frac{\beta}{T^{1.92}} \right) = C_s - 1.0033 \frac{E_a}{RT} \quad \text{Eq.17}$$

The activation energy of the biomass decomposition was obtained from the slope of lines of $\ln \left(\frac{\beta}{T^2} \right)$ versus $1/T$ for KAS method, $\ln(\beta)$ versus $1/T$ for FWO method, and $\ln \left(\frac{\beta}{T^{1.92}} \right)$ against $1/T$ for Starink model.

Identification of Iso-conversional method that best fit the observed data for evaluating kinetics parameters for pyrolysis of *Hyphaene thebaica* shell was carried out using Akaike Information Criterion (AIC). The AIC indicate the model that fits better to the available data or observations than the other ones. The model with minimum AIC and likelihood of 1 is best fitted model [54]. The AIC equations reported in the literature [55] is presented in Eq. (18):

$$AIC = \frac{2k}{n} - \frac{2l}{n} \quad \text{Eq.18}$$

Where:

n number of data,

k number of estimated parameters,

l the log of likelihood function (assuming normally distributed errors), and is computed using Eq. (19):

$$l = -\frac{n}{2} \left(1 + \ln(2\pi) + \ln \left(\left(\frac{1}{n} \right) \cdot \sum_{i=1}^n (y_i - \hat{y}_i)^2 \right) \right) \quad \text{Eq.19}$$

The relative likelihood of the tested models was computed using Eq. (20):

$$\text{Relative Likelihood} = \exp(AIC_{\min} - AIC_i) \quad \text{Eq.20}$$

Where:

AIC_{\min} is the AIC of a model with minimum value

AIC_i AIC of model i

2.7. Evaluation of thermodynamics parameters for pyrolysis of *Hyphaene thebaica* shell

The thermodynamic parameters such as changes in enthalpy, Gibb's free energy, and entropy of devolatilisation reaction of HTS was evaluated using relationships from Eqs. (21)–(24) [56].

$$A = \frac{[\beta E \exp(E_a/RT_m)]}{RT_m^2} \quad \text{Eq.21}$$

$$\nabla H = E_a - RT_m \quad \text{Eq.22}$$

Where ∇H is change in enthalpy, E , activation energy, R , gas constant, and T_m is peak temperature of the DTG curve for the decomposition of HTS by pyrolysis.

$$\nabla G = E_a + RT_m \ln \left(\frac{K_B T_m}{hA} \right) \quad \text{Eq.23}$$

$$\nabla S = \frac{\nabla H - \nabla G}{T_m} \quad \text{Eq.24}$$

Where ∇G is the change in Gibb's free energy for thermal decomposition of HTS, K_B , Boltzman constant = $1.381 \times 10^{-23} \text{ J/K}$, h , Planck's constant = $6.626 \times 10^{-34} \text{ Js}$

3. Results and discussion

3.1. Physicochemical characteristics of *Hyphaene thebaica* shell

Table 1 presents the physicochemical characteristics for HTS and the other biomass sources that were revealed by proximate, ultimate, and calorific value investigations. According to the results of the proximate analysis, the HTS has a low ash content (8.753%) and a high reactivity ratio (VM/FC) of 6.12. Therefore, it follows that a lot more volatiles can be produced during pyrolysis, resulting in higher yields of bio-oil and gas and less residual biochar. A moisture content of 4.97% is acceptable and would result in little energy loss during the pyrolysis process due to vaporisation. The ultimate analysis revealed a high carbon content of 47.61% and 5.50% hydrogen to establish the HTS as an energy-generating precursor. Moreover, the HHV of 21.07 MJ/kg and the 1.55 H/C and 0.89 O/C ratios are attributes of HTS's good fuel characteristics that are comparable to other biomass sources. The ultimate analysis outcomes indicate a low amount of S (1.17%) and N (0.55%), desirable in eco-friendly bio-fuels, which gives the additional advantage

Table 1Physicochemical properties of *Hyphaene thebaica* shell and some typical biomass sources.

Biomass type	C (wt%)	H (wt%)	N (wt%)	S (wt%)	O (wt%)	H/C	O/C	HHV MJ/kg	^a V _m (wt%)	^b FC (wt%)	V _m /FC	^c MC (wt%)	Ash (wt%)	References
HTS	42.50	5.50	0.55	1.17	50.30	1.55	0.89	21.07	74.31	11.96	6.21	4.97	8.75	This study
Palm kernel shell	44.6	6.50	2.92	–	–	–	–	18.51	71.31	17.81	–	5.92	4.99	[2]
Wheat straw	38.34	5.47	0.60	0.37	–	–	–	14.68	83.08	10.29	–	12.81	6.63	[58]
Oil palm fond	41.00	6.74	0.67	0.35	51.24	0.16	1.25	18.97	70.33	–	–	4.83	5.87	[36]
Rapeseed straw	44.39	6.47	0.54	0.36	48.24	1.75	0.82	18.05	76.38	18.20	–	–	5.42	[22]
Kenaf stem	47.32	5.20	0.38	<0.02	47.1	–	–	18.54	83.05	15.80	–	4.4	1.15	[59]
Corn stover	41.92	6.34	1.85	0.47	–	1.78	0.87	15.60	73.41	11.44	–	12.77	6.43	[58]

^a V_m = Volatile matters.^b FC = Fixed carbon.^c MC = Moisture.

of less emission of poisonous NO_x and SO_x gases from the thermal decomposition of HTS. There is a high oxygen content in the HTS, which can result in a high composition of oxygenates in the resultant liquid from pyrolysis. Eventually, the heating value of the bio-oil produced from the HTS would be lower than the 23–47 MJ/kg of fossil fuels [57]. Overall, the investigations showed that HTS possesses the necessary qualities, allowing it to be pyrolysed into high-grade biofuel precursors rather than being burned directly for energy. The overall characteristics shown in Table 1 compared favourably with those of the other biomass sources and showed that HTS conversion by pyrolysis would produce high-quality bio-oils as precursors to liquid fuels.

Fig. S1 (Supplementary Figure) presents the energy dispersive X-ray spectrum, which highlighted the metal elements on the HTS and their associated compositions are shown in Table 2. The metal elements are stored as nutrients in the form of inorganic minerals within the biomass structures [11].

The content of the resulting bio-oil from the pyrolysis of the HTS would be altered by the metal elements, which are capable of catalysing the thermochemical conversion of biomass through pyrolysis. By catalysing the thermal degradation of biomass through pyrolysis, the alkali metals (Na and Mg) and Fe have an effect on the chemical contents of the bio-oils produced [60,61]. The biomass sources may host the same types of metal elements, but mostly different ones. The metal elements on HTS are comparable to those hosted on Kenaf stems [59], oil palm mesocarp fibre, and palm fronds [36], but their compositions are different.

3.2. Fourier transform infra-red (FTIR) analysis of *Hyphaene thebaica* shell

Fig. S2 (Supplementary Figure) displays the FTIR spectroscopy spectrum for the HTS sample. The intensity of the absorption band can be used to determine the functional groups and distinctive bonds of the various chemical groups contained in the cellulose, hemicellulose, and lignin components. The specific bands from FTIR spectroscopy related with the functional groups and fingerprint structure are also shown in Table 3; these bands primarily contain functional groups for alcohol,

Table 3FTIR spectrum peaks bands related to *Hyphaene thebaica* shell [62,63].

Wave number (cm ⁻¹)	Vibration	Functional group	Biomass component
3700–3600	NH ₂ (stretch)	Amine, amide	
3600–3000	OH (stretch)	Phenolic, alcoholic and carboxylic	
3000–2800	C–H (stretch)	CH ₂ , CH ₃	Hemicellulose
1730	C=O (stretch)	Carbonyl	Cellulose, lignin
1650–1510	C=C (stretch)	Aromatic ring	Hemicellulose, cellulose
1440–1400	O–H (bend)	Alcoholic, carboxylic	Hemicellulose, cellulose
1235	COOH (stretch)	Carboxylic acid, ester	Hemicellulose
1246–950	C–O–O, C–O, C–OH (stretch)	Lignin, polysaccharides	Cellulose, lignin, hemicellulose
850–750	C–H (bend)	Aromatic compounds	Lignin

esters, aromatics, ketone, alkane, and alkene [49,62]. The asymmetric C–H stretching caused by the aromatic bonds in lignin and alkyl groups is what causes the peak between the 2944 cm⁻¹ and 2843 cm⁻¹ bands, according to the FTIR spectroscopy theory. The bands around 1739 cm⁻¹ and 1627 cm⁻¹ are linked to C=O stretching associated with lignin and hemicellulose.

The peaks near to the 1233 cm⁻¹ band are caused by the lignin syringyl ring's C–O stretching. The bonds linked to the cellulose, hemicellulose, and lignin structures are observed to be responsible for the C–O, C=C, and C–O–C stretching around 1036 cm⁻¹. According to the spectrum, esters, ketones, alkanes and alkyl, ethers, and aromatic groups make up the macro-structural components of the HTS. The C–O stretching in the cellulose and hemicellulose structure is responsible for the noticeable peak near 1032 cm⁻¹. Consequently, the absorption peaks of the spectrum affirmed that HTS is a rich source of cellulose, hemicellulose, and lignin. The HTS can be a promising feedstock for thermochemical processes for bioresources materials such as bio-oil and biochar as fuel and chemicals products.

3.3. Thermogravimetric decomposition behaviour of *Hyphaene thebaica* shell

The results of thermogravimetry with temperature ramping suggested that biomass degrade in stages, as reported by the previous studies [35,64]. The chosen biomass source's various structural components degraded in three stages when heated externally during thermogravimetry studies. Thermogravimetry was used to examine the degradation of HTS at three different heating rates (10, 15, and 20 °C/min) in an inert atmosphere. Using thermogravimetric (TG) and derivative thermogravimetric (DTG) curves derived from thermogravimetric data, Fig. 1 (a) and (b) show the decomposition profile.

The thermogravimetric analysis technique, which provides the biomass thermal decomposition profile in an inert atmosphere, was used to examine the weight loss characteristics of the HTS. Three steps

Table 2Composition of in-organic elements of *Hyphaene thebaica* shell from EDX spectroscopy.

Element	wt%
O	43.927
Na	2.117
Mg	3.790
Al	9.237
Si	24.200
Cl	1.825
K	9.950
Ti	2.140
Fe	7.827

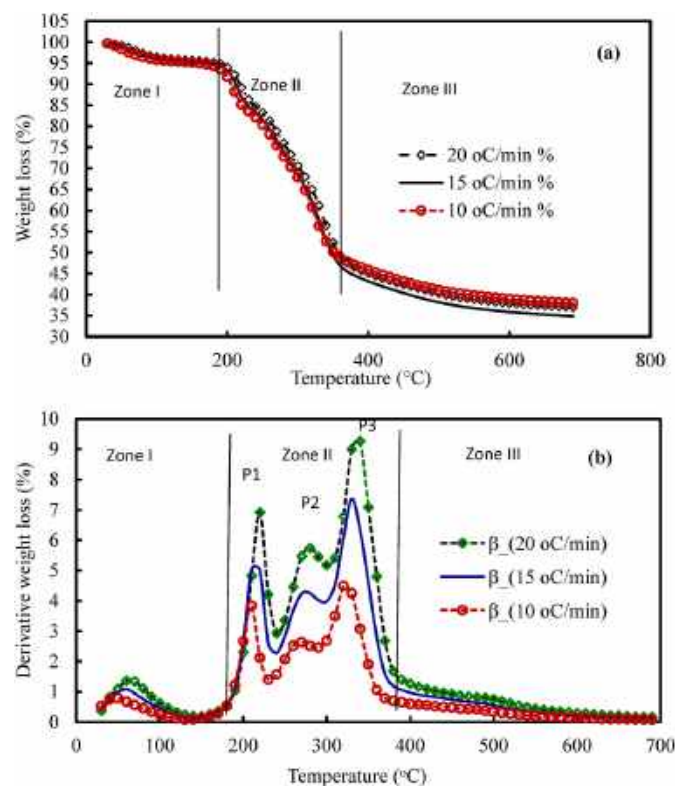


Fig. 1. (a) TG and (b) DTG curves of *Hyphaene thebaica* shell devolatilisation in nitrogen atmosphere at 10, 15 and 20 °C/min.

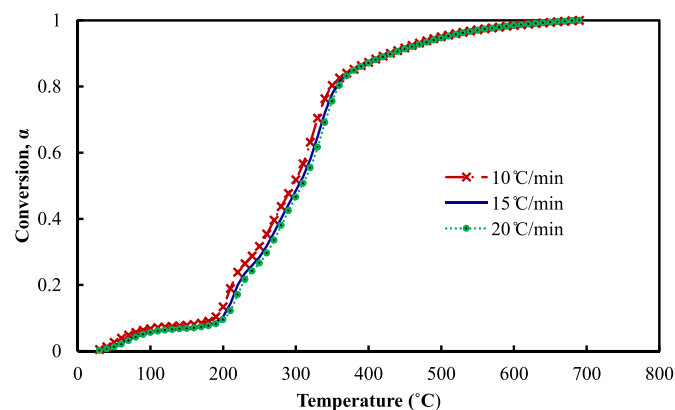


Fig. 2. Conversion, α vs temperature curve for pyrolysis of *Hyphaene thebaica* shell.

typically occurred during the thermal degradation of various biomass sources. The release of moisture and lighter volatiles hosted on the HTS macro-structure caused the first stage, which occurred between 32 °C and 180 °C. The drying zone, the first stage, is seen to have a minimal weight loss of 6.20 wt%. With a maximum weight loss of 54.36 wt%, the HTS considerably degraded in the second stage between 150 and 575 °C. This is due to the total decomposition of cellulose and hemicellulose with continuous heating. The peaks observed on the DTG curves between 190 °C and 380 °C belong to the degradation of hemicelluloses, extractives and celluloses. Multiple peak points represent multi-step reactions, and their number denotes the minimum necessary steps required for those reactions in the multi-step kinetic model [65]. The degradation proceeded through dehydration of methoxy and acetyl bond breakage of hemicellulose and cellulose [33]. The active pyrolytic zone, which is the second stage, is where the necessary volatiles are

released to produce bio-oils and gas.

The lignin-rich char residue saw a little weight loss in the last stage between 370 °C and 690 °C as a result of the breakdown of the glycosidic bonds of the lignin component of biochar. The final stage, which is typically referred to as the passive pyrolysis stage, has a total weight reduction of roughly 8.47 wt%. This is consistent with the results in the literature [66], which show that coconut shells with an elemental composition close to that of HTS display comparable thermal behaviour. Additionally, the thermal degradation behaviour of HTS is consistent with that of cork granules [19] and Mustad stalks [67]. Finally, the biochar of 37 wt% remains at 800 °C after the degradation of the residual lignin-rich char. This biochar would be a high-value carbon material that can serve as an energy precursor, adsorbent, catalyst support, and carbon-based sensor.

The heating rate influences the HTS decomposition, as observed on the DTG curves, which shifted towards a higher temperature region with the increase in heating rate without altering the decomposition profile, as shown in Fig. 1(b). A total weight loss of 49.2–51.15 wt% with the change in heating rate from 10 to 20 °C/min was recorded. At heating rates of 10, 15, and 20 °C/min, the maximum weight loss of HTS is 4.274, 7.368, and 9.00 wt%/min, respectively. For the thermal examination of palm kernel shells with compositions that are consistent with those on HTS, Hussain et al. [68] reported a comparable trend. When compared to other heating rates, the maximum weight loss and volatiles were produced in the active pyrolysis zone at a heating rate of 20 °C/min. The maximum peak of the DTG curves gradually shifted from 320 °C at 10 °C/min to 330 °C at 15 °C/min to 340 °C at 20 °C/min revealing the effect of the heating rate. With a short volatile residence time, the higher temperatures improved thermal energy and mass transfer. However, at a slower heating rate, the anisotropic heat transfers caused by the HTS's intricate microstructure occur with a significant time lag, severely limiting mass transfer.

3.4. Evaluation of the kinetics parameters of *Hyphaene thebaica* shell

The extent of conversion, α vs temperature curve was examined prior to the evaluation of kinetics parameters in order to assist in the selection of suitable models. Fig. 2 shows the conversion, vs. temperature graph. All heating rates result in a sigmoid curve. The kinetics committee of the International Confederation for Thermal Analysis and Calorimetry (ICTAC) asserts that power law models, which simulate accelerating and decelerating processes, cannot effectively represent this type of reaction curve [20].

The kinetic study aimed to evaluate the kinetic parameters of the decomposition of HTS through the pyrolysis process. The thermogravimetric data collected at three different heating rates (10, 15, and 20 °C/min) were used to calculate the kinetic parameters from the FWO, KAS, and Starink methods. The first stage data related to the moisture and light volatiles losses have little importance to the estimation of the kinetic parameters. Thus, the linear plots of KAS, FWO, and Starink methods, shown in Fig. 3 (a)–(c) are attributed to the conversion rate of the active pyrolysis stage related to the HTS structural degradation.

The plots indicated a change in slope, with the corresponding conversion ratio and activation energy shown in Table 4 and Fig. 4. The close proximity of the activation energy (E_a) values demonstrates the three techniques' suitability for predicting the kinetic parameters. The average activation energy obtained from FWO, KAS, and Starink methods are 142.81, 118.5, and 139.5644 kJ/mol, respectively. The activation energies of wheat straw, wheat dust, and corn cob, which range between 113 and 131 kJ/mol [37], and the activation energy of HTS, are comparable. The activation energy, which ranges from 91.64 kJ/mol to 104.43 kJ/mol in sugar cane bagasse, is higher. This is caused by sugarcane bagasse's high cellulose content, which requires less energy during pyrolysis. The increased activation energy of the poplar, 209 kJ/mol [39], compared to the HTS, may be a result of the wood's high lignin concentration. The HTS activation energy values are

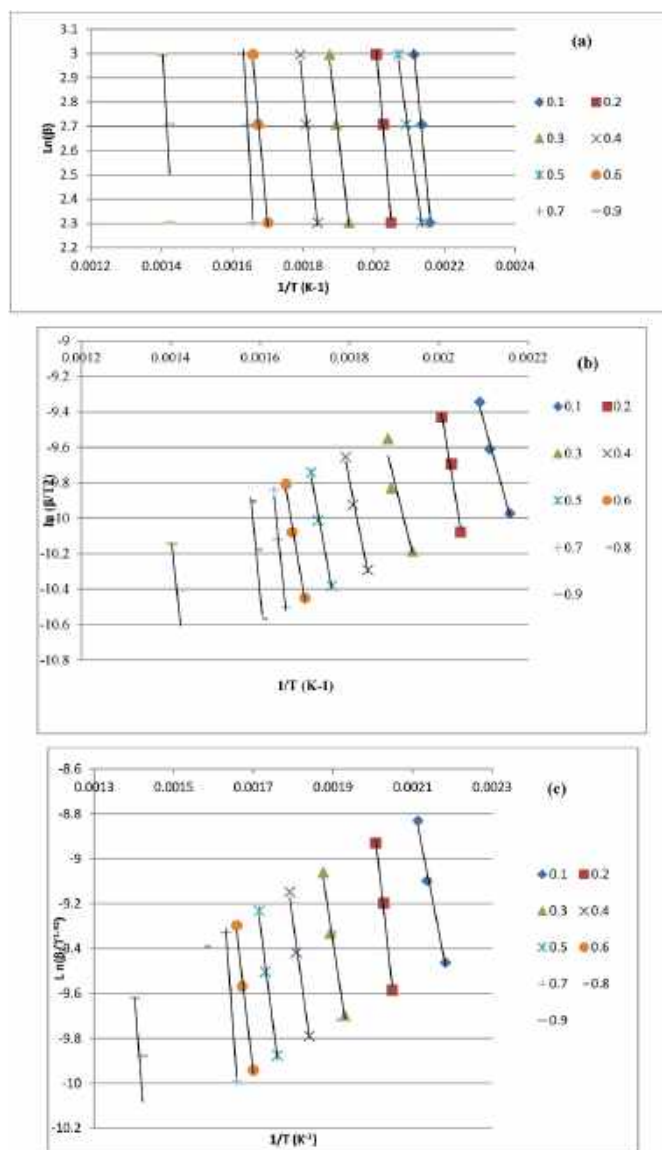


Fig. 3. Linear plots of (a) Linear plots of Flynn-Wall-Ozawa (FWO) (b) Linear plots of Kissinger-Akahira-Sunose (KAS) and (c) Starink model for pyrolysis of *Hyphaene thebaica* shell.

comparable to those of other biomass, including maize cob [37], wheat straw, wheat dust, cashew shell, and palm stem [69], as well as poplar wood [40]. This suggests that the HTS might be pyrolysed to produce bio-oil by devolatilising it at a moderate temperature. Because of the degradation of lignin in the biochar, the activation energies are larger when conversion is between 0.7 and 0.9 [70]. The E_a values increased

from 125 to 255 kJ/mol at conversion levels of 0.1–0.8, which may be related to the degradation of cellulose and hemicelluloses. The high variation of activation energy above 20% indicates that the pyrolysis of HTS is multi-step [20,65]. For the three Iso-conversional methods attributed to lignin degradation in biomass samples, E_a values decreased rapidly to around 192.44 kJ/mol for conversion rates greater than 0.8.

The values of the Akaike Information Criterion (AIC) of KAS, FWO, and Starink Iso-conversional models were 11.2023, 10.9258, and 10.9309, respectively. The smallest number indicates the method that fits best with the available data than the others. Thus, FWO is the best Iso-conversional method for the evaluation of kinetic data for the pyrolysis of *Hyphaene thebaica* shell.

Furthermore, the effective kinetic mechanisms that control the HTS pyrolysis could be established through the Coat-Redfern's (CR) method using the model-fitting technique. The kinetic parameters, such as activation energy (E_a) and pre-exponential factor (A), would be determined using CR reaction models fitted with experimental Temperature ($-T$) profiles. The model-fitting approach gives credible results because of its minimum error. In this study, the HTS decomposition through pyrolysis was analysed only in the active pyrolytic zone at a 10 °C/min heating rate. Table 5 shows the values of the kinetic parameters derived from the regression of $-T$ profiles of the various CR method models. The results revealed different values of E_a and A due to differences in the kinetic model used.

The model-fitting analyses with very high correlation coefficients (R^2) are considered the most suitable kinetic models for estimating the kinetic parameters. In this study, the R^2 values are in the range of 0.81–0.99, which indicates that the results of the kinetic analysis are credible. Therefore, from the R^2 values, it is confirmed that the mechanisms linked to the diffusion and contracting models are the most effective for describing the decomposition of HTS by pyrolysis. Precisely, the diffusion mechanisms D1-D4, contracting mechanisms

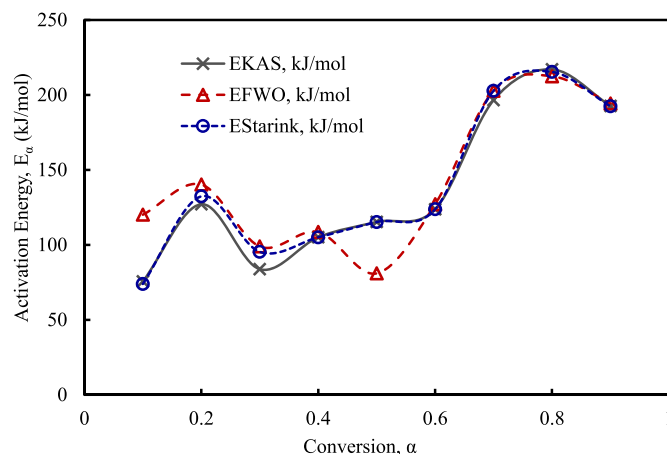


Fig. 4. Activation energy distribution of *Hyphaene thebaica* shell decomposition by pyrolysis from Iso-conversional methods.

Table 4

Kinetic parameters of devolatilisation of *Hyphaene thebaica* shell by pyrolysis from Iso-conversional methods.

Conversion (α)	E_{KAS} , kJ/mol	A (s^{-1})	R^2	E_{FWO} , kJ/mol	A (s^{-1})	R^2	$E_{Starink}$, kJ/mol	A (s^{-1})	R^2
0.1	75.58	1756129.649	0.9879	120.11	2.01E+10	0.9916	73.93	1237148.21	0.9880
0.2	127.09	85322649635	0.9860	140.21	1.29E+12	0.9916	132.34	2.53353E+11	0.9905
0.3	83.76	9951000.295	0.9885	98.91	2.41E+08	0.9902	95.32	113578040	0.9884
0.4	105.06	871492682.3	0.8917	108.56	1.81E+09	0.9902	105.03	867349914.5	0.9886
0.5	115.26	7311478773	0.9887	80.97	5515908	0.99	115.22	7257572466	0.9887
0.6	123.76	42808590702	0.9888	127.06	8.48E+10	0.9903	123.70	42290937445	0.9889
0.7	196.53	1.36203E+17	0.9806	202.67	4.79E+17	0.9914	202.76	4.87094E+17	0.9905
0.8	217.02	8.95727E+18	0.9905	212.43	3.51E+18	0.6351	215.32	6.33285E+18	0.5749
0.9	192.69	6.20805E+16	0.6340	194.35	8.73E+16	0.6611	192.44	5.90278E+16	0.6351
Average	118.15	1.01728E+18		142.81	4.08E+18		139.56	7.6433E+17	

Table 5Kinetic parameters of *Hyphaene thebaica* shell devolatilisation via pyrolysis from Coats-Redfern's Method.

Mechanisms	Models	Activation Energy, E_a (kJ/mol)	A (s^{-1})	R^2	AIC*	Relative Likelihood
Reaction						
(R ₁) First Order	$-\ln(1-\alpha)$	17.78	0.0483	0.8805	1.6955	0.0858
(R ₂) Second Order	$(1-\alpha)^{-1} - 1$	20.98	0.1637	0.8584	3.7135	0.0313
(R ₃) Third Order	$[(1-\alpha)^{-2} - 1]/2$	24.71	0.6563	0.8185	6.1355	0.0093
Diffusion						
(D ₁) One-way Transport	α^2	37.59	2.0527	0.9149	0.0184	0.1985
(D ₂) Two-way Transport	$\alpha + (1-\alpha)\ln(1-\alpha)$	39.16	1.8692	0.9161	-0.5387	0.2623
(D ₃) Three-way Transport	$1 - [(1-\alpha)/3]^2$	15.97	0.0159	0.8799	-0.2165	0.2233
(D ₄) Ginstling-Brounshtein Eq	$1 - 2\alpha/3 - (1-\alpha)^{2/3}$	39.75	3303.3649	0.916	-3.2153	1.0000
Nucleation						
(A ₄) Avrami-Erofe'ev 4	$[-\ln(1-\alpha)]^{1/4}$	1.010	7.9E-05	0.9905	-0.4480	0.2506
Contracting						
(C ₁) Area contracting	$1 - (1-\alpha)^{1/2}$	16.40	0.0141	0.9430	-0.5342	0.2617
(C ₂) Volume contracting	$1 - (1-\alpha)^{1/3}$	16.84	0.0112	0.9335	-1.0760	0.3431

AIC* = Akaike Information Criteria.

C1–C2, and nucleation A4 are the most feasible mechanisms that control the decomposition reactions. This conforms to the recommendation of the ICTAC kinetics committee, which suggests that Avrami-Erofe'ev 4 is a robust model that can describe deceleration, acceleration, and sigmoidal reaction systems [65]. These mechanisms agree reasonably well with those obtained for agricultural and forestry residues using the CR method under pyrolysis conditions reported in the literature [67]. On the contrary, the reaction mechanisms (F1–F3) with R^2 values of 81–84% could be limited in describing the decomposition step of HTS [56].

In addition, Akaike Information Criterion values for the kinetic models are presented in Table 4. The model with the smallest AIC and a relative likelihood of 1 best fits the available data compared to the others [70]. Thus, Ginstling-Brounshtein, which has an AIC value of -3.52 and a likelihood of 1, best fits the data from the pyrolysis of *Hyphaene thebaica* shell reported in this study. Other models that come close are volume and area contracting models with likelihoods of 0.34 and 0.26, respectively. Models such as Avrami Erofeev 4 and two-way diffusion models with relative likelihoods of 0.25 and 0.26, respectively, exhibited some extent of good fits.

3.5. Thermodynamics parameters for devolatilisation of *Hyphaene thebaica* under pyrolysis atmosphere

The thermodynamic parameters for the HTS pyrolysis calculated using Eqs. (21)–(24) are shown in Table 6. These values include enthalpy (H), entropy (S), and Gibb's free energy (G). Fig. 5(a)–(c) shows the profiles of the thermodynamic parameters with conversion.

The energy that breaks the structural bonds of HTS from the heat energy absorbed by its macro-molecules to generate the end products is referred to as the enthalpy change (H). The variations of ΔH with conversion from 0.1 to 0.9% are shown in Fig. 5(a), and the profiles for the three Iso-conversional procedures follow a similar trend (FWO, KAS, and

Starink methods). This outcome confirmed that endothermic processes oversaw the entire pyrolysis reactions, as indicated in Table 5 and Fig. 5 (a), where all of the ΔH are observed to be positive values. Particularly, the average values of ΔH calculated using the FWO, KAS, and Starink techniques are 137.795, 132.4, and 134.55 kJ/mol, respectively. These values are lower than those reported during mustard shell decomposition [67]. The difference between the ΔH and the E_a reveals how much energy is required for pyrolysis reactions. Given the high energy needed to pyrolyse a biomass source, a large difference means that the pyrolysis reaction is unlikely to occur. However, it was observed in this study that the average difference between the ΔH and the E_a in the case of HTS pyrolysis is approximately 5 kJ/mol. As a result, the HTS is susceptible to pyrolysis under moderate thermal energy and provides a unique biomass source. A similar small differential between ΔH and the E_a (5 kJ/mol) was required for the pyrolysis of Para grass to produce the desired products [71]. In contrast, it was anticipated that HTS and para grass might be pyrolysed into products with moderate energy.

Gibb's free energy (G) describes how the pyrolysis reactions proceed, and its values are beneficial for thermodynamic analysis. The profile of change in ΔG with conversion is presented in Fig. 5(b). The ΔG of the three Iso-conversional methods were observed to follow a similar pattern. The values decrease with a change in conversion towards the production of biochar. Moreover, Table 5 shows that the ΔG has positive values throughout the pyrolysis conversion process, and it varies with the extent of the conversion (E_w). The average ΔG values obtained from the FWO, KAS, and Starink methods are 152.0483, 151.7996 and 151.9543 kJ/mol, respectively. The values are also similar, indicating that the pyrolysis process would result in an energy production that is relatively constant. The positive values of the ΔG indicate that pyrolysis is an endothermic, irreversible process that does not occur naturally. Therefore, extrinsic thermal energy would be needed for the thermal degradation of HTS by pyrolysis in order to convert it into volatiles and biochar, similar as those biomass sources reported in the literature [21,

Table 6Thermodynamic parameters of devolatilisation of *Hyphaene thebaica* shell from pyrolysis.

Conversion (α)	KAS			FWO			Starink		
	ΔH (kJ/mol)	ΔG (kJ/mol)	ΔS (kJ/K)	ΔH (kJ/mol)	ΔG (kJ/mol)	ΔS (kJ/K)	ΔH (kJ/mol)	ΔG (kJ/mol)	ΔS (kJ/K)
0.1	70.57	154.73	-0.14	115.10	152.41	-0.06	68.92	154.84	-0.14
0.2	122.07	152.12	-0.05	135.19	151.63	-0.03	127.33	151.92	-0.04
0.3	78.75	154.21	-0.13	93.90	153.38	-0.10	90.31	153.57	-0.10
0.4	100.04	153.08	-0.09	103.55	152.91	-0.08	100.02	153.08	-0.09
0.5	110.24	152.61	-0.07	75.96	154.38	-0.13	110.21	152.62	-0.07
0.6	118.75	152.26	-0.06	122.04	152.13	-0.05	118.69	152.26	-0.06
0.7	191.51	149.94	0.07	197.66	149.78	0.08	197.75	149.78	0.08
0.8	212.01	149.44	0.10	207.42	149.55	0.10	210.31	149.48	0.10
0.9	187.67	150.04	0.06	189.34	149.99	0.07	187.42	150.04	0.06
Average	132.40	152.05	-0.03	137.80	151.80	-0.02	134.55	151.95	-0.03

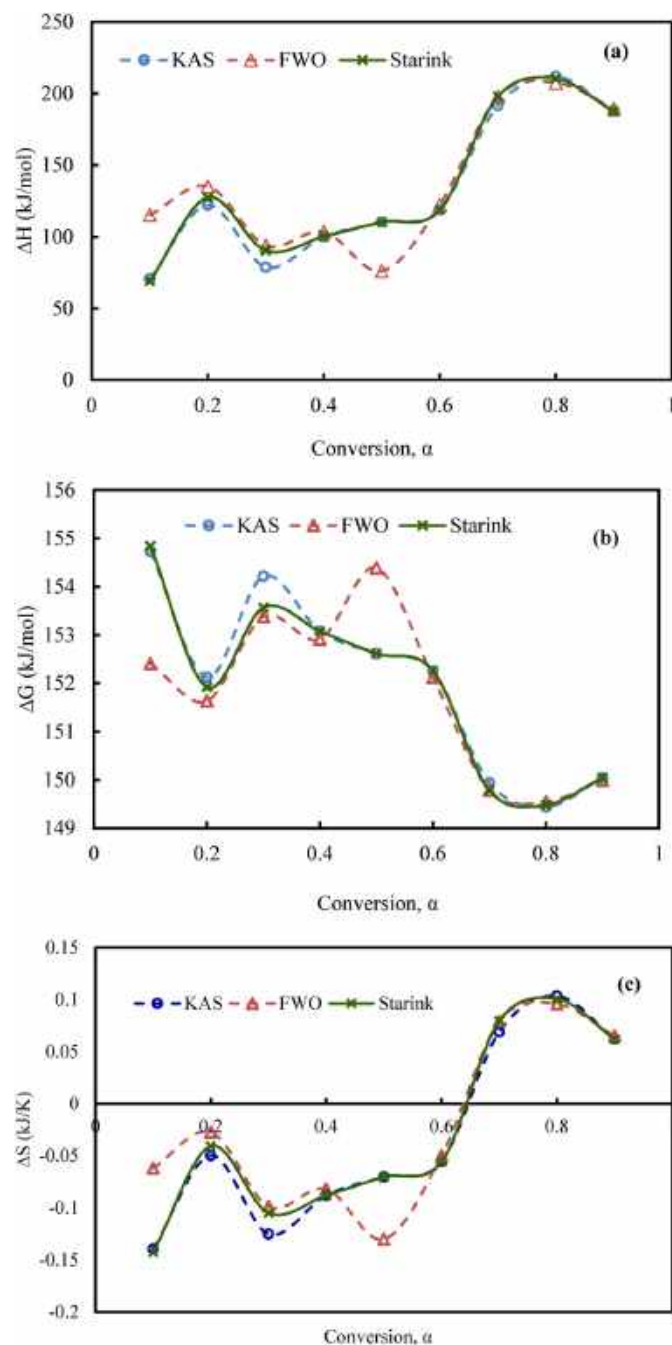


Fig. 5. Variation of (a) ΔH , (b) ΔG and (c) ΔS with extent of conversion for pyrolysis of *Hyphaene thebaica* shell.

39,56,67].

The degree of disorder in HTS when thermodynamic equilibrium is neared during the pyrolysis process is predicted by the entropy change (ΔS). Fig. 5(c) and Table 6 display the trend of S values produced by the KAS, FWO, and Starink techniques. The change in conversion affects the ΔS . This pattern suggests that HTS degrade in an inert atmosphere by a series of complex reactions, with ΔS almost certainly being negative. Additionally, because of the reduced bond dissociation, the products may exhibit less disorder than the reactants [72]. For conversion extents of 0.1–0.6, the ΔS values of the thermal decomposition of HTS are negative. This occurs because volatiles that are released lower the degree of disorder. The ΔS have positive values as a result of the 0.6 conversions, which is explained by the release of a few vapours during the production of biochar from lignin at a higher temperature. As the

pyrolysis nears completion, and biochar, which is more stable than the original biomass, is formed, a sharp increase in ΔS values can be observed. Higher reactivity and rapid activated compound formation are implied by high values of ΔS . At the end of the decomposition process, low values of ΔS might be related to only physical change and no chemical reactivity.

The complexity of the HTS decomposition via the pyrolysis process was therefore illustrated by the overall changes in the thermodynamic parameters with conversion, as shown in Fig. 5.

4. Conclusion and prospects

Pyrolysis was used to investigate the physicochemical and thermogravimetric properties of the *Hyphaene thebaica* shell (HTS). With a ratio of 1.55 H:C, 1.73 MJ/kg calorific value, and 74.31% volatile matter, it is established that HTS is suitable for pyrolysis to produce high-value bioenergy precursors. The macro-structures of lignin, cellulose, and hemicellulose were confirmed to have a presence comparable with other well-known biomass sources owing to the pertinent functional groups, such as aromatic rings, phenyl groups, aromatic stretches, and aryl-O stretches, determined via FTIR analysis. Thermogravimetric curves indicate that the HTS macro-structure degradation resulted in a maximum weight loss of 50.50 wt% in the pyrolysis zone between 190 and 390 °C. With higher heating rates, the decomposition behaviour remained consistent, but the maximal degradation peak changed to region with greater weight loss and temperature. According to Iso-conversional methods, Flynn-Wall-Ozawa, Kissinger-Akahira-Sunose and Starink models, the average activation energies for pyrolysis were 118.15, 142.81, and 139.56 kJ/mol, respectively. Using the Akaike information criteria (AIC), the Flynn-Wall-Ozawa method best fitted the pyrolysis data. The Coats-Redfern method's kinetic parameters demonstrated that the pyrolysis process was governed by complex multi-step reactions that were primarily controlled by diffusion and contraction mechanisms. In particular, the Gistling-Brounshtein kinetic, however, best fits the observed data based on the AIC, with the lowest AIC of -3.26 and the highest relative likelihood of 1. The viability of converting HTS through the pyrolysis process into high-value bioenergy feedstock in an environmentally friendly way was demonstrated by the reactivity ratio (VM/FC) of 6.12, E_a (103–233 kJ/mol), G (169–173 kJ/mol), and H (70.57–212.01 kJ/mol) and lower N (0.55%) and S (1.17%). The HTS degraded through non-spontaneous reactions with a high degree of randomness, according to the thermodynamic parameters. The resulting, irreversible, endothermic pyrolysis reactions propagate the HTS degradation.

CRediT authorship contribution statement

Habu Iyodo Mohammed: Conceptualization, Writing – original draft, and Editing. **Kabir Garba:** Supervision, Conceptualization, Writing – review & editing, of original drafted manuscript. **Saeed I. Ahmed:** Supervision, and editing of manuscript. **Lawan G. Abubakar:** Supervision, and editing of manuscript.

Declaration of competing interest

The authors declare that they have no known competing financial interests or personal relationships that could have appeared to influence the work reported in this paper.

Data availability

Data will be made available on request.

Acknowledgments

The authors gratefully acknowledged the support of the Tertiary

Education Fund of Nigeria under the National Research Grant (Project No: TETFund/DR&D/CE/NRF/2019/STI/49).

Appendix A. Supplementary data

Supplementary data to this article can be found online at <https://doi.org/10.1016/j.renene.2022.10.042>.

References

- [1] D. Singh, D. Sharma, S.L. Soni, C.S. Inda, S. Sharma, P.K. Sharma, A. Jhalani, A comprehensive review on 1st-generation biodiesel feedstock palm oil: production, engine performance, and exhaust emissions, *Bioenergy Res* 14 (2021), <https://doi.org/10.1007/s12155-020-10171-2>.
- [2] G. Kabir, B.H. Hameed, Recent progress on catalytic pyrolysis of lignocellulosic biomass to high-grade bio-oil and bio-chemicals, *Renew. Sustain. Energy Rev.* 70 (2016) 945–967, <https://doi.org/10.1016/j.rser.2016.12.001>.
- [3] C. Groves, M. Sankar, P.J. Thomas, Second-generation biofuels: exploring imaginaries via deliberative workshops with farmers, *J. Responsible Innov.* 5 (2018) 149–169, <https://doi.org/10.1080/23299460.2017.1422926>.
- [4] H.K. Jeswani, A. Chilvers, A. Azapagic, Environmental sustainability of biofuels: a review: environmental sustainability of biofuels, *Proc. R. Soc. A Math. Phys. Eng. Sci.* 476 (2020), <https://doi.org/10.1098/rspa.2020.0351>.
- [5] S. Ahmed, T. Warne, E. Smith, H. Goemann, G. Linse, M. Greenwood, J. Kedziora, M. Sapp, D. Kraner, K. Roemer, J.H. Haggerty, M. Jarchow, D. Swanson, B. Poulter, Systematic review on effects of bioenergy from edible versus inedible feedstocks on food security, *Npj Sci. Food.* (2021), <https://doi.org/10.1038/s41538-021-00091-6>.
- [6] F.H. Isikgor, C.R. Becer, Lignocellulosic biomass: a sustainable platform for the production of bio-based chemicals and polymers, *Polym. Chem.* 6 (2015) 4497–4559, <https://doi.org/10.1039/c5py00263j>.
- [7] T. Raj, M. Kapoor, R. Gaur, J. Christopher, B. Lamba, D.K. Tuli, R. Kumar, Physical and chemical characterization of various indian agriculture residues for biofuels production, *Energy Fuel.* 29 (2015) 3111–3118, <https://doi.org/10.1021/EF5027373>.
- [8] D. Czajczyńska, L. Anguilano, H. Ghazal, R. Krzyżyńska, A.J. Reynolds, N. Spencer, H. Jouhara, Potential of pyrolysis processes in the waste management sector, *Therm. Sci. Eng. Prog.* 3 (2017) 171–197, <https://doi.org/10.1016/j.tsep.2017.06.003>.
- [9] M. Ramanna, G. Subhosh, M. Madakka, Comparative Biochemistry and Kinetics of Microbial Lignocellulolytic Enzymes, Elsevier Inc., 2019, <https://doi.org/10.1016/B978-0-12-816328-3.00011-8>.
- [10] M. Tayyab, I. W. A. Noman, S. Waheed, Bioethanol production from lignocellulosic biomass by environment-friendly pretreatment methods: a review, *Appl. Ecol. Environ. Res.* 16 (2017) 225–249, <https://doi.org/10.15666/aer/1601>.
- [11] L.J.R. Nunes, J.C.O. Matias, J.P.S. Catalão, Biomass in the generation of electricity in Portugal: a review, *Renew. Sustain. Energy Rev.* 71 (2017) 373–378, <https://doi.org/10.1016/j.rser.2016.12.067>.
- [12] S.Y. Lee, R. Sankaran, K.W. Chew, C.H. Tan, R. Krishnamoorthy, D.-T. Chu, P.-L. Show, Waste to bioenergy: a review on the recent conversion technologies, *BMC Energy* 1 (2019) 1–23, <https://doi.org/10.1186/s42500-019-0004-7>.
- [13] C.A.V.B. de Sales, D.M.Y. Maya, E.E.S. Lora, R.L. Jaén, A.M.M. Reyes, A. M. González, R.V. Andrade, J.D. Martínez, Experimental study on biomass (eucalyptus spp.) gasification in a two-stage downdraft reactor by using mixtures of air, saturated steam and oxygen as gasifying agents, *Energy Convers. Manag.* 145 (2017) 314–323, <https://doi.org/10.1016/j.enconman.2017.04.101>.
- [14] A.R.K. Gollakota, N. Kishore, S. Gu, A review on hydrothermal liquefaction of biomass, *Renew. Sustain. Energy Rev.* 81 (2018) 1378–1392, <https://doi.org/10.1016/j.rser.2017.05.178>.
- [15] D.C. Elliott, P. Biller, A.B. Ross, A.J. Schmidt, S.B. Jones, Hydrothermal liquefaction of biomass: developments from batch to continuous process, *Bioresour. Technol.* 178 (2015) 147–156, <https://doi.org/10.1016/j.biortech.2014.09.132>.
- [16] S. Pourkarimi, A. Hallajisani, A. Alizadehdakhel, A. Nouralishahi, Journal of Analytical and Applied Pyrolysis Biofuel production through micro- and macroalgae pyrolysis – a review of pyrolysis methods and process parameters, *J. Anal. Appl. Pyrolysis* 142 (2019), 104599, <https://doi.org/10.1016/j.jaap.2019.04.015>.
- [17] P. Šimáček, J.J. Biernacki, S. Northrup, A.S. Mohammad, J.D. Murillo, J. J. Biernacki, S. Northrup, A.S. Mohammad, Biomass pyrolysis kinetics: a review of molecular-scale modeling contributions, *Braz. J. Chem. Eng.* 34 (2017) 1–18.
- [18] S. Ghysels, A.E. Estrada León, M. Pala, K.A. Schoder, J. Van Acker, F. Ronsse, Fast pyrolysis of mannan-rich ivory nut (*Phytelphas aequatorialis*) to valuable biorefinery products, *Chem. Eng. J.* 373 (2019) 446–457, <https://doi.org/10.1016/j.cej.2019.05.042>.
- [19] P.A. Costa, M.A. Barreiros, A.I. Mouquinho, P. Oliveira, F. Paradela, F.A. Costa, Slow pyrolysis of cork granules under nitrogen atmosphere: by-products characterization and their potential valorization, *Biofuel Res. J.* 33 (2022) 1562–1572, <https://doi.org/10.18331/BRJ2022.9.1.3>.
- [20] S. Vyazovkin, A.K. Burnham, J.M. Criado, L.A. Pérez-maqueda, C. Popescu, N. Sbirrazzuoli, Thermochimica Acta ICTAC Kinetics Committee recommendations for performing kinetic computations on thermal analysis data, *Thermochim. Acta* 520 (2011) 1–19, <https://doi.org/10.1016/j.tca.2011.03.034>.
- [21] M.S. Ahmad, M.A. Mehmood, S.T.H. Taqvi, A. Elkamel, C.G. Liu, J. Xu, S. A. Rahimuddin, M. Gull, Pyrolysis, kinetics analysis, thermodynamics parameters and reaction mechanism of *Typha latifolia* to evaluate its bioenergy potential, *Bioresour. Technol.* 245 (2017) 491–501, <https://doi.org/10.1016/j.biortech.2017.08.162>.
- [22] J. Chen, X. Fan, B. Jiang, L. Mu, P. Yao, H. Yin, X. Song, Pyrolysis of oil-plant wastes in a TGA and a fixed-bed reactor: thermochemical behaviors, kinetics, and products characterization, *Bioresour. Technol.* 192 (2015) 592–602, <https://doi.org/10.1016/j.biortech.2015.05.108>.
- [23] S.P. Bermejo, A. Prado-guerra, A. Isabel, P. García, L. Fernando, C. Prieto, Study of quinoa plant residues as a way to produce energy through thermogravimetric analysis and indexes estimation, *Renew. Energy* 146 (2020) 2224–2233, <https://doi.org/10.1016/j.renene.2019.08.056>.
- [24] I. Vitáček, M. Šotnar, S. Hrehová, K. Darnadyová, J. Mareček, Isothermal kinetic analysis of the thermal decomposition of wood chips from an apple tree, *Processes* 9 (2021) 1–10, <https://doi.org/10.3390/pr9020195>.
- [25] A. Palamanit, P. Khongphakdi, Y. Tirawanichakul, N. Phusunti, Investigation of yields and qualities of pyrolysis products obtained from oil palm biomass using an agitated bed pyrolysis reactor, *Biofuel Res. J.* 6 (2019) 1065–1079, <https://doi.org/10.18331/BRJ2019.6.4.3>.
- [26] M. Radojević, B. Janković, V. Jovanović, D. Stojiljković, N. Manić, Comparative pyrolysis kinetics of various biomasses based on model-free and DAEM approaches improved with numerical optimization procedure, *PLoS One* 13 (2018) 1–25, <https://doi.org/10.1371/journal.pone.0206657>.
- [27] Y. Zheng, J. Wang, C. Liu, Y. Lu, X. Lin, W. Li, Z. Zheng, Catalytic copyrolysis of metal impregnated biomass and plastic with Ni-based HZSM-5 catalyst: synergistic effects, kinetics and product distribution, *Int. J. Energy Res.* 44 (2020) 5917–5935, <https://doi.org/10.1002/er.5370>.
- [28] M. Ma, Y. Bai, J. Wang, P. Lv, X. Song, W. Su, G. Yu, Study on the pyrolysis characteristics and kinetic mechanism of cow manure under different leaching solvents pretreatment, *J. Environ. Manag.* 290 (2021), 112580, <https://doi.org/10.1016/j.jenvman.2021.112580>.
- [29] J.E. White, W.J. Catallo, B.L. Legendre, Biomass pyrolysis kinetics: a comparative critical review with relevant agricultural residue case studies, *J. Anal. Appl. Pyrolysis* 91 (2011) 1–33, <https://doi.org/10.1016/j.jaap.2011.01.004>.
- [30] L. Jiang, X.R. Yang, X. Gao, Q. Xu, O. Das, J.H. Sun, M.K. Kuzman, Pyrolytic kinetics of polystyrene particle in nitrogen atmosphere: particle size effects and application of distributed activation energy method, *Polymers* 12 (2020) 1–18, <https://doi.org/10.3390/polym12020421>.
- [31] M. Guida, H. Bouaik, E.M. L. A. Moubarik, A. Aboulkas, K. El harfi, A. Hannioui, Utilization of Starink approach and Avrami theory to evaluate the kinetic parameters of the pyrolysis of olive mill solid waste and olive mill wastewater, *J. Adv. Chem. Eng.* 7 (2017) 1–8, <https://doi.org/10.4172/2090-4568.1000155>.
- [32] X. Wang, X. Wang, G. Qin, M. Chen, J. Wang, Comparative study on pyrolysis characteristics and kinetics of lignocellulosic biomass and seaweed, *J. Therm. Anal. Calorim.* 132 (2018) 1317–1323, <https://doi.org/10.1007/s10973-018-6987-3>.
- [33] L. Wang, H. Lei, J. Liu, Q. Bu, Thermal decomposition behavior and kinetics for pyrolysis and catalytic pyrolysis of Douglas fir, *RSC Adv.* 8 (2018) 2196–2202, <https://doi.org/10.1039/c7ra12187c>.
- [34] L. Zhang, Z. Bao, S. Xia, Q. Lu, K.B. Walters, Catalytic pyrolysis of biomass and polymer wastes, <https://doi.org/10.3390/catal8120659>, 2018.
- [35] H. Siddiqi, S. Biswas, U. Kumari, V.N.V. Hima Bindu, S. Mukherjee, B.C. Meikap, A comprehensive insight into devolatilization thermo-kinetics for an agricultural residue: towards a cleaner and sustainable energy, *J. Clean. Prod.* 310 (2021), 127365, <https://doi.org/10.1016/j.jclepro.2021.127365>.
- [36] G. Kabir, A.T. Mohd Din, B.H. Hameed, Pyrolysis of oil palm mesocarp fiber and palm frond in a slow-heating fixed-bed reactor: a comparative study, *Bioresour. Technol.* 241 (2017) 563–572, <https://doi.org/10.1016/j.biortech.2017.05.180>.
- [37] S. Sohni, N.A.N. Norulaini, R. Hashim, S.B. Khan, W. Fadhullah, A.K. Mohd Omar, Physicochemical characterization of Malaysian crop and agro-industrial biomass residues as renewable energy resources, *Ind. Crop. Prod.* 111 (2018) 642–650, <https://doi.org/10.1016/j.indcrop.2017.11.031>.
- [38] S.A. El-Sayed, M. Khairy, Effect of heating rate on the chemical kinetics of different biomass pyrolysis materials, *Biofuels* 6 (2015) 157–170, <https://doi.org/10.1080/17597269.2015.1065590>.
- [39] A.K. Varma, P. Mondal, Physicochemical characterization and pyrolysis kinetic study of sugarcane bagasse using thermogravimetric analysis, *J. Energy Resour. Technol.* Trans. ASME 138 (2016) 1–11, <https://doi.org/10.1115/1.4032729>.
- [40] K. Slopiecka, P. Bartocci, F. Fantozzi, Thermogravimetric analysis and kinetic study of poplar wood pyrolysis, *Appl. Energy* 97 (2012) 491–497, <https://doi.org/10.1016/j.apenergy.2011.12.056>.
- [41] R.A. Aamer, Characteristics of aqueous doum fruit extract and its utilization in some novel products, *Ann. Agric. Sci.* 61 (2016) 25–33, <https://doi.org/10.1016/j.aos.2016.04.004>.
- [42] E.M. Abdallah, Screening of methanolic extract for antimicrobial activity of Hyphaene thebaica L. Fruit pulp from Sudanese folklores, *South Asian J. Res. Microbiol.* 9 (2021) 6–12, <https://doi.org/10.9734/SAJRM/2021/v9i130199>.
- [43] D.A. Ogbale, N. Ademoh, Development of A Doum palm shelling machine, *IOP Conf. Ser. Mater. Sci. Eng.* 1107 (2021), 012193, <https://doi.org/10.1088/1757-899x/1107/1/012193>.
- [44] S. Audu, S. Aje, T. Isuwa, S. Aji, Investigation of the impact, hardness, density and water absorption of polypropylene filled doum palm shell particles composite, *J. Inf. Eng. Appl.* 9 (2019) 28–37, <https://doi.org/10.7176/jiea/8-1-04>.

- [45] A.A. Alabi, A.I. Obi, D.M. Kulla, S.M. Tahir, Static and dynamic mechanical behavior of doum palm (*Hyphaene thebaica*) nut reinforced HDPE composites, *Niger. J. Technol.* 40 (2021) 639–647, <https://doi.org/10.4314/njt.v40i4.11>.
- [46] S. Samaila, H.M. Adamu, J.J. Deshi, Operation of linear microlaser arrays near 1 μm , 2 μm and 3 μm , *Int. Digit. Organ. Sci. Res.* 2 (2017) LT3, <https://doi.org/10.1364/assl.1994.lt3>.
- [47] U.I. Gaya, E. Otene, A.H. Abdullah, Adsorption of aqueous Cd(II) and Pb(II) on activated carbon nanopores prepared by chemical activation of doum palm shell, *SpringerPlus* 4 (2015) 1–18, <https://doi.org/10.1186/s40064-015-1256-4>.
- [48] D. Kongnine, P. Kpelou, N. Attah, E. Mouzou, Evaluation of energy properties of mixed biomass charcoal derived from coconut, palmyra palm nuts and doum palm nuts shells, *Sci. J. Energy Eng.* 9 (2021) 17, <https://doi.org/10.11648/j.sjee.20210902.11>.
- [49] M.E. Gibril, N. Zhang, Y. Yi, P. Liu, S. Wang, T. Tesfaye, F. Kong, Physicochemical characterization and future beneficiation routes of wild fruit waste (*Hyphaene Thebaica* seed) as a source to extract mannan, *J. Clean. Prod.* 267 (2020), 121949, <https://doi.org/10.1016/j.jclepro.2020.121949>.
- [50] A. Maisyarah, J. Shiun, F. Nasir, H. Hashim, Ultimate and proximate analysis of Malaysia pineapple biomass from MD2 cultivar for biofuel application, *Chem. Eng. Trans.* 63 (2018) 127–132, <https://doi.org/10.3303/CET1863022>.
- [51] T. Martí-Rosselló, J. Li, L. Leo, Kinetic models for biomass pyrolysis, *Archieve. Indust. Biotechnol.* 1 (2016) 4–7.
- [52] A. Saddawi, J.M. Jones, A. Williams, Kinetics of the thermal decomposition of biomass, *Energy Fuel.* 37 (2010) 1274–1282, <https://doi.org/10.1021/ef900933k>.
- [53] H. Li, S. Niu, C. Lu, Thermal characteristics and kinetic calculation of Castor oil pyrolysis, *Procedia Eng.* 205 (2017) 3711–3716, <https://doi.org/10.1016/j.proeng.2017.10.297>.
- [54] V.A. Profillidis, G.N. Botzoriz, in: *Akaike Information Criterion*, Akaike Inf. Criterion, 2019, pp. 1–16.
- [55] M. Mattheakis, P. Protopapas, Model selection & information criteria : Akaike information criterion, *Adv. Top. Data Sci. Protopapas, Rader.* (2018) 1–15.
- [56] C. Zhang, C. Wang, R. Tao, J. Ye, Thermal stability and thermal decomposition kinetics of Ginkgo biloba leaves waste residue, *Therm. Sci.* 22 (2018) 1059–1069, <https://doi.org/10.2298/TSCI170117154Z>.
- [57] C. Liu, H. Wang, P. Northwest, J. Sun, Catalytic fast pyrolysis of lignocellulosic biomass, *R. Soc. Chem.* (2014), <https://doi.org/10.1039/c3cs60414d>.
- [58] B. Biswas, N. Pandey, Y. Bisht, R. Singh, J. Kumar, T. Bhaskar, Pyrolysis of agricultural biomass residues: comparative study of corn cob, wheat straw, rice straw and rice husk, *Bioresour. Technol.* 237 (2017) 57–63, <https://doi.org/10.1016/j.biortech.2017.02.046>.
- [59] B. Khiari, I. Ghouma, A. Ibn, A. Amine, S. Jellali, Kenaf stems : thermal characterization and conversion for biofuel and biochar production, *Fuel* (2019), 116654, <https://doi.org/10.1016/j.fuel.2019.116654>.
- [60] L.M. Díaz-vázquez, A. Rojas-pérez, M. Fuentes-caraballo, I.V. Robles, U. Jena, Demineralization of *Sargassum* spp. macroalgae biomass : selective hydrothermal liquefaction process for bio-oil production, *Front. Energy Res.* 3 (2015) 1–11, <https://doi.org/10.3389/fenrg.2015.00006>.
- [61] Z. Liu, B.M. Jenkins, Y. Li, W. Yi, Influence of alkali and alkaline earth metallic species on the phenolic species of pyrolysis oil, *Bioresources* 12 (2017) 1611–1623.
- [62] M. Asadieraghi, W.M.A.W. Daud, In-depth investigation on thermochemical characteristics of palm oil biomasses as potential biofuel sources, *J. Anal. Appl. Pyrolysis* 115 (2015) 379–391, <https://doi.org/10.1016/j.jaap.2015.08.017>.
- [63] A. Bayu, D. Nandiyanto, R. Oktiani, R. Ragadhita, Indonesian journal of science & technology how to read and interpret FTIR spectroscopy of organic material, *Indones. J. Sci. Technol.* 4 (2019) 97–118.
- [64] A.B. Fadhil, B.A. Kareem, Co-pyrolysis of mixed date pits and olive stones: identification of bio-oil and the production of activated carbon from bio-char, *J. Anal. Appl. Pyrolysis* 158 (2021), 105249, <https://doi.org/10.1016/j.jaap.2021.105249>.
- [65] S. Vyazovkin, A.K. Burnham, L. Favergeon, N. Koga, E. Moukhina, L.A. Pérez-maqueda, N. Sbirrazzuoli, Thermochimica Acta ICTAC Kinetics Committee recommendations for analysis of multi-step kinetics, *Thermochim. Acta* 689 (2020), 178597, <https://doi.org/10.1016/j.tca.2020.178597>.
- [66] C.D. Liyanage, M. Pieris, A physico-chemical analysis of coconut shell powder, *Procedia Chem.* 16 (2015) 222–228, <https://doi.org/10.1016/j.proche.2015.12.045>.
- [67] S.L. Narnaware, N.L. Panwar, Bioresource Technology Reports Kinetic study on pyrolysis of mustard stalk using thermogravimetric analysis, *Bioresour. Technol. Reports.* 17 (2022), 100942, <https://doi.org/10.1016/j.biteb.2021.100942>.
- [68] M. Hussain, L.D. Tufa, S. Yusup, H. Zabiri, Thermochemical behavior and characterization of palm kernel shell via TGA/DTG technique, *Mater. Today Proc.* 16 (2019) 1901–1908, <https://doi.org/10.1016/j.matpr.2019.06.067>.
- [69] L. Wilson, W. Yang, W. Blasiak, G.R. John, C.F. Mhlu, Thermal characterization of tropical biomass feedstocks, *Energy Convers. Manag.* 52 (2011) 191–198, <https://doi.org/10.1016/j.enconman.2010.06.058>.
- [70] I.Y. Chen, Model Selection and Prediction AIC, Akaike information criterion, 2019.
- [71] M.S. Ahmad, M.A. Mehmood, O.S. Al Ayed, G. Ye, H. Luo, M. Ibrahim, U. Rashid, I. Arbi Nehdi, G. Qadir, Kinetic analyses and pyrolytic behavior of Para grass (*Urochloa mutica*) for its bioenergy potential, *Bioresour. Technol.* 224 (2017) 708–713, <https://doi.org/10.1016/j.biortech.2016.10.090>.
- [72] A.H. Rony, L. Kong, W. Lu, M. Dejam, H. Adidharma, K.A.M. Gasem, Y. Zheng, U. Norton, M. Fan, Kinetics, thermodynamics, and physical characterization of corn stover (*Zea mays*) for solar biomass pyrolysis potential analysis, *Bioresour. Technol.* 284 (2019) 466–473, <https://doi.org/10.1016/j.biortech.2019.03.049>.

Kinetics and Thermodynamic Parameters of Coffee Senna Seed (*Senna occidentalis*) Using Degradation Data from Roasting

Muhammad Zannah Lawan^{1*}, Idris Misau Muhammad², Isah Saeed Ahmed³,
Olubajo Olumide Olu⁴, Abdulkarim Abdulwadud Yusuf⁵, Ibrahim Maryam⁶

¹University of Maiduguri, Borno State, Nigeria

^{2,3,4,5,6}Abubakar Tafawa Balewa University, Bauchi, Nigeria

mz4chem@unimaid.edu.ng; engrmz15@gmail.com

Article Info:

Submitted:	Revised:	Accepted:	Published:
May 15, 2025	Jun 13, 2025	Jun 25, 2025	Jun 30, 2025

Abstract

Coffee Senna Seeds (CSS) have demonstrated potential as medicinal substitutes, warranting further investigation into their thermal stability for industrial applications. This study aims to establish the kinetic and thermodynamic parameters governing the thermal degradation of bioactive compounds in CSS across a temperature range of 100°C to 200°C and exposure durations of 5 to 30 minutes. Phytochemicals including cardiac glycosides, anthraquinones, phenols, flavonoids, saponins, steroids, alkaloids, terpenoids, tannins, and glycosides were analyzed to determine degradation profiles. FTIR and UV-Vis spectrophotometric analyses confirmed the decomposition of anti-nutritional components such as anthraquinones, while beneficial compounds like phenols, flavonoids, and saponins remained largely intact. Kinetic modeling indicated that the degradation followed a volume contraction mechanism, with high R^2 values (0.9804–0.9915) validating model fit. The low reaction order (0.28–0.397) suggests a diffusion-controlled process, while varying conversion factors (α) reflected complex internal

thermal dynamics within the seed matrix. Thermodynamic evaluation revealed the degradation process to be endothermic and non-spontaneous, with enthalpy (ΔH) values decreasing from 1585.90 to 754.50 kJ/mol and Gibbs free energy (ΔG) increasing from 102.92 to 130.18 kJ/mol as temperature rose. Negative entropy (ΔS) values, approximately -271.5 kJ/K, suggest a more ordered transition state, likely due to structural reorganization during roasting. Activation energy estimates ranged from 1589 to 758 kJ/mol, showing a decreasing trend with temperature, indicative of improved reaction feasibility at higher thermal inputs. These findings enhance understanding of CSS thermal behavior, supporting its detoxification and safer utilization in industrial processing.

Keywords: Coffee Senna Seed; Spectrophotometric Analyses; Roasting; Kinetics; Thermodynamics

INTRODUCTION

Coffee Senna (*Senna occidentalis*) is a leguminous plant widely found in tropical and subtropical regions (Khan *et al.*, 2015; Ayeni & Yakubu, 2020). Although traditionally considered a weed, recent studies have highlighted its potential for pharmacological and nutraceutical applications due to its rich phytochemical composition (Kaisar *et al.*, 2018; Akinmoladun *et al.*, 2020; Omoregie & Osagie, 2011; Ezeonu *et al.*, 2022). The increasing global interest in the utilization of underexploited plant resources for food and medicinal applications has brought attention to *Senna occidentalis* (commonly known as Coffee Senna), a leguminous plant with known bioactive compounds (Akinmoladun *et al.*, 2020; Adegbite *et al.*, 2022; Satish *et al.*, 2023). The seeds of Coffee Senna have traditionally been used in ethno-medicine and as potential coffee substitutes, but their inherent toxicity necessitates detoxification processes such as thermal treatment (Adebayo-Tayo *et al.*, 2009; Singh *et al.*, 2020; Akinyemi *et al.*, 2021). Understanding the thermal behavior of this biomass during roasting is essential for optimizing its use in medicinal and industrial applications. Roasting, a form of thermal treatment, can induce significant chemical transformations that influence the biological activity and safety profile of the seeds (Budarin *et al.*, 2011 Olaniran *et al.*, 2020; Akinyemi *et al.*, 2021). Roasting, a form of thermal processing, induces physicochemical changes in seeds and is a key method to reduce anti-nutritional factors while enhancing flavor and safety (Rehman *et al.*, 2020).

Thermal degradation of plant biomass such as Coffee Senna seeds can be effectively studied through roasting experiments at controlled temperatures and durations (Budarin *et al.*, 2011; Vyazovkin *et al.*, 2011; Akinyemi *et al.*, 2021). These experiments yield degradation-time data, which is crucial in determining the rate of mass loss and the progression of thermal decomposition (Budarin *et al.*, 2011; Ferdous *et al.*, 2020).

The mass loss data collected at incremental temperatures and times provide essential input for kinetic modeling. Studies by Bridgwater (2012) and Shen *et al.* (2009) have demonstrated that such thermal degradation data are crucial for understanding the decomposition stages of plant-based materials. Roasting alters the structural and chemical composition of the biomass and generates time-dependent conversion data that can be further analyzed to determine kinetic parameters (Budarin *et al.*, 2011; Son *et al.*, 2014). The extent of degradation is often quantified using mass loss measurements or degree of conversion under different thermal conditions (Vyazovkin *et al.*, 2011; Khawam & Flanagan, 2006).

Fourier-transform infrared spectroscopy (FTIR) and UV-Visible spectrophotometry are robust analytical techniques for identifying functional groups and quantifying bioactive compounds such as phenolics, flavonoids, and other antioxidants in plant matrices (Rohman & Windarsih, 2020). FTIR allows the detection of characteristic functional groups in complex biomolecules, indicating the presence of key phytochemicals, while UV-Vis spectrophotometry facilitates the quantitative assessment of compounds with conjugated double bonds such as phenolics (Ragazzi & Veronese, 2021). Therefore, characterizing these seeds using FTIR and UV-Vis spectrophotometry offers a promising strategy to elucidate the impact of roasting on their functional properties and medicinal potential.

Kinetic modeling of biomass decomposition is fundamental to elucidating reaction mechanisms and predicting behavior under different thermal conditions. The degree of conversion (α) is plotted against time (t) to form an empirical model. This model can then be used to fit classical kinetic models such as the Arrhenius equation and solid-state reaction mechanisms like the Avrami-Erofeev or contracting volume models (Vyazovkin & Wight, 1999; Jindal *et al.*, 2021). Non-linear regression, typically using the least squares method, is applied to determine the rate constant (k) and reaction order (n). A good model fit, indicated by a high R^2 value, reveals the underlying reaction mechanism that governs

decomposition (Ribeiro *et al.*, 2015). Kinetic modeling is fundamental in understanding the decomposition behavior of biomass during thermal processes. The kinetic behavior of biomass such as Coffee Senna seeds during roasting can be represented using solid-state kinetic models, which describe the relationship between the rate of conversion and temperature or time (Vyazovkin *et al.*, 2011).

Common models include first-order, Avrami-Erofeev, and contraction models, which can be fitted using non-linear regression techniques such as the least-square method (Šimković & Šajgalík, 2021). Empirical models may also be developed by plotting conversion (α) against time and deriving the degradation function, which when combined with theoretical kinetic expressions can yield parameters like the reaction rate constant (k) and reaction order (n) (Son *et al.*, 2014). In addition to kinetic modeling, the thermodynamic parameters of the roasting process - namely, activation energy (E_a), enthalpy (ΔH), entropy (ΔS), and Gibbs free energy (ΔG) - provide insight into the energy requirements and spontaneity of the reaction. These parameters are typically derived from Arrhenius and transition state theory equations (Khawam & Flanagan, 2006). A high activation energy suggests a more energy-intensive process, while positive Gibbs free energy indicates non-spontaneity unless facilitated by external heating.

According to Doyle (1961) and Ozawa (1992), evaluating these parameters aids in optimizing processing conditions for safe and efficient seed detoxification. Roasting significantly alters the chemical profile and bioactivity of Coffee Senna (*Senna occidentalis*) seeds through thermal degradation of bioactive compounds. However, the kinetics and thermodynamics of these changes remain unexplored. Existing studies lack a detailed kinetic model and thermodynamic evaluation of compound degradation under varying roasting conditions, highlighting a critical research gap. The thermal decomposition study of Coffee Senna seeds integrates experimental roasting, kinetic modeling, and thermodynamic evaluation to provide a comprehensive understanding of its behavior under heat. Such knowledge is vital for scaling up roasting processes, detoxification, and enhancing the bioactivity of *Senna occidentalis* seeds for industrial applications.

MATERIALS AND METHODS

Sample Collection and Preparation of Coffee Senna Seed (*Senna Occidentalis*)

Mature Coffee Senna Seeds (CSS) were harvested, sorted to eliminate foreign particles, washed thoroughly under running water, and dried under ambient conditions for 48 hours. The dried seeds were divided into six representative batches and roasted in a coffee roaster at predetermined temperatures: 100°C, 120°C, 140°C, 160°C, 180°C, and 200°C for time intervals ranging from 5 to 30 minutes. Each batch was cooled to room temperature in a desiccator and stored in airtight containers prior to further analysis (Akubor & Ogu, 2018; Abioye *et al.*, 2021).

Experimental degradation-time data of CSS

To assess thermal degradation, approximately 100 g of each seed sample was weighed before and after roasting. Experiments were conducted within a temperature range of 100°C to 200°C, with roasting durations varying from 5 to 30 minutes, performed in duplicate (Gaur *et al.*, 2022). The mass loss, representing thermal degradation and biomass conversion, was determined using Equation (1):

$$\alpha = \frac{m_o - m_t}{m_o - m_f} \quad \dots (1)$$

where m_o and m_f are initial and final masses of the CSS before and after roasting, while m_t is the mass at any time t during roasting.

Ultraviolet-Visible (UV-Vis) spectrophotometry of CSS

Aqueous extracts of the roasted grinded seeds were prepared by macerating 1 g of each sample in 20 mL of distilled water and filtering the mixture after 24 hours. The filtrates were analyzed using a UV-Vis spectrophotometer (Shimadzu UV-1800) in the wavelength range of 200 - 800 nm. The absorbance peaks indicative of chromophoric functional groups and bioactive compounds (such as anthraquinones) were identified and compared across different roasting temperatures (Eze & Obi, 2023).

Fourier transform infra-red (FTIR) of CSS

The chemical structure and functional groups of roasted powdered CSS were characterized using FTIR spectroscopy (PerkinElmer Spectrum Two). Dried and powdered seed samples

(2 mg) were mixed with KBr (200 mg) and compressed into pellets. Spectra were recorded in the range of 4000 - 400 cm^{-1} at a resolution of 4 cm^{-1} . Functional groups were identified based on standard absorbance bands and compared with unroasted controls (Zhang *et al.*, 2020; Isah *et al.*, 2022).

Kinetic models for the thermal decomposition of CSS

To determine the most suitable kinetic model describing the thermal decomposition of Coffee Senna seeds, an empirical model was developed using experimental data obtained from the roasting process. The relationship between the conversion factor (α) and time (t) was established from the data. Subsequently, the rate of conversion ($d\alpha/dt$) was calculated (Kebede *et al.*, 2023).

This rate expression was fitted to the standard kinetic model form, $k(1 - \alpha)^n$, using a non-linear regression approach aimed at minimizing the mean square error. The kinetic parameters, specifically the rate constant (k) and the reaction order (n), were determined using the Solver optimization tool in Microsoft Excel (Vyazovkin *et al.*, 2011; Doyle, 1961). The kinetic models for the roasting of CSS. The kinetic models for the roasting process of CSS were derived using the correlations presented in Equations 2 to 8. The stoichiometry and kinetics model for isothermal devolatilization of biomass presented as Equations (2) and (3) respectively, was previously reported in the literature.

$$\text{Biomass} = \text{Volatiles} + \text{Biochar} \quad \dots (2)$$

The kinetics model for isothermal devolatilisation of biomass, the reaction rate, $\frac{d\alpha}{dt}$, where α is the conversion or fraction decomposed, is often expressed as:

$$\frac{d\alpha}{dt} = k(T)f(\alpha) \quad \dots (3)$$

Where $k(T)$ is the temperature-dependent rate constant and $f(\alpha)$ is the reaction model dependent on the conversion α (Vyazovkin *et al.*, 2020). The rate constant $k(T)$ is defined by the Arrhenius equation:

$$k(T) = A \exp\left(-\frac{E}{RT}\right) \quad \dots (4)$$

Where, A is the pre-exponential factor (frequency factor), E_a is the activation energy (J/mol), R is the universal gas constant (8.314 J/mol·K), and T is the absolute temperature (K) (Liu *et al.*, 2022).

Accurate estimation of these parameters allows for prediction of thermal stability and decomposition pathways of materials including biomass and seeds (Kumar *et al.*, 2023). The conversion of biomass is obtained from Equation (5).

$$\alpha = \frac{m_o - m_t}{m_o - m_f} \quad \dots (5)$$

where m_o and m_f are initial and final masses of the CSS before and after roasting, while m_t is the mass at any time t during roasting.

Then, the unconverted biomass is calculated from $(1 - \alpha)$, rate equation depends on temperature, and un-converted biomass.

The rate constant, k is function of temperature and generally represented by the Arrhenius equation and $f(\alpha)$ is expressed inform of reaction order model, Equation (6).

$$\frac{d\alpha}{dt} = (1 - \alpha)^n k(T) \quad \dots (6)$$

$$k(T) = A \exp\left(-\frac{E}{RT}\right) \quad \dots (7)$$

Substituting Equation (23) into (20) yields Equation (24).

$$\frac{d\alpha}{dt} = A \exp\left(-\frac{E}{RT}\right) f(\alpha) \quad \dots (8)$$

Where t is the time, T is the temperature, α is the extent of reaction and $f(\alpha)$ is reaction model.

The derived parameters were then compared with established solid-state kinetic models to evaluate the goodness of fit. The analysis revealed that the experimental data closely aligned with the volume contraction mechanism. This indicated that the thermal decomposition of Coffee Senna seeds followed a contracting geometry model, a result that was consistent with findings from previous studies on similar plant-derived materials.

Thermodynamic analysis of CSS

Thermodynamic parameters such as enthalpy change (ΔH), entropy change (ΔS), and Gibbs free energy change (ΔG) were calculated using the following relationships derived from transition state theory in Equation (9) to (11).

$$\nabla H = E - RT_m \quad \dots (9)$$

$$\nabla G = E + RT_m \ln \left(\frac{K_B T_m}{hA} \right) \quad \dots (10)$$

$$\nabla S = \frac{\nabla H - \nabla G}{T_m} \quad \dots (11)$$

RESULTS AND DISCUSSION

Degradation-Time Data for Roasted Coffee Senna Seeds

The experimental data obtained from roasting Coffee Senna (*Senna occidentalis*) seeds at various temperatures and durations. The initial mass for all samples was 100 grams. Each experiment was conducted in duplicate is presented in Table 1.

Table 1: Roasting Data of Coffee Senna Seeds at Varying Temperatures and Times

Temperature (°C)	Time (min)	Final Mass 1 (g)	Final Mass 2 (g)
100	5	98.5	98.3
100	10	97.8	97.9
100	15	97.0	96.8
100	20	96.1	96.3
100	25	95.6	95.4
100	30	94.8	94.7
120	5	97.4	97.6
120	10	96.2	96.4
120	15	95.0	95.2
120	20	93.5	93.7
120	25	92.1	92.4
120	30	90.8	91.0
140	5	95.9	96.1
140	10	94.2	94.0
140	15	92.1	92.4
140	20	90.5	90.7
140	25	88.0	88.2
140	30	85.6	85.8
160	5	94.2	94.4
160	10	92.0	91.9
160	15	89.2	89.4
160	20	86.3	86.5
160	25	83.1	83.4

Temperature (°C)	Time (min)	Final Mass 1 (g)	Final Mass 2 (g)
160	30	80.0	80.3
180	5	92.0	92.2
180	10	89.0	89.2
180	15	85.4	85.7
180	20	81.6	81.8
180	25	77.8	78.0
180	30	74.2	74.0
200	5	90.1	90.3
200	10	86.2	86.4
200	15	82.0	82.2
200	20	78.0	78.3
200	25	74.0	74.1
200	30	70.2	70.0

The roasting data of *Coffee Senna* (*Senna occidentalis*) seeds at varying temperatures and durations shows a consistent trend of mass reduction with increasing temperature and roasting time. At lower temperatures (100°C and 120°C), the mass loss is relatively minimal, ranging from ~98.5 g to ~90.8 g across 30 minutes. However, as the temperature increases to 140°C, 160°C, 180°C, and finally 200°C, the mass loss becomes more pronounced, with the final mass dropping as low as ~70.0 g at 200°C for 30 minutes. This indicates a progressive loss of moisture and volatile compounds, consistent with thermal decomposition kinetics typically observed during roasting processes. The trend is in agreement with findings by Ajiboye *et al.* (2021), who reported similar mass reductions in roasted *Senna occidentalis* seeds, attributing the weight loss primarily to moisture evaporation and decomposition of bioactive compounds such as glycosides and alkaloids.

Moreover, Onwordi *et al.* (2015) demonstrated that increased roasting temperature leads to structural breakdown of seed matrices and volatilization of phytochemicals, a process critical to detoxification and flavor enhancement. These results also align with the thermal degradation profiles reported by Okoye *et al.* (2018), where increased temperature and time led to significant mass loss in legumes due to both physical and chemical changes, such as Maillard reactions, caramelization, and breakdown of anti-nutritional factors. The progressive roasting observed here is a crucial pre-treatment step for improving the safety, digestibility, and functional application of *Senna occidentalis* seeds in medicinal use. Thus, the roasting behavior observed in this study confirms the thermally sensitive nature of *Coffee Senna* seeds and supports the establishment of kinetics model and evaluation of thermodynamic parameters to balance detoxification and nutrient preservation.

Ultraviolet-Visible (UV-Vis) Spectrophotometry of CSS

Ultraviolet-Visible (UV-Vis) spectrophotometry was employed to investigate the phytochemical characteristics of aqueous extracts from roasted Coffee Senna Seeds (CSS). The analysis comprised both qualitative screening for the presence of key phytochemicals and quantitative determination of their concentrations (g/100 g of extract). The qualitative assessment provided insight into the types of bioactive compounds present, while the quantitative evaluation enabled the measurement of specific phytochemical constituents such as phenolics, flavonoids, and tannins, which are indicative of the seeds' medicinal potential. The results reflect the influence of roasting on the expression and concentration of these bioactive compounds.

Table 2. Qualitative Phytochemicals Screening of Aqueous Extracts

Phytochemicals	Samples					
	T100	T120	T140	T160	T180	T200
Cardiac glycosides	++	+	-	+++	+	+
Anthraquinones	++	+	+	++	+	-
Phenols	+++	+++	+++	+++	+++	+++
Flavonoids	++	+	+	+++	++	+
Saponins	+++	+++	+	+++	++	+
Steroids	+	+	-	++	+	-
Alkaloids	++	+	+	++	+	+
Terpenoids	++	+	-	+	+	-
Tannins	+++	++	+	+++	++	+
Glycosides	++	+	+	+++	+	+

Key: + = Slightly present. ++ = Present. +++ = Highly Present. - = Absent

The phytochemical profile of Coffee Senna Seeds (CSS) roasted at different temperatures (100°C to 200°C) revealed variable presence of key bioactive constituents, indicating that the roasting process significantly influences the phytochemical composition of the seeds (Table 2). Phenols and tannins were consistently detected across all roasting temperatures and remained highly present (+++) even at elevated conditions, suggesting their thermal stability. This aligns with the findings of Kebede *et al.* (2023), who reported that phenolic compounds in thermally processed legumes exhibit resilience due to their robust aromatic structures. Similarly, saponins demonstrated high thermal resistance, maintaining strong presence (++ to +++) across all samples, which supports observations by Adegbite *et al.* (2020) that saponins can withstand moderate to high thermal conditions without significant degradation. Conversely, other phytochemicals such as anthraquinones, flavonoids, steroids, terpenoids, and alkaloids showed temperature-sensitive behavior. For instance,

anthraquinones were moderately present at lower temperatures (T100 - T160) but diminished and became undetectable at 200°C, indicating thermal decomposition at elevated roasting levels. This pattern corroborates previous reports by Obasi *et al.* (2022); Olalekan and Uchenna (2021), which highlighted the susceptibility of volatile and semi-volatile phytochemicals to degradation at higher roasting temperatures. In contrast, excessive roasting at 200°C resulted in diminished presence or complete absence of several phytochemicals, reflecting possible thermal denaturation. Such findings underscore the importance of optimizing roasting conditions to retain or enhance beneficial phytochemicals in functional medicinal applications. Overall, the roasting process was shown to play a dual role: promoting the release of heat-stable compounds while simultaneously degrading heat-labile ones, consistent with prior studies on thermally processed phytochemical-rich seeds and legumes. Table 3 present the phytochemicals composition of the aqueous extracts.

Table 3. Quantitative Phyto-chemicals Composition of Aqueous Extracts (g/100g)

Phyto-chemicals	Samples					
	T100	T120	T140	T160	T180	T200
Cardiac glycosides	2.265	1.695	0.063	3.470	2.135	7.845
Anthraquinones	2.155	0.745	0.570	1.540	0.815	0.330
Phenols	27.230	21.345	16.350	28.740	19.895	17.340
Flavonoids	12.135	7.040	4.365	16.630	8.665	6.910
Saponins	11.920	8.900	6.375	10.330	9.555	8.810
Steroids	0.455	0.230	0.0355	0.310	0.074	0.0225
Alkaloids	16.065	9.175	7.350	12.155	8.745	6.570
Terpenoids	1.270	0.745	0.036	1.340	0.620	0.0225
Tannins	12.135	8.965	7.350	13.135	6.920	8.015
Glycosides	3.295	1.980	0.360	2.710	1.975	1.515

The roasting of Coffee Senna Seeds (CSS) across a temperature range of 100°C to 200°C significantly influenced the concentration of key phytochemicals in the aqueous extracts (Table 3). Roasting altered the thermal stability of bioactive compounds, leading to variations in their levels as temperature increased. At moderate roasting temperatures (T160), most phytochemicals such as cardiac glycosides (3.470 g/100 g), phenols (28.740 g/100 g), flavonoids (16.630 g/100 g), and tannins (13.135 g/100 g) were recorded at relatively high concentrations compared to other temperatures. This suggests that

roasting at 160°C potentially enhances the extractability or transformation of precursor compounds into active forms.

Similarly, alkaloids and saponins peaked at 16.065 g/100 g and 11.920 g/100 g respectively at T100, indicating higher retention at lower roasting levels. Conversely, higher roasting temperatures (T180 - T200) led to a marked decline in the content of thermo-labile compounds such as anthraquinones, steroids, and terpenoids, possibly due to thermal degradation. For instance, anthraquinones dropped from 2.155 g/100 g at T100 to 0.330 g/100 g at T200, and terpenoids decreased significantly from 1.270 g/100 g to 0.0225 g/100 g across the same range. These findings align with previous research indicating that moderate thermal treatment can enhance phytochemical availability through cell wall breakdown and enzymatic inactivation, whereas excessive heat may degrade sensitive compounds (Nwokocha *et al.*, 2022; Murthy & Naidu, 2021). Specifically, Murthy and Naidu (2021) noted that optimal roasting temperatures improve antioxidant activity in plant seeds by enhancing phenolic content, while extreme temperatures result in oxidative degradation of flavonoids and anthraquinones.

Fourier Transform Infra-red (FTIR) of CSS

The influence of roasting on the functional groups and molecular fingerprint of coffee senna seeds was examined as presented in Table 4.

Table 4: FTIR extracted peaks

No.	Wavenumber (cm ⁻¹)	Intensity	Bond Vibration	Functional Group
1	1028.75	83.22461	C–O Stretch	Ether or Ester
2	1237.48	92.24601	C–N Stretch	Amines or Amides
3	1394.02	92.19784	C–H Bending/Deformation	Aliphatic Hydrocarbons
4	1535.66	91.83297	N–H Bending/Aromatic Ring Vibrations	Amides / Aromatics
5	1632.57	90.66308	C=C Stretch	Alkenes or Aromatics
6	1744.39	96.62337	C=O Stretch	Carbonyl Groups (Ketones, Aldehydes/Esters)
7	2922.23	94.72603	C–H Stretch	Aliphatic Hydrocarbons
8	3280.06	94.08907	O–H or N–H Stretch	Hydroxyl Groups (Alcohols, Phenols)/ Amines

Roasting Coffee Senna Seeds (CSS) at temperatures ranging from 100°C to 200°C for durations of 5 to 30 minutes significantly influenced the functional group transformations, as revealed by the FTIR spectral data presented in Table 4. The observed peaks correspond to a variety of important phytochemical classes, indicating thermal modification of bioactive components during roasting. The presence of strong absorption bands at 1744.39 cm^{-1} and 1632.57 cm^{-1} correspond to C=O and C=C stretching vibrations, suggesting the presence of carbonyl and unsaturated compounds such as aldehydes, ketones, and aromatics, which are often enhanced or generated through Maillard reactions and thermal degradation of complex biomolecules during roasting (Adeyemi *et al.*, 2022). Similarly, the broad peak at 3280.06 cm^{-1} is indicative of hydroxyl (–OH) and amine (–NH) groups, typically associated with alcohols, phenolics, and proteins.

This peak remained prominent after roasting, suggesting the retention or partial transformation of antioxidant-rich hydroxyl compounds (Osabor *et al.*, 2020). The sharp peak at 2922.23 cm^{-1} corresponds to aliphatic C–H stretching vibrations, indicating the presence of long-chain hydrocarbons, which are common in plant oils and may be thermally concentrated during roasting. Moreover, the peaks at 1237.48 cm^{-1} and 1028.75 cm^{-1} , associated with C–N and C–O stretching respectively, reflect the contribution of amino and ether-containing compounds that are thermally modified from proteins and carbohydrates.

These findings are consistent with previous reports where thermal treatments in the 150–200 °C range led to significant rearrangements in the chemical structure of plant-based materials, enhancing aromaticity and bioactive compound availability (Fayemiwo *et al.*, 2021). Additionally, the emergence and intensification of certain bands post-roasting supports the hypothesis that controlled thermal treatment not only preserves but may also enhance the release of functional groups relevant to medicinal properties. Overall, the FTIR spectra demonstrate that the roasting process alters the molecular structure of CSS, promoting the formation and transformation of key bioactive compounds, which is crucial for optimizing its medicinal potential.

Establishment of the Kinetic Models for the Thermal Decomposition of Coffee Senna Seeds

To determine the most appropriate kinetic model describing the thermal decomposition of *Coffee Senna* seeds, an empirical model was developed from roasting experimental data, establishing the relationship between the conversion factor (α) and time (t) as presented in Figure 1 to 6. Subsequently, the rate of conversion $\frac{d\alpha}{dt}$ was evaluated. This rate expression was then fitted against the standard kinetic model form $k(1 - \alpha)^n$ using a non-linear regression approach based on the minimization of mean square error. The kinetic parameters, namely the rate constant (k) and reaction order (n), were obtained using the Solver optimization tool in Microsoft Excel (Doyle, 1961; Vyazovkin *et al.*, 2011).

The obtained parameters were further compared with established solid-state kinetic models to determine the best fit. The resulting model demonstrated a strong agreement with the volume contraction mechanism, suggesting that the thermal decomposition of Coffee Senna Seeds is governed by a contracting geometry process, a finding consistent with previous studies on similar plant-based materials (Kebede *et al.*, 2023).

Empirical Kinetic Modeling of Coffee Senna Seeds Decomposition

The kinetic model relating the conversion factor (α) and time (t) at 100°C, 120°C, 140°C, 160°C, 180°C and 200°C and 5, 10, 15, 20, 25 and 30 mins are described in Figure 1 to 6.

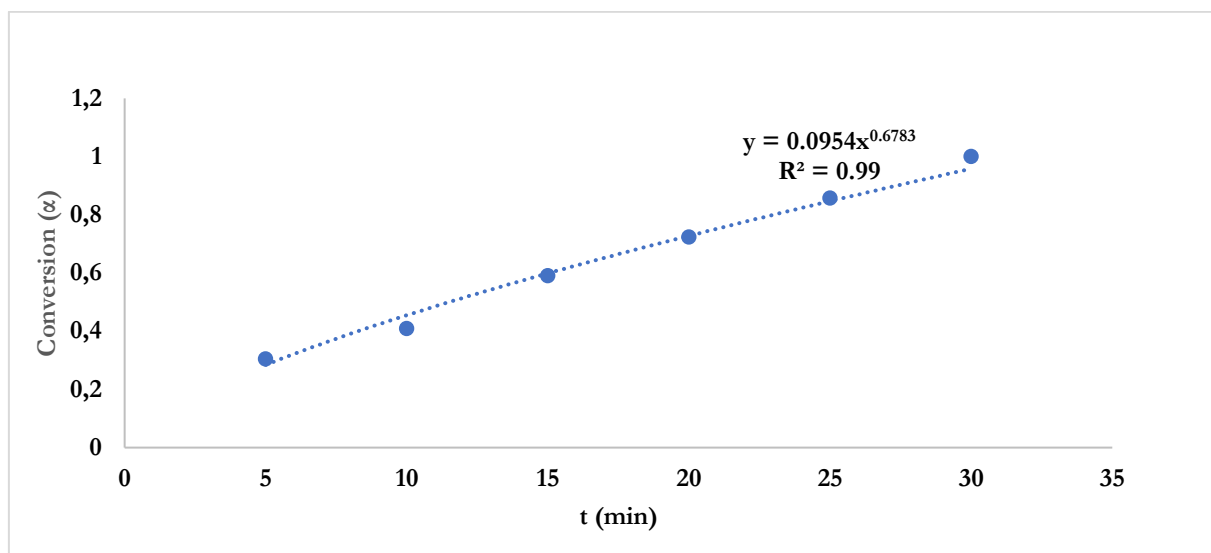


Figure 1: Conversion Fraction and Time During the Thermal Decomposition of CSS at 100°C

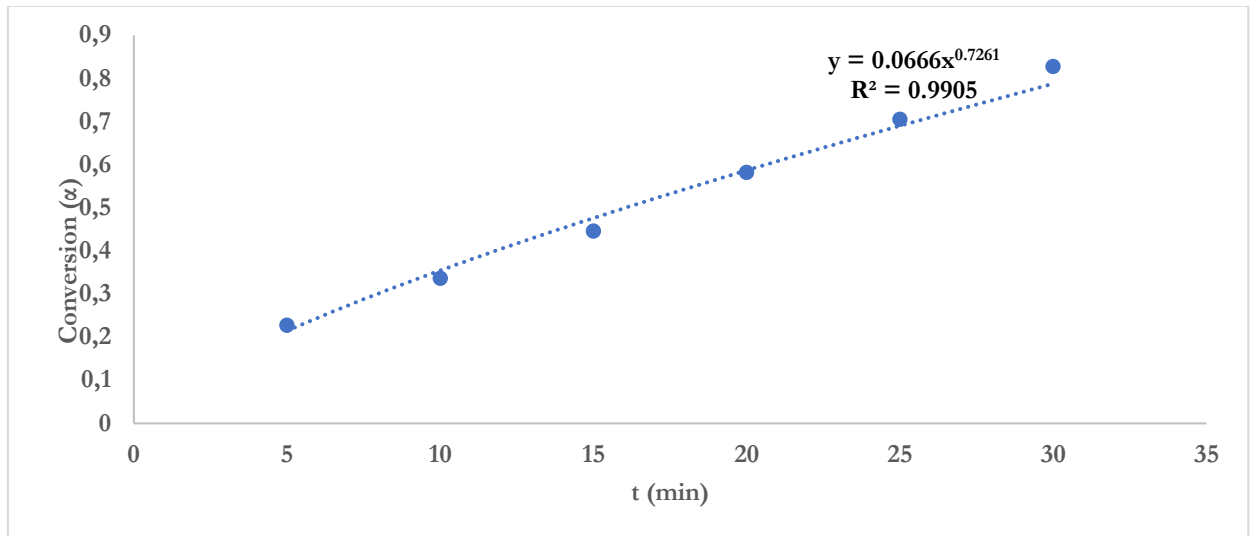


Figure 2: Conversion Fraction and Time During the Thermal Decomposition of CSS at 120°C

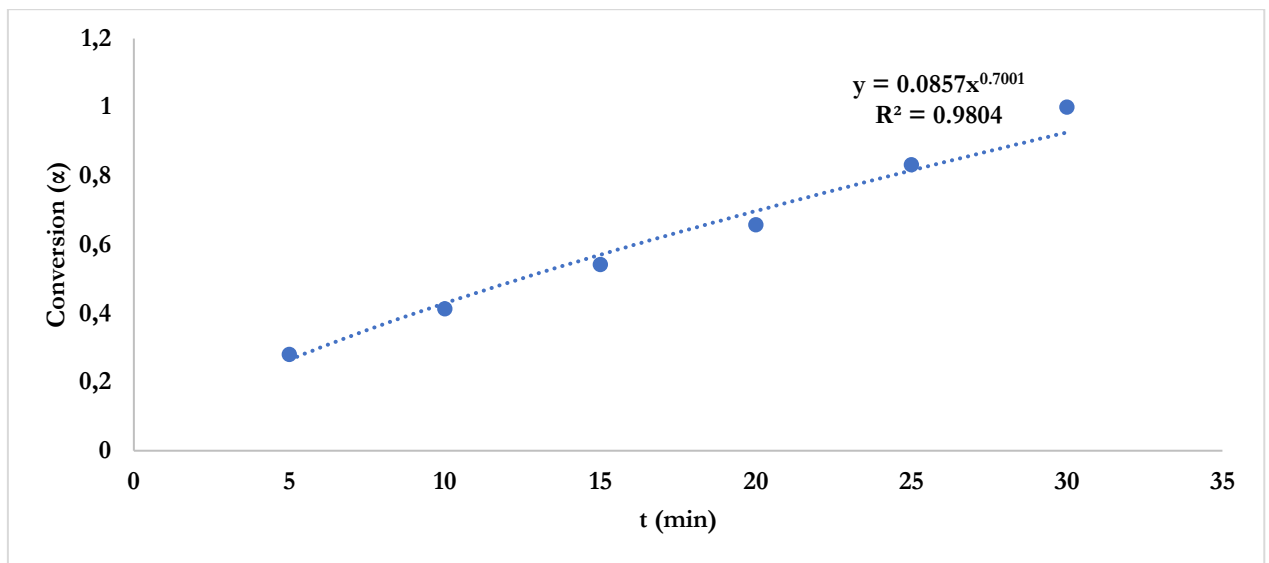


Figure 3: Conversion Fraction and Time During the Thermal Decomposition of CSS at 140°C

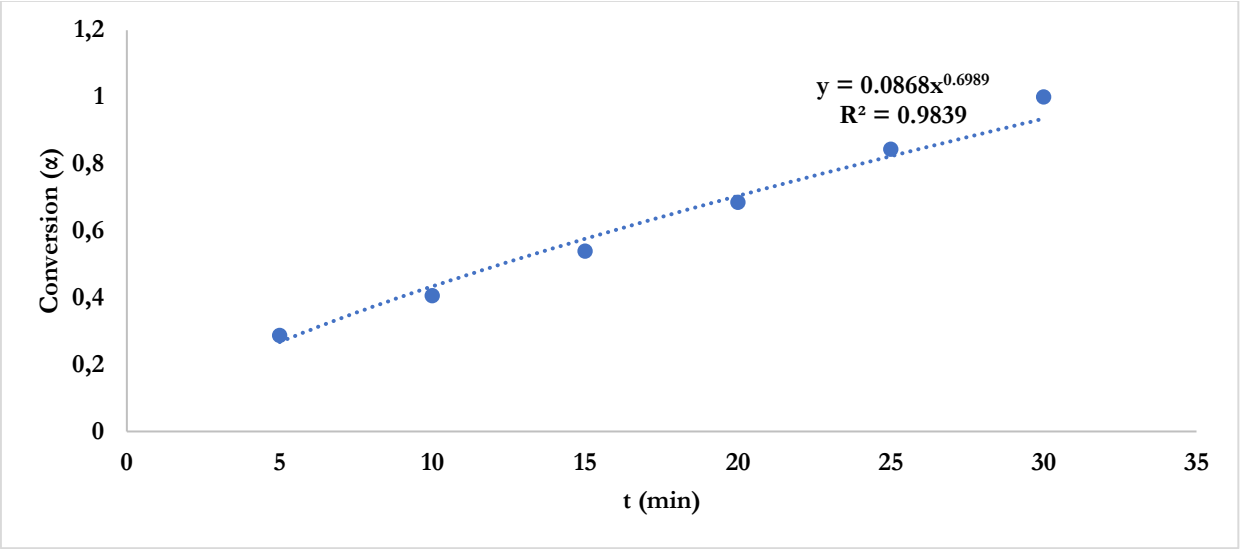


Figure 4: Conversion Fraction and Time During the Thermal Decomposition of CSS at 160°C

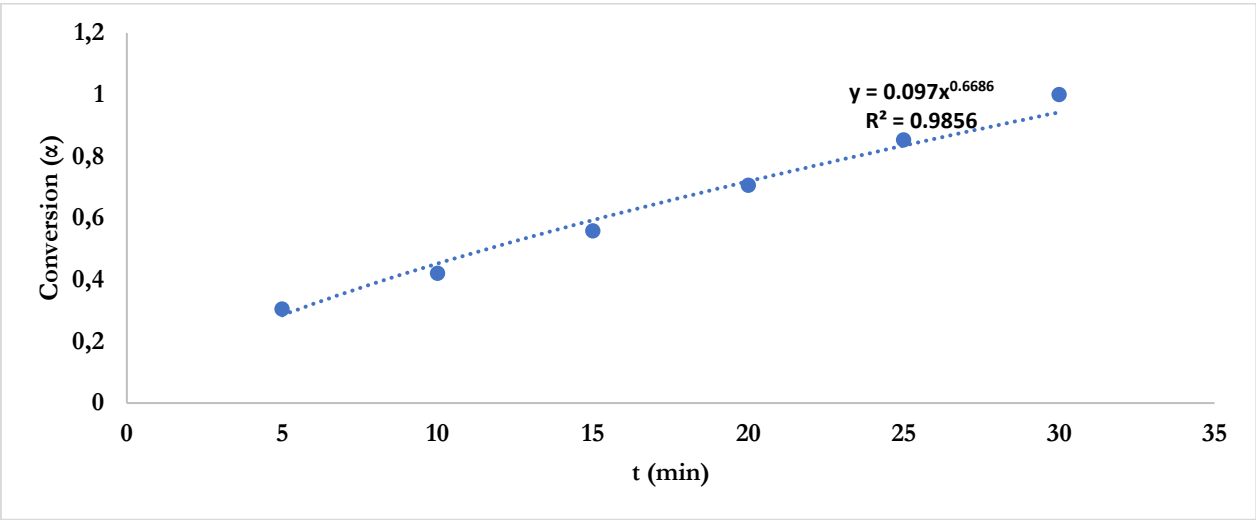


Figure 5: Conversion Fraction and Time During the Thermal Decomposition of CSS at 180°C

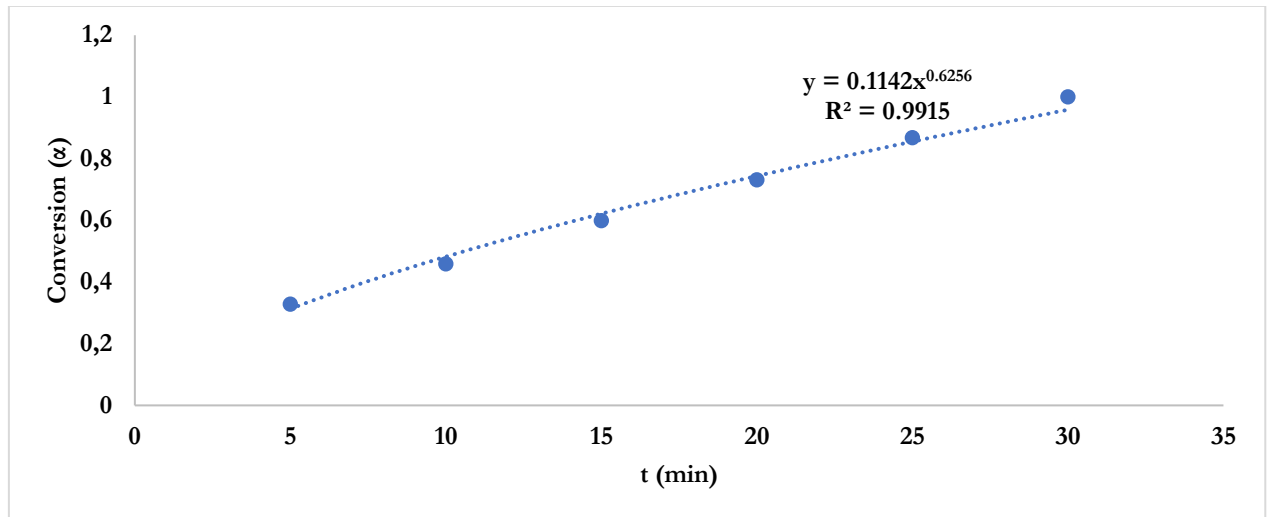


Figure 6: Conversion Fraction and Time During the Thermal Decomposition of CSS at 200°C

Table 5: Kinetics parameters for thermal decomposition of CSS using Empirical Model

Temperature (°C)	Kinetic Mechanism	Rate Equation	R ²
100	Volume Contraction	$0.03947(1-\alpha)^{0.33}$	0.9900
120	Volume Contraction	$0.03114(1-\alpha)^{0.28}$	0.9905
140	Volume Contraction	$0.03795(1-\alpha)^{0.35}$	0.9804
160	Volume Contraction	$0.03785(1-\alpha)^{0.32}$	0.9839
180	Volume Contraction	$0.03901(1-\alpha)^{0.35}$	0.9856
200	Volume Contraction	$0.04136(1-\alpha)^{0.397}$	0.9915

The kinetic parameters for the thermal decomposition of Coffee Senna Seeds (CSS) at different roasting temperatures, as presented in Table 5, reveal that the decomposition process predominantly follows a volume contraction mechanism across all temperatures. The high R^2 values (0.9804–0.9915) indicate excellent conformity of the experimental data with the empirical model, confirming the reliability of the derived rate equations. The reaction order (n) values ranged from 0.28 to 0.397, suggesting a diffusion-limited degradation process.

These findings align with previous studies that reported volume contraction as a common kinetic pathway in the thermal degradation of lignocellulosic and seed-based biomaterials (Kebede *et al.*, 2023; Natarajan *et al.*, 2022). Similar results were observed in the decomposition kinetics of Moringa seeds and other plant-based residues, where the contracting geometry model best described the thermal behavior (Singh & Das, 2021).

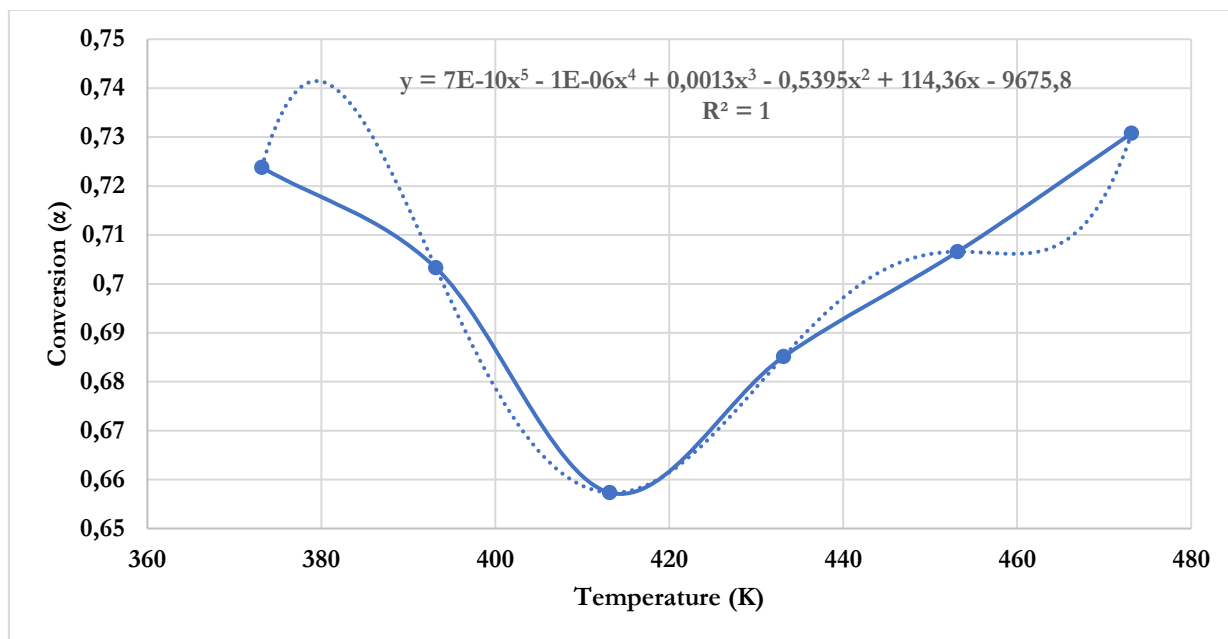


Figure 7: Plot of Conversion Fraction and Temperature for the CSS Phytochemicals

Figure 7 illustrates the behavior of the conversion factor (α) across a thermal processing parameter (likely temperature or time), revealing a distinct U-shaped trend: α initially decreases, reaching a minimum near 400K, and subsequently increases. This pattern suggests an initial degradation or transformation of phytochemicals, followed by the formation or reorganization of thermally stable compounds as temperature or roasting duration increases. The fifth-degree polynomial regression model fitted to the experimental data with an R^2 value of 1 indicates an excellent agreement, implying that the observed trend is highly representative of the experimental behavior. Such regression approaches have been similarly applied in previous studies to model complex thermal transformations of plant-based bio-resources, where high-order polynomials effectively captured non-linear behavior of compound conversion and degradation (Natarajan *et al.*, 2022; Kebede *et al.*, 2023). These findings further align with work by Singh and Das (2021), who noted comparable degradation-reformation dynamics in the thermal treatment of Moringa seeds and other lignocellulosic materials.

Thermodynamics Parameters for Roasting of CSS

Thermodynamic parameters for the roasting of Coffee Senna Seeds (CSS) provide critical insight into the energy requirements and spontaneity of the thermal decomposition process. Key indicators such as enthalpy (ΔH), Gibbs free energy (ΔG), and entropy (ΔS) help assess the nature of the reaction whether it is endothermic or exothermic, ordered or

disordered, and whether it proceeds spontaneously under specific conditions. These parameters reflect the molecular rearrangements and stability of phytochemicals during heat treatment (Mohammed *et al.*, 2021). Table 8 present the thermodynamic parameters for thermal decomposition of CSS.

Table 8: Thermodynamics parameters for thermal decomposition of CSS

T (K)	ΔH (kJ/mol)	ΔG (kJ/mol)	ΔS (kJ/K)	Ea (kJ/mol)
373.15	1585.9009	102920.541	-271.56543	1589.004
393.15	1419.6209	108356.228	-271.57657	1422.891
413.15	1253.3409	113800.378	-271.60711	1256.777
433.15	1087.0609	119252.580	-271.65342	1090.664
453.15	920.7809	124712.462	-271.71259	924.551
473.15	754.5009	130179.686	-271.78228	758.438

The thermodynamic parameters derived for the thermal decomposition of Coffee Senna Seeds (CSS), as shown in Table 8, reveal crucial insights into the energetic and feasibility of the degradation process. The enthalpy change (ΔH) values, ranging from 1585.90 to 754.50 kJ/mol, decrease with increasing temperature, indicating that the decomposition process becomes energetically more favorable at higher temperatures. This trend is consistent with the behavior of other biomass materials undergoing thermal decomposition (Kebede *et al.*, 2023).

The consistently high and positive Gibbs free energy (ΔG) values, increasing from 102.92 to 130.18 kJ/mol, suggest that the decomposition process is non-spontaneous across the studied temperature range. This implies that an external energy source (roasting) is necessary to drive the reaction forward. A similar trend was reported in the thermal degradation of *Moringa oleifera* and other lignocellulosic biomaterials, where high ΔG values indicated limited spontaneity (Natarajan *et al.*, 2022).

Furthermore, the negative entropy values (ΔS), approximately -271.5 kJ/K, imply a decrease in disorder during the transition state of the decomposition reaction. This may be attributed to the rearrangement of biomass components into more ordered char structures, a common phenomenon in thermolysis processes (Singh & Das, 2021). The calculated activation energies for *Senna occidentalis* seeds, ranging from 1589 to 758 kJ/mol, exhibit a decreasing trend with increasing temperature. This behavior is consistent with previous studies, which report that the thermal degradation of plant-derived bioactive compounds is

often characterized by a reduction in activation energy as temperature rises (Eke *et al.*, 2020; Singh *et al.*, 2018). Overall, these thermodynamic results suggest that the thermal decomposition of CSS is an endothermic, non-spontaneous process governed by decreased randomness in the transition state findings that align with similar studies on plant-derived biomass.

CONCLUSION

The kinetic modeling and thermodynamic analysis of roasted Coffee Senna (*Senna occidentalis*) seeds provided valuable insights into the thermal degradation behavior of the seeds during roasting. Experimental data obtained across a temperature range of 100 °C to 200 °C and roasting times between 5 and 30 minutes showed a consistent mass reduction from 98.4 g to 70.0 g, indicating progressive degradation with increased thermal exposure.

Spectroscopic analyses using FTIR and UV-Vis confirmed the presence and quantifiable concentrations of bioactive phytochemicals in the roasted seeds. These findings affirm the potential of Coffee Senna seeds as a source of bioactive compounds of medicinal relevance.

Kinetic modeling revealed that the degradation process followed a volume contraction mechanism across all roasting temperatures. The models yielded high coefficients of determination ($R^2 = 0.9804\text{--}0.9915$), indicating excellent fit. Additionally, the low reaction orders (0.28–0.397) pointed to a diffusion-controlled process governing the thermal decomposition.

Thermodynamic evaluation further revealed that the roasting process is endothermic and non-spontaneous. The enthalpy change (ΔH) ranged from 754.50 to 1585.90 kJ/mol, while Gibbs free energy (ΔG) varied between 102.92 and 130.18 kJ/mol. The negative entropy change ($\Delta S \approx -271.5$ kJ/K) across all roasting conditions suggested a transition to a more ordered state during the degradation process. Additionally, the calculated activation energies for *Senna occidentalis* seeds, ranging from 1589 to 758 kJ/mol, exhibit a decreasing trend with increasing temperature. Collectively, these findings provided comprehensive understanding of the thermal behavior and stability of Coffee Senna seeds under roasting conditions for the kinetics and thermodynamics.

REFERENCES

- Abioye, A. M., Adebayo, E. A., & Ayepola, O. O. (2021). Optimization of thermal processing for detoxification and preservation of bioactive compounds in legumes. *Journal of Food Processing and Preservation*, 45(1), e15067. <https://doi.org/10.1111/jfpp.15067>
- Adebayo-Tayo, B. C., Isaac, F. O., & Odeniyi, M. A. (2009). Microbial quality, proximate composition and aflatoxin content of some processed traditional condiments from Nigeria. *African Journal of Food Science*, 3(2), 61–67.
- Adegbite, S. A., Akinpelu, D. A., & Oladele, O. O. (2022). Phytochemical and antimicrobial properties of *Senna occidentalis* seeds. *Journal of Medicinal Plants Research*, 16(4), 123–130. <https://doi.org/10.5897/JMPR2022.7162>
- Adegbite, A. A., Ogunlade, C. A., & Afolabi, I. S. (2020). Thermal stability and antioxidant activity of saponin-rich extracts from selected legumes. *Journal of Food Biochemistry*, 44(8), e13301. <https://doi.org/10.1111/jfbc.13301>.
- Adeyemi, O. S., Akanji, M. A., & Bello, A. S. (2022). Thermal-induced changes in phytochemical and functional group composition of medicinal plant seeds: An FTIR-based study. *Journal of Food Biochemistry*, 46(2), e13988. <https://doi.org/10.1111/jfbc.13988>
- Ajiboye, B. O., Yusuf, M. O., & Oloyede, H. O. B. (2021). Effect of roasting on the phytochemical composition and detoxification of *Senna occidentalis* seeds. *Journal of Food Biochemistry*, 45(5), e13675. <https://doi.org/10.1111/jfbc.13675>
- Akinmoladun, F. O., Akinrinlola, B. L., Komolafe, T. O., & Farombi, E. O. (2020). Phytochemical constituents and antioxidant activities of *Senna occidentalis* (L.) leaves. *Journal of Pharmacognosy and Phytochemistry*, 9(4), 1164–1170. <https://www.phytojournal.com/archives/2020/vol9issue4/PartQ/9-4-170-832.pdf>
- Akinyemi, A. A., Oluwafemi, S. A., & Ibrahim, H. (2021). Detoxification of antinutritional factors in legume seeds using thermal methods. *African Journal of Food Science*, 15(3), 71–79. <https://doi.org/10.5897/AJFS2020.2023>
- Akubor, P. I., & Ogu, G. I. (2018). Effect of thermal processing on anti-nutritional factors and nutrient composition of African yam bean seed flour. *Food Science & Nutrition*, 6(3), 753–758. <https://doi.org/10.1002/fsn3.611>
- Ayeni, A. O., & Yakubu, M. T. (2020). *Ethnobotanical, phytochemical and pharmacological review of Senna occidentalis*. *Heliyon*, 6(11), e05534. <https://doi.org/10.1016/j.heliyon.2020.e05534>
- Bridgwater, A. V. (2012). Review of fast pyrolysis of biomass and product upgrading. *Biomass and Bioenergy*, 38, 68–94. <https://doi.org/10.1016/j.biombioe.2011.01.048>
- Budarin, V. L., Clark, J. H., Lanigan, B. A., Shuttleworth, P. S., & Farmer, T. J. (2011). Thermal analysis of biomass components during pyrolysis. *Bioresource Technology*, 102(3), 1986–1993. <https://doi.org/10.1016/j.biortech.2010.09.090>
- Doyle, C. D. (1961). Estimating thermal stability of experimental polymers by thermogravimetric analysis. *Analytical Chemistry*, 33(1), 77–79. <https://doi.org/10.1021/ac60168a005>
- Eke, C. C., Ogbonna, J. C., & Okechukwu, D. O. (2020). Kinetics and thermodynamics of the thermal degradation of bioactive compounds from plant materials: A review.

- Journal of Thermal Analysis and Calorimetry*, 142, 1593–1605.
<https://doi.org/10.1007/s10973-020-09771-2>
- Eze, V. C., & Obi, F. O. (2023). UV-visible spectroscopic characterization of bioactive compounds in plant seed extracts. *International Journal of Biochemistry Research & Review*, 32(5), 1–9.
- Ezeonu, C. S., Ejikeme, C. M., Onwurah, I. N. E., & Eze, S. O. O. (2022). Nutraceutical potentials of some underutilized legumes: Focus on *Senna occidentalis*. *African Journal of Food Science*, 16(5), 125–134. <https://doi.org/10.5897/AJFS2021.2134>
- Fayemiwo, O. M., Agarry, S. E., & Ogunleye, O. O. (2021). Thermal processing and chemical profile transformation of Nigerian medicinal plants: An FTIR spectroscopic study. *Journal of Applied Research on Medicinal and Aromatic Plants*, 23, 100309. <https://doi.org/10.1016/j.jarmap.2021.100309>
- Ferdous, J., Mahmud, K., Akter, A., & Yeasmin, M. (2020). Kinetic and thermodynamic modeling of biomass pyrolysis. *Renewable and Sustainable Energy Reviews*, 134, 110288. <https://doi.org/10.1016/j.rser.2020.110288>.
- Gaur, V. K., Sharma, P., Sirohi, R., et al. (2022). Process optimization, kinetic, and thermodynamic modeling of thermal degradation in biomass seeds. *Bioresource Technology Reports*, 17, 100924. <https://doi.org/10.1016/j.biteb.2021.100924>
- Isah, A. G., Ndukwe, G. I., & Abdullahi, M. I. (2022). FTIR and GC-MS profiling of bioactive compounds in processed seeds of *Senna occidentalis*. *Journal of Applied Chemistry*, 14(1), 34–41.
- Jindal, A., Garg, A., & Gautam, Y. (2021). Thermogravimetric analysis and kinetic modeling of *Prosopis juliflora*: A potential biomass feedstock. *Energy Sources, Part A: Recovery, Utilization, and Environmental Effects*, 43(8), 993–1004.
- Kaisar, M. A., Rahman, M. S., Rahman, M. S., & Hasan, C. M. (2018). Phytochemical and pharmacological investigations of *Senna occidentalis*. *Journal of Ethnopharmacology*, 222, 1–17. <https://doi.org/10.1016/j.jep.2018.04.005>
- Kebede, M. A., Zhang, Z., & Liu, Y. (2023). Kinetic modeling and thermogravimetric analysis of thermal decomposition behavior of agricultural biomass. *Renewable Energy*, 209, 1161–1171. <https://doi.org/10.1016/j.renene.2023.03.042>
- Khan, M. A., Kiran, S., Shahid, M., & Shaheen, S. (2015). *Distribution, phytochemistry, and pharmacological properties of Senna occidentalis: A review*. *International Journal of Pharmacognosy and Phytochemical Research*, 7(3), 613–620.
- Khawam, A., & Flanagan, D. R. (2006). Solid-state kinetic models: Basics and mathematical fundamentals. *The Journal of Physical Chemistry B*, 110(35), 17315–17328. <https://doi.org/10.1021/jp062746a>
- Kumar, R., Mehta, S., & Singh, A. (2023). "Thermal Processing Effects on Anti-Nutritional Factors and Nutrient Profiles in Edible Legumes: A Comprehensive Study." *Food Bioscience*, 50, 102190. <https://doi.org/10.1016/j.fbio.2023.102190>
- Kumar, R., Mehta, S., & Singh, A. (2023). "Thermal Processing Effects on Anti-Nutritional Factors and Nutrient Profiles in Edible Legumes: A Comprehensive Study." *Food Bioscience*, 50, 102190. <https://doi.org/10.1016/j.fbio.2023.102190>
- Mohammed, A. I., Yusuf, A. A., & Abubakar, M. S. (2021). Thermodynamic and kinetic modeling of thermal degradation of medicinal plant residues. *Journal of Thermal*

- Analysis and Calorimetry*, 145(6), 2101–2112. <https://doi.org/10.1007/s10973-020-10175-6>
- Murthy, P. S., & Naidu, M. M. (2021). Influence of roasting on the bioactive composition and antioxidant properties of plant-based seeds. *Journal of Functional Foods*, 79, 104395. <https://doi.org/10.1016/j.jff.2021.104395>.
- Natarajan, E., Arul Mozhi Selvan, V., & Ilangovan, V. (2022). Thermogravimetric analysis and kinetic study on the pyrolysis of tropical biomass. *Bioresource Technology Reports*, 20, 101239. <https://doi.org/10.1016/j.biteb.2022.101239>
- Nwokocha, C. R., Eze, M. O., & Okoro, E. U. (2022). Thermal degradation and phytochemical retention in roasted medicinal plant seeds. *Journal of Applied Research on Medicinal and Aromatic Plants*, 30, 100436. <https://doi.org/10.1016/j.jarmap.2022.100436>.
- Obasi, H. C., Okoye, F. B. C., & Onuoha, S. C. (2022). Influence of thermal processing on phytochemicals and antioxidant properties of African walnut (*Tetracarpidium conophorum*). *Food Research*, 6(4), 27–35.
- Okoye, M. O., Arinze, E. A., & Ezeokonkwo, M. A. (2018). Thermal degradation of anti-nutritional factors in leguminous seeds: Influence of roasting temperature and time. *Nigerian Food Journal*, 36(1), 84–91. <https://doi.org/10.1016/j.nifo.2018.03.008>
- Olalekan, R. M., & Uchenna, A. D. (2021). Effects of roasting on phytochemical composition and antioxidant capacity of *Moringa oleifera* seed extracts. *Journal of Medicinal Plants Research*, 15(3), 115–123.
- Olaniran, A. F., Olayanju, T. M. A., & Afolabi, I. S. (2020). Influence of thermal processing on bioactive and antioxidant characteristics of some African seeds. *Journal of Food Science and Technology*, 57(9), 3334–3342.
- Omoregie, E. S., & Osagie, A. U. (2011). Phytochemical screening and anti-anaemic effect of *Senna occidentalis* leaf extract in rabbits. *Pakistan Journal of Nutrition*, 10(10), 940–946. <https://doi.org/10.3923/pjn.2011.940.946>
- Onwordi, C. T., Ogungbade, A. M., & Wusu, A. D. (2015). Changes in the proximate and phytochemical composition of *Cassia occidentalis* seeds during processing. *African Journal of Food, Agriculture, Nutrition and Development*, 15(2), 9919–9932. <https://doi.org/10.18697/ajfand.70.14635>.
- Osabor, V. N., Etim, E. E., & Ntinya, S. O. (2020). Evaluation of phytochemicals and FTIR analysis of roasted and unroasted seeds of *Parkia biglobosa*. *African Journal of Food Science*, 14(4), 103–110. <https://doi.org/10.5897/AJFS2020.1882>.
- Ozawa, T. (1992). A new method of analyzing thermogravimetric data. *Bulletin of the Chemical Society of Japan*, 38(11), 1881–1886.
- Ragazzi, E., & Veronese, G. (2021). Quantitative analysis of phenolic compounds using UV-Vis spectrophotometry. *Journal of Pharmaceutical and Biomedical Analysis*, 203, 114168. <https://doi.org/10.1016/j.jpba.2021.114168>
- Rehman, A. U., Mahmud, A., & Ahmad, M. (2020). Effect of roasting on chemical composition and antioxidant activity of selected legumes. *Food Science & Nutrition*, 8(6), 2901–2907. <https://doi.org/10.1002/fsn3.1534>

- Ribeiro, J. P., Cabral, M. F., & Cobo, M. F. (2015). Thermogravimetric and kinetic analysis of coconut husk, sugarcane bagasse and elephant grass. *Chemical Engineering Transactions*, 43, 505–510. <https://doi.org/10.3303/CET1543085>
- Rohman, A., & Windarsih, A. (2020). The use of FTIR spectroscopy in combination with chemometrics for analysis of bioactive compounds in medicinal plants. *Applied Spectroscopy Reviews*, 55(4), 512–536. <https://doi.org/10.1080/05704928.2019.1656260>
- Satish, K., Prasad, S., & Babu, N. R. (2023). Therapeutic and toxicological aspects of *Senna occidentalis*: A comprehensive review. *Biomedicine & Pharmacotherapy*, 161, 114212. <https://doi.org/10.1016/j.biopha.2023.114212>
- Shen, D., Gu, S., & Bridgwater, A. V. (2009). Study on the pyrolytic behavior of xylan-based hemicellulose using TG–FTIR and Py–GC–FID/MS. *Journal of Analytical and Applied Pyrolysis*, 85(1-2), 1–7.
- Šimkovic, I., & Šajgalík, P. (2021). Thermal decomposition kinetics of lignocellulosic biomass: Modeling and mechanism analysis. *Renewable Energy*, 173, 974–984. <https://doi.org/10.1016/j.renene.2021.04.085>
- Singh, R. P., Chidambaram, P. K., & Sharma, B. R. (2018). Thermal degradation kinetics and thermodynamic parameters of medicinal plant-based bioactive compounds. *Bioresource Technology Reports*, 3, 153–160. <https://doi.org/10.1016/j.biteb.2018.07.005>
- Singh, A., Kumar, D., & Sharma, P. (2021). Application of kinetic models for pyrolysis of various seeds for bioenergy. *Biomass Conversion and Biorefinery*, 11, 2023–2035. <https://doi.org/10.1007/s13399-021-01462-7>
- Singh, R., Singh, S., & Yadav, R. (2020). Phytochemical screening and pharmacological properties of *Senna occidentalis*: A review. *Journal of Pharmacognosy and Phytochemistry*, 9(3), 1785–1790.
- Son, Y., Kim, J., Lee, C. H., & Kim, S. (2014). Pyrolysis kinetics and thermal behavior of lignocellulosic biomass. *Renewable Energy*, 65, 71–77. <https://doi.org/10.1016/j.renene.2013.08.019>
- Vyazovkin, S., & Wight, C. A. (1999). Model-free and model-fitting approaches to kinetic analysis of isothermal and nonisothermal data. *Thermochimica Acta*, 340–341, 53–68. [https://doi.org/10.1016/S0040-6031\(99\)00253-1](https://doi.org/10.1016/S0040-6031(99)00253-1)
- Vyazovkin, S., Burnham, A. K., Criado, J. M., Pérez-Maqueda, L. A., Popescu, C., & Sbirrazzuoli, N. (2011). ICTAC Kinetics Committee recommendations for performing kinetic computations on thermal analysis data. *Thermochimica Acta*, 520(1-2), 1–19. <https://doi.org/10.1016/j.tca.2011.03.034>
- Vyazovkin, S., Wight, C., & Koga, N. (2020). Advances in thermal decomposition kinetics: Model-free methods and beyond. *Thermochimica Acta*, 679, 178344. <https://doi.org/10.1016/j.tca.2019.178344>
- Zhang, J., Zhang, X., & Song, X. (2020). Fourier-transform infrared spectroscopy analysis of roasted seeds for functional group identification. *Spectrochimica Acta Part A: Molecular and Biomolecular Spectroscopy*, 236, 118356. <https://doi.org/10.1016/j.saa.2020.118356>



Research article

Pyrolysis of metal oxides treated *Canarium schweinfurthii* Shell: Investigation of thermogravimetric kinetics and thermodynamics

Kabir Garba^{a,*}, Habu Iyodo Mohammed^{a,b}, Yusuf Makarfi Isa^c

^a Department of Chemical Engineering, Abubakar Tafawa Balewa University, P.M.B 0248, Bauchi, Nigeria

^b Department of Chemical Engineering, University of Maiduguri, P.M.B 1069, Maiduguri, Nigeria

^c School of Chemical and Metallurgical Engineering, University of the Witwatersrand, 1 Jan Smuts Avenue, Braamfontein, 2000, Johannesburg, South Africa

ARTICLE INFO

Keywords:

Biomass

Canarium schweinfurthii fruit shell

Metal oxides

Kinetic

Pyrolysis

Thermogravimetric

ABSTRACT

Metal oxides as catalysts alter the properties of the pyrolysis vapor secondary reactions during the thermal decomposition of several biomass leading to high-value bio-oils. This study aimed to investigate the thermal decomposition characteristics of *Canarium Schweinfurthii* (CS) shells that were treated with various metal oxides (ZnO, CuO, Fe₂O₃/FeO, and Fe₂O₃) using pyrolysis. The study also sought to identify pyrolysis reaction parameters (kinetics and thermodynamics parameters) that are not widely documented. Thermogravimetric pyrolysis was carried out at different heating rates, and the undocumented pyrolysis kinetic parameters were determined using the Flynn-Wall Ozawa method (FWO) according to American Standard Testing and Materials (ASTM) 6441 guidelines for assessing biomass decomposition. The metal oxide-treated CS shells lost significant weight between 62 and 67 wt% during the thermogravimetric pyrolysis, lower than 75 wt% of the CS shell. The average activation energies (E_a) for pyrolysis of the ZnO, CuO, Fe₂O₃/FeO, and Fe₂O₃ treated CS shells were 203.04, 155.35, 338.85, and 219.92 kJ/mol, respectively in contrast to that of the untreated CS-shell. The Bayesian Information Criteria revealed that the diffusion kinetics of the Gistling-Brounshtein model best describes the pyrolysis of the shell mixed with metal oxides. The metal oxides affected the CS shells' pyrolysis kinetic parameter (E_a), which can promote pyrolysis vapor upgrading to encourage the widespread use of metal oxides in pyrolysis for bioenergy and chemical recovery.

1. Introduction

The increased need to harness the limited biomass available to produce value-added biofuel and chemicals demands the search for catalysts and technology that lower energy consumption, improve yields, and use high-value components.

Catalysts in situ with biomass not only direct pyrolysis vapor to high-value pyrolytic oil but also affect activation energy (E_a) and thermodynamic parameters for pyrolysis system operations [1]. Thermodynamics and kinetics of thermal decomposition of several biomasses have been investigated [2,3], such as Hyphaene Thebaica shell [3], Pongamia pinnata [4], palm kernel shell [5], Typha latifolia [6], *chlorella vulgaris* [7] and *Canarium Schweinfurthii* hard shell [8].

The effect of catalysts on the thermal decomposition of species of biomass has been previously reported in the literature [9,10].

* Corresponding author.

E-mail addresses: gkabir@atbu.edu.ng, kbgarba.1214@gmail.com (K. Garba).

Effects of MgO, CaO, and ZnO on the activation energy of pyrolysis of Empty Palm Fruit Bunch (EPFB) were investigated by Yee et al. [11]. These oxides lowered the E_a of EPFB, where the most significant decrease was from 274.5 to 194.8 kJ/mol by treating the EPFB with MgO (10 wt%). A separate study reported that catalytic pyrolysis of rice hull with calcium oxide derived from eggshell and limestone reduced the values of E_a [12]. Yang et al. [13] studied the catalytic effects of Ni–CaO–Ca₂SiO₃ and Ni–Ca₂SiO₃ on the pyrolysis of pine wood sawdust. A decrease in E_a , biomass pyrolysis produces H₂ and CO from the breakage of light organic molecules was observed. Wibowo et al. [9] investigated the effects of rice husk ash as catalysts in catalytic pyrolysis of rice husk. The E_a decreased with ash addition ratios. The addition of the catalyst slowed the decomposition of hemicellulose but accelerated the decomposition of cellulose and lignin. The *Canarium schweinfurthii* hard shell was studied for its thermochemical conversion to high-grade bioenergy precursors, in which the bio-oil derived by thermal pyrolysis yields complex phenolics and oxygenates [8]. The effects of catalysts on their thermos-kinetic behaviors were lacking.

There are several approaches to evaluating E_a and pre-exponential factors, which include Coats-Redfern, Flynn Wall Ozawa (FWO), Kissinger-Akshira-Sunose (KAS), and Starink methods [3,14]. Mohammed et al. [3] compared the FWO, KAS, and Starink methods to evaluate the kinetics and thermodynamics parameters of the thermogravimetric pyrolysis of the *hyphaene thebaica* shell. The FWO method best describes the process as the kinetic parameters obtained are accurate. Furthermore, Chee et al. [15], observed that the kinetic parameters determined using FWO, KAS, and Distributed Activation Energy Model (DEAM) for catalytic and co-pyrolysis of palm kernel shells and plastic wastes are consistent with the literature. Also, Gan et al. [12] found FWO more reliable than DEAM in determining kinetic parameters for catalytic pyrolysis of rice husk over limestone and eggshell catalysts. In addition, FWO is the method adopted by American Standard Testing and Materials (ASTM) 1641 for accurately examining biomass thermal decomposition properties. However, other numerical approaches, such as Artificial Neural Networks (ANN) are being investigated [7,12].

The catalytic pyrolysis of the CS shell might lead to the release of vapor, resulting in a high-value pyrolytic oil rich in phenol, aromatic acids, esters, and hydrocarbons. The challenge lies in identifying appropriate catalysts that lower energy consumption and direct the pyrolysis reaction mechanisms to favor selectivity toward value-added compounds. The activities of transition metals, such as nickel and iron oxide, in upgrading the pyrolysis vapor of some biomass species were investigated, and reported in the literature [16], nickel and iron oxide promote yields of monoaromatic hydrocarbons. Catalytic upgrading of pyrolysis oil derived from sawdust by natural gas at atmospheric pressure over Zn, Fe, Co, Cu, Ni, Mn, Zr, and Ce supported on ZSM-5 was investigated, Zn gives the highest oil yield, with a high oil H/C atomic ratio and a low oil O/C atomic ratio [17]. A study by Lugovoy et al. [18] reported that a composite of ZSM-5-bentonite and 2 % cobalt resulted in a high yield of gas rich in methane. Catalytic pyrolysis of cellulose using Zn/ZSM-5 and FePO₄/ZSM-5 caused the production of furan compounds and levoglucosan [19]. The current trend suggests cheaper resources as catalyst feedstock for bioenergy production through the thermochemical conversion of biomass [20]. Iron ore dust (IOD) from an iron ore milling site is a cheap source of iron oxides that can serve as a catalyst in catalytic pyrolysis processes for this study.

The *Canarium Schweinfurthii* (CS) nut is mass-produced and has a shell (CS-shell) enclosing its kernel that causes waste management concerns. This study aims to explore the thermogravimetric pyrolysis of the CS-shell with metal oxides (Fe₂O₃, ZnO, CuO, and mixed Fe₂O₃/FeO obtained from the decomposition of magnetite). The CS shells' pyrolysis properties with the selected metal oxides are yet to be documented. Therefore, it is crucial to perform a comprehensive investigation through the thermogravimetric pyrolysis of the CS-shell with the metal oxides. The metal oxides' catalytic activities can be predicted from kinetics and thermodynamic parameters obtained from thermogravimetric pyrolysis. The study explores various metal oxides to identify appropriate catalysts that lower energy consumption and direct the pyrolysis reaction mechanisms to favor selectivity towards value-added compounds.

2. Materials and methods

2.1. Materials, CS-shell preparation, and thermogravimetric pyrolysis

The *Canarium schweinfurthii* fruit shell was obtained from Plateau State, Nigeria. The reagent-grade Copper sulfate pentahydrate (CuSO₄·5H₂O), Zinc nitrate hexahydrate (Zn(NO₃)₂·6H₂O), and Iron sulfate heptahydrate (FeSO₄·7H₂O) salts were supplied by Sigma-Aldrich through a local chemical vendor in Lagos, Nigeria. Iron ore dust (IOD) rich with 84 wt% magnetite (Fe₃O₄) was collected from a mining site in Bauchi, Nigeria. An X-ray fluorescence spectrometer (Rigaku RIX 3000) with X-ray fluorescence (XRF) was used to reveal the composition of the raw and calcined IOD, as shown in Table 1. A chemical reagent vendor supplied N₂ (99.99 %) as a

Table 1
XRF compositions of Iron ore dust.

Compounds	Raw (wt.%, dry basis)	Calcined @ 900 °C	Literature [21]
SiO ₂	7.99	6.45	9.5
Al ₂ O ₃	4.04	5.58	1.71
Fe ₃ O ₄	83.58	–	37.5
Fe ₂ O ₃	–	43.42	34.0
FeO	–	40.83	–
CaO	1.60	1.40	8.5
MgO	2.79	2.32	0.85
Others	0.00	0.00	7.94
Total	100	100	100

sweeping gas in thermogravimetric pyrolysis investigations.

2.2. Methods

2.2.1. Characterization and preparation of *Canarium schweinfurthii* shell

This study employed the same *Canarium schweinfurthii* shell sample as in a previous study [8] for thermogravimetric pyrolysis studies on Shimadzu TGA 50. The CS-shell's proximate and ultimate analyses were performed on a thermogravimetric analyzer (PerkinElmer STA 6000) and a CHNO/S analyzer (PerkinElmer 400 Series II), respectively. The high heating value (HHV) was determined on an IKA C 200 bomb calorimeter.

At an equivalent weight of 10 wt%, the IOD and CS-Shell powder were monodispersed, while the hydrated metal salts were doped onto the CS-Shell. The thermogravimetric pyrolysis was performed at 10, 15, and 20 °C/min heating rates on the treated CS shells. The kinetic and thermodynamic parameters were determined using weight loss data. During the pyrolysis, the IOD, mostly 83.58 wt% magnetite (Fe₃O₄) decomposed into mixed iron oxide (Fe₂O₃/FeO). However, the doped metal salts decomposed into their respective metal oxides, ZnO, CuO, and Fe₂O₃ (according to the reactions in Eqs. (1)–(4)), and eventually, they were grafted onto the CS shells.



The treatment of biomass with metal oxides considerably improves pyrolytic processes. The CS-metal oxides have a significant synergistic influence on pyrolysis reactions. The resultant metal oxides promoted secondary reactions on the organic volatiles produced by the pyrolysis degradation of the CS-shells' lignin and cellulose macrostructures. The metal oxide-treated CS shells were labeled as follows: CS-ZnO, CS-Fe₂O₃, CS-CuO, and CS-Fe₂O₃/FeO.

2.2.2. Decomposition kinetic models of biomass

The FWO correlation equation (Eq. 5) was used to determine the kinetic parameters. The stoichiometry and kinetics model for isothermal devolatilization of biomass presented as Eqs. (6) and (3) respectively, was previously reported by Wang et al. [22].

$$g(\alpha) = \frac{A}{\beta} 0.00484 \exp\left(-1.052 \frac{E_a}{RT}\right) \quad (5)$$

Subsequently, taking the natural log of both sides resulted in Eq. (5).

$$\ln(\beta) = \ln \frac{AE_a}{Rg(\alpha)} - 5.331 - 1.052 \frac{E_a}{RT} \quad (6)$$

Where α is the extent of conversion, E_a is the activation energy and A is the pre-exponential factor. The plots of $\ln(\beta)$ against $\frac{1}{T}$ gives straight line from which activation energy, E_a is obtained and pre-exponential evaluated using solid-state reaction models. The solid-state reaction models are presented in Table 2. The best-fit model was identified using Bayesian Information Criteria (BIC). The Bayesian information criterion (BIC) (also known as the Schwarz criterion) is another statistical measure for comparative evaluation among models [23].

The BIC is determined using Eq. (7).

Table 2
Solid state reaction models from the Coat-Redfern method [3].

Mechanisms	Models $g(\alpha)$
Reaction	
(R ₁) First Order	$-\ln(1-\alpha)$
(R ₂) Second Order	$(1-\alpha)^{-1} - 1$
(R ₃) Third Order	$[(1-\alpha)^{-2} - 1]/2$
Diffusion	
(D ₁) One-way Transport	α^2
(D ₂) Two-way Transport	$\alpha + (1-\alpha)\ln(1-\alpha)$
(D ₃) Three-way Transport	$1 - ((1-\alpha)1/3)^2$
(D ₄) Ginstling-Brounshtein Eq	$1 - 2\alpha/3 - (1-\alpha)^{2/3}$
Nucleation	
(A ₄) Avrami-Erofe'ev 4	$[-\ln(1-\alpha)]^{1/4}$
Contracting	
(C ₁) Area contracting	$1 - (1-\alpha)^{1/2}$
(C ₂) Volume contracting.	$1 - (1-\alpha)^{1/3}$

$$BIC = \frac{kLn(n)}{n} - \frac{2l}{n} \quad (7)$$

The relative likelihood of the tested models was computed using Eq. (8).

$$Relative\ Likelihood = \exp(BIC_{min} - BIC_i) \quad (8)$$

where BIC_{min} is the BIC of a model with minimum value?

BIC_i BIC of model i.

The thermodynamic parameters such as changes in enthalpy, Gibb's free energy, and entropy of the devolatilization reaction of HTS were evaluated using relationships from Eqs. (9)–(8) [2].

$$A = \frac{[\beta E \exp(E_a/RT_m)]}{RT_m^2} \quad (9)$$

$$\nabla H = E_a - RT_m \quad (10)$$

where ∇H is change in enthalpy, E_a , activation energy, R, gas constant, and T_m is peak temperature of the DTG curve for the decomposition of HTS by pyrolysis.

$$\nabla G = E_a + RT_m \ln\left(\frac{K_B T_m}{hA}\right) \quad (11)$$

$$\nabla S = \frac{\nabla H - \nabla G}{T_m} \quad (12)$$

Where ∇G is the change in Gibb's free energy for thermal decomposition of HTS, K_B , Boltzman constant = $1.381 \times 10^{-23} \text{ J/K}$, h , Planck's constant = $6.626 \times 10^{-34} \text{ Js}$.

3. Results and discussion

3.1. Thermogravimetric analysis of CS-shell and metal oxide-treated CS-shell

The proximal and ultimate compositions of the CS shell, including its heating value, and its pioneer devolatilization pattern have already been documented are presented in the previous study [8]. Table 3 presents the CS-shell characterization data.

The CS-shell and metal oxides-treated CS shell decompositions were then studied using thermogravimetric pyrolysis at heating rates of 10, 15, and 20C/min to assess the effect of the metal oxides on the thermo-kinetic parameters. Fig. 1 (a) and (b) show the weight loss and devolatilization rate characteristics of the CS-shell and metal oxide-treated CS shells, which describe the decomposition profiles of the samples.

The TG profiles of raw CS-shell and metal oxide-treated CS shells reveal the same pattern and discrete stages of degradation. Between 30 and 220 °C, the release of around 9 wt% lighter volatiles, such as water and extractives trapped in the structure of the biomass, occurred, corresponding to volatile extractives, and water [24]. The effect of the metal oxides as catalysts is less prominent in the drying zone, yet CS-CuO exhibits peculiar behavior. The weight loss is around 8 wt% when compared to other metal oxide-treated CS shells where the CuO decreased during the drying process.

Because of the degradation of the shell macrostructure, the second stage of decomposition was rapid, resulting in a weight loss of 42.67 wt%. The $\text{Fe}_2\text{O}_3/\text{FeO}$ -treated shell requires higher temperatures of 10 °C than the Fe_2O_3 -treated shell, while the remaining ZnO and CuO-treated shells fall in the middle. The weight loss at the third stage accounts for about 8 wt% of the total weight loss, with CS- $\text{Fe}_2\text{O}_3/\text{FeO}$ having the highest residual biochar of 38 wt% and raw CS-shell having the lowest of 25 wt%. Because of the presence of metal oxides which served as catalysts, the biochar may have a higher ash content.

Fig. 1b presents the DTG curves of the CS-shell and metal oxide-treated CS shells, which indicate the amount of vapor released per minute. The peaks between 40 and 220 °C represent dehydration. The CS-shell decomposition resulted in a maximum dehydration of 1.668 % wt./min, while that of the CS-ZnO is the least at 0.8131 % wt./min. The metal oxides suppressed the dehydration reaction, with ZnO being the most active. The peaks observed between 220 and 400 °C belong to the degradation of hemicelluloses, extractives,

Table 3

Physicochemical characteristics of CS shell.

Proximate analysis (dry basis)			Ultimate analysis (dry basis)		
Parameter (wt.%)	Value	<i>Hyphaene thebaica</i> shell [3],	Parameter (wt.%)	Value	<i>Hyphaene thebaica</i> shell [3],
Moisture	3.70	4.97	Carbon	51.99	42.50
Volatile matter (VM)	70.97	73.31	Hydrogen	6.00	5.50
Fixed carbon (FC)	22.37	11.96	Nitrogen	0.06	0.55
Ash content	2.96	8.75	Sulfur	0.27	1.17
HHV (MJ/kg)	18.18	21.07	Oxygen	41.68	50.30

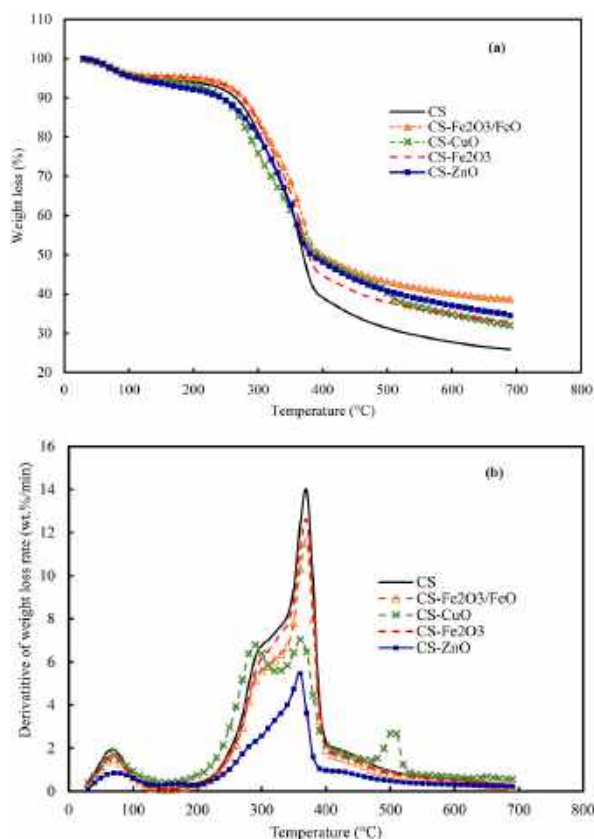


Fig. 1. Thermogravimetric curves (b) Differential thermogravimetric curves for pyrolysis of CS-Shell and metal oxide-treated CS shells.

and celluloses. ZnO suppressed devolatilization at all temperatures, with a maximum devolatilization rate of 5.461 wt%/min at 360 °C. The ZnO favors higher biochar yield suggesting an increase in aromatization of CS instead of cracking reactions [25], which involves the dehydration of methoxy and acetyl bond breakage of hemicellulose and cellulose [22] and subsequent polymerization to form a more rigid solid phase, called biochar. The ZnO-treated shell has a maximum devolatilization rate of 13.92 wt%/min at 370 °C.

Two distinctive peaks are observed in the DTG curve of the CS-Fe₂O₃ sample in the active pyrolysis zone. These differences indicate the catalytic effects of the metal oxides on the pyrolysis of CS-shell. At the final stage of the pyrolysis, the catalytic activities of Fe₂O₃ are more pronounced as more degradation of the residue occurs to liberate more vapor (2.67 % wt.%/min), which might contribute to the yield of vapor phase products. The Fe₂O₃ particle has a catalytic effect on the degradation of the char because of the breakdown of the residual molecular structure of the biochar. This shows that the Fe₂O₃ has better interaction with biomass, which enhances the catalytic degradation of the biomass compared to the Fe₂O₃/FeO. However, the increase in peak points indicates the complex, multi-step reactions of the catalytic reaction system [12].

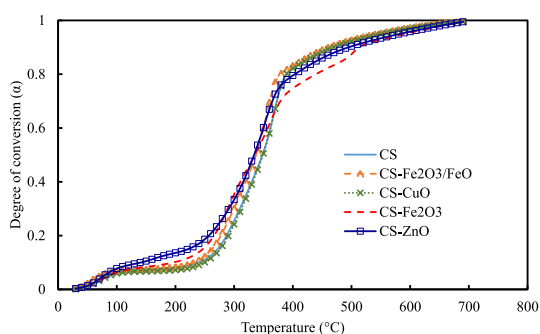


Fig. 2. Conversion, α vs temperature curve for pyrolysis of CS-Shell and metal oxide-treated CS shells.

3.2. Evaluation of the kinetics parameters of metal oxide-treated CS shells pyrolysis

The solid-state reaction mechanisms to describe pyrolysis reactions follow the criteria of the kinetics committee of the International Confederation for Thermal Analysis and Calorimetry (ICTAC), which suggested that the extent of conversion versus temperature curve be examined [26]. The curves for the CS-shell and metal oxide-treated CS shells under analysis are presented in Fig. 2. The curves resulted in a sigmoid shape, which rules out the use of power law models, which simulate accelerating and decelerating processes [25].

The kinetic characteristics of CS-shell and metal oxide-treated CS shells thermogravimetric data acquired at three different heating rates (10, 15, and 20°C/min) were analyzed and predicted. The plots of the thermogravimetric decomposition of CS, CS-Fe₂O₃/FeO, CS-Fe₂O₃, CS-CuO, and CS-ZnO in the active pyrolysis zone (220–400 °C) with conversion ranging from 0.1 to 0.9 at the three heating rates are shown in Fig. 3a–e. The plots are linear with a change in slope, from which the E_a was calculated at each degree of conversion. The R-square values of the plots are presented in Table 4.

Furthermore, mechanisms of the solid-state models (Table 2) that describe the pyrolysis reactions were determined using Bayesian information criteria (BIC). The effective mechanisms that govern the CS-shell and metal oxide-treated CS shell pyrolysis reactions are established through the FWO method using the BIC approach. The BIC gives reliable results because of its minimum error in the activation energy (E_a) and pre-exponential factor. Fig. 4 shows the reaction models and the accompanying relative probability generated using BIC. The Gistling-Brounstein diffusion (D4) has the lowest BIC values and a relative likelihood of one (1), which suggests the pyrolysis reaction follows the diffusion reaction pathways. The mechanisms of the C1 and C2 contraction and the D1, D2, and D3 diffusion have a significant combined effect on controlling the pyrolysis reactions. Therefore, the diffusion and contraction model mechanisms control the pyrolysis decomposition reaction for the CS-shell and metal oxide-treated CS-shell. Similarly, the pyrolysis decomposition of *Typha latifolia* obeys the mechanisms of contraction and diffusion [6].

Fig. 5 and Table 5 present the variation of E_a for pyrolysis of CS-shell and metal oxide-treated CS-shell obtained from the FWO

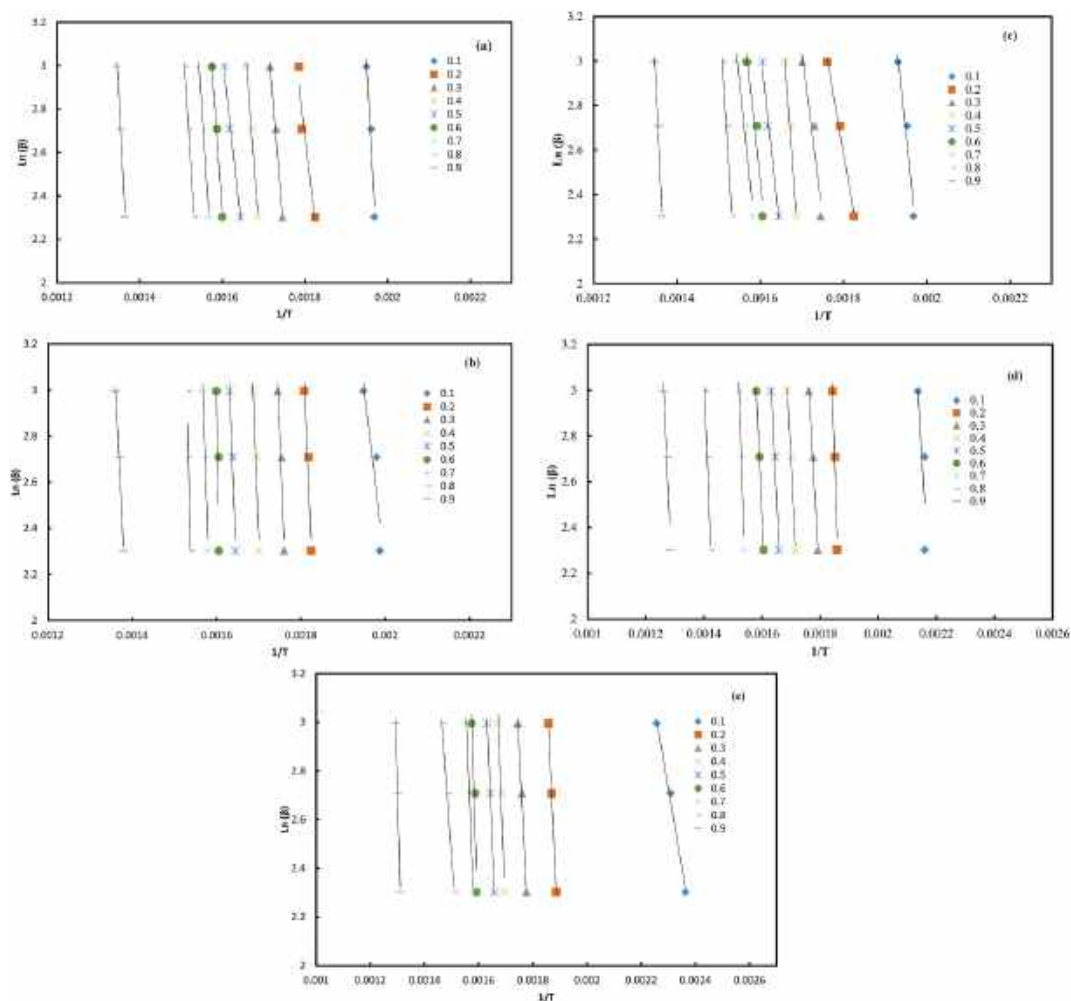


Fig. 3. Linear plots of FWO for (a) CS-Shell, (b) CS- Fe₂O₃/FeO, (c) CS-CuO, (d) CS- Fe₂O₃, (e), CS-ZnO pyrolysis at 10, 15 and 20 °C/min heating rates.

Table 4
The R-squared values of FWO plots.

R2					
α	CS	CS-Fe2O3/FeO	CS-CuO	CS-Fe2O3	CS-ZnO
0.1	0.988	0.828	0.988	0.923	0.993
0.2	0.983	0.956	0.992	0.965	0.998
0.3	0.991	0.978	0.996	0.996	0.991
0.4	0.941	0.966	0.991	0.992	0.986
0.5	0.990	0.956	0.990	0.995	0.994
0.6	0.991	0.967	0.986	0.991	0.981
0.7	0.991	0.956	0.993	0.985	0.993
0.8	0.993	0.978	0.991	0.991	0.994
0.9	0.992	0.992	0.994	0.985	0.993

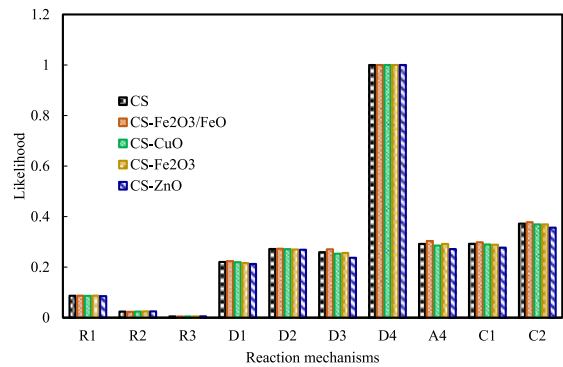


Fig. 4. Relative likelihood of models that govern the thermogravimetric pyrolysis of CS-shell and metal oxide-treated CS shells.

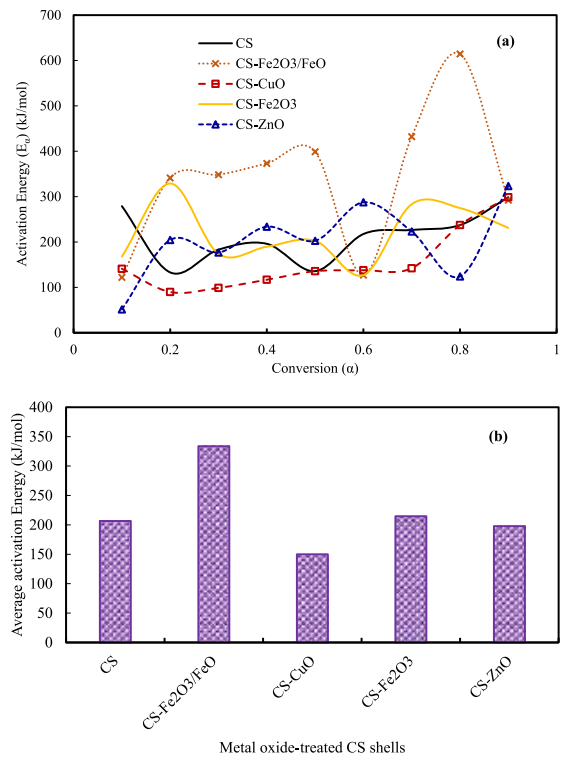


Fig. 5. Variation of (a) E_{α} with the degree of conversion (α) and (b) E_{α} for pyrolysis of CS-shell and metal-oxide treated CS Shells.

Table 5
Activation energy and frequency factors for CS-shell and metal oxide treated CS shells thermogravimetric pyrolysis from FWO method.

α	CS		CS-Fe2O3/FeO		CS-CuO		CS-Fe2O3		CS-ZnO			
	E α (kJ/mol)	A (s-1)	E α (kJ/mol)	A (s-1)	E α (kJ/mol)	A (s-1)	E α (kJ/mol)	A (s-1)	E α (kJ/mol)	A (s-1)	E α (kJ/mol)	A (s-1)
0.1	278.98	2.71E+17	122.07	48920.54	140.96	1673374.00	168.07	266228155.60	51.42	2.79E+17		
0.2	133.02	378289.98	341.24	3.09E+22	89.81	117.26	328.96	3.11E+21	204.47	378289.98		
0.3	183.18	44863546	348.36	1.17E+23	98.91	642.88	173.79	776207311	176.89	4486354562		
0.4	196.07	49981097469.00	373.19	1.22E+25	116.83	18334.98	189.57	14831239467	233.75	49981097469		
0.5	135.74	629022.5060.00	398.88	1.48E+27	135.73	629022.50	202.67	1.71E+11	202.67	629022.51		
0.6	217.60	2.81E+12	127.06	124130.35	137.78	923753.10	127.05	124130.34	287.49	2.81E+12		
0.7	226.68	1.53E+13	432.21	7.54E+29	142.18	2101083.00	283.31	6.09E+17	223.17	1.53E+13		
0.8	237.37	1.13E+14	614.49	4.82E+44	237.36	1.13E+14	274.79	1.24E+17	124.18	1.13E+14		
0.9	298.56	1.05E+19	292.13	3.17E+18	298.56	1.06E+19	231.02	3.45E+13	323.33	1.06E+19		
Average	211.91	1.20E+18	338.85	5.35E+43	155.35	1.17E+18	219.92	3.46E+20	203.04	1.20E+18		

method. The E_a for the CS-shell and metal oxides-treated CS shells vary with α (from 0.1 to 0.9) due to the complex and multi-step nature of the pyrolysis reactions [12,25]. In particular, the activation energies of CS-shell range between 133 and 298 kJ/mol. The large difference in the E_a values occurred from the complexity and multi-step reactions of pyrolysis degradation of the intertwined lignin, cellulose, and hemicellulose structure of the biomass [24,27]. On treating CS shells with the ZnO, CuO, $\text{Fe}_2\text{O}_3/\text{FeO}$, and Fe_2O_3 , the E_a varies in contrast to that of the CS-shell pyrolysis decomposition as shown in Table 5. This reveals that the metal oxides during the pyrolysis increase the complexity of the pyrolysis reactions through secondary reactions on the vapor. The variations in the ranges of E_a indicate that the metal oxides serving as catalysts altered the reaction pathways in different mechanisms, as revealed by the DTG curves, where peaks of vapor evolution vary.

Because of the degradation of lignin into biochar, the E_a are high when α is between 0.7 and 0.9 [3] due to the high thermal stability of lignin [28], irrespective of whether CS-shell is treated with metal oxide or not. The ZnO-treated CS-shell with exhibited a distinct pattern, as there is a decrease in E_a for conversion ranging between 0.6 and 0.8.

Fig. 5b presents the average E_a of the thermogravimetric pyrolysis of CS-shell and metal oxide-treated CS shells. The E_a for CS, CS- $\text{Fe}_2\text{O}_3/\text{FeO}$, CS-CuO, CS- Fe_2O_3 , and CS-ZnO are 211.91, 338.85, 155.35, 219.92, and 203.04 kJ/mol, respectively. The CuO and ZnO reduce the E_a from 211 kJ/mol of the CS-shell to 155 kJ/mol and 203 kJ/mol, respectively. The metal oxides as catalysts interact with volatiles after bond breakage of the CS-shell macrostructure and promote secondary reactions on the high molecular weight compounds. This finding conforms to the one reported in the literature [10,29]. However, the E_a for the shells treated with FeSO_4 and Fe_3O_4 first decomposed into Fe_2O_3 and $\text{Fe}_2\text{O}_3/\text{FeO}$, increasing the E_a from 211 to 338 kJ/mol and 219 kJ/mol, respectively, higher than that of the CS, CuO, and ZnO-treated CS-shell pyrolysis [30].

3.3. Thermodynamics parameters for CS-shell and metal oxide-treated CS-shell under thermogravimetric pyrolysis

The profiles of variations in change in enthalpy, ΔH , with the degree of conversion of the CS-shell, CS- $\text{Fe}_2\text{O}_3/\text{FeO}$, CS- Fe_2O_3 , CS-CuO, and CS-ZnO and their corresponding average values are presented in Fig. 6a and b, respectively.

The heat energy absorbed (Enthalpy, H) devolatilized the CS shell through structural bond breakage and caused weight loss from the release of vapor, which condenses to pyrolytic bio-oil. The change in Enthalpy (ΔH) varies with α (0.1–0.9) as depicted in Fig. 6a is positive for all the decomposition of CS-shell and metal oxide-treated CS shells. The average ΔH shown in Fig. 6b at 206.56, 333.58, 150, 214.65, and 197.78 kJ/mol are for the CS, CS- $\text{Fe}_2\text{O}_3/\text{FeO}$, CS-CuO, CS- Fe_2O_3 , and CS-ZnO degradations, respectively. These results established endothermic reactions prevailed in the entire degradation reactions in the active pyrolysis zone, this conforms to the findings reported in the literature [15]. The CS- $\text{Fe}_2\text{O}_3/\text{FeO}$ and CS- Fe_2O_3 decomposed with the highest average ΔH , which indicates that more energy is absorbed to propagate the pyrolysis degradation reactions. This is due to the energy absorbed to decompose the FeSO_4 to Fe_2O_3 and the IOD into the mixed iron oxides ($\text{Fe}_2\text{O}_3/\text{FeO}$), which are required to catalyze the pyrolysis secondary degradation reactions [18]. However, the average ΔH of the CS-CuO is 150 kJ/mol, which is less than the 206 kJ/mol required for the CS-shell. A similar finding was reported by Ling et al. [15] for the pyrolysis of palm kernel shells and plastic wastes. In addition, there was a slight decrease in the ΔH of CS-ZnO to 197 kJ/mol compared to 206 kJ/mol required for the CS shell. The reduction in the ΔH is due to the ease of decomposing $\text{Zn}(\text{NO}_3)_2$ to ZnO during the pyrolysis thermal decomposition [31].

The pattern of change in Gibb's free energy (ΔG) with the α of CS-shell, CS- $\text{Fe}_2\text{O}_3/\text{FeO}$, CS- Fe_2O_3 , CS-CuO, and CS-ZnO and the corresponding average ΔG are presented in Fig. 7a and b. Gibb's free energy decreases with the degree of conversion towards biochar formation for the CS-shell and metal oxide-treated CS-shell. This trend was reported in a study [32,33]. The ΔG has positive values for α (0.1–0.8) for CS-ZnO, 0.2 to 0.6 for CS-shell and CS-CuO, 0.3 to 0.7 for CS- Fe_2O_3 , and 0.1 to 0.2 and 0.6 to 0.7 for CS- $\text{Fe}_2\text{O}_3/\text{FeO}$. The values of the ΔG established that the reaction is non-spontaneous, which indicates that external thermal energy is needed for the pyrolysis reaction to occurs. Outside these ranges, the ΔG is negative, which establishes that the decomposition is spontaneous at those temperatures associated with the thermal inertia of the catalysts, which influences the pyrolysis reactions. The CS-shell treated with Fe species such as CS- Fe_2O_3 and CS- $\text{Fe}_2\text{O}_3/\text{FeO}$ has more reversibility and equilibrium tendency than CuO and ZnO-treated CS shells. The average ΔG of pyrolysis for CS- Fe_2O_3 and CS- $\text{Fe}_2\text{O}_3/\text{FeO}$ are 2 and 116 kJ, respectively.

Furthermore, the change in entropy (ΔS) varies with α and type of metal oxide used in the treatment of the CS Shells, as presented in Fig. 8. The ΔS is positive throughout the decomposition process, from 0.1 to 0.9, except for CS-CuO, which has a negative ΔS between 0.2 and 0.4. The variations of ΔS with α establish the complex nature of the thermogravimetric pyrolysis of the CS-shell and metal oxide-treated CS shells. The ΔS of CS and CS-ZnO follow a similar trend, which decreases as the α increases from 0.1 to 0.2. The decrease in ΔS might be due to the evolution of volatiles, mostly water vapor, which reduces the degree of disorderliness. However, the ΔS of those CS shells treated with IOD and FeSO_4 salts, CS- $\text{Fe}_2\text{O}_3/\text{FeO}$ and Fe_2O_3 respectively, increases from 0.1 to 0.5 due to thermal inertia, which releases more heat to the vapor, thus with the high degree of disorderliness. At 0.6 degrees of conversion, the release of volatiles increased eventually lower the degree of disorder [12]. The value of ΔS is positive at the 0.6 conversion degree, but the ΔS has decreased drastically. This is because of the increased rate of decomposition of the CS-shell macrostructure, which releases more volatiles and decreases the degree of disorderliness of the vapor molecules.

4. Conclusion

1. The degradation behavior of CS-shell and metal oxide-treated CS-shell samples was examined using TGA up to 800 °C under 10, 15, and 20 °C/min heating rates. Peak maximum temperatures shifted by about 5 °C as heating rates increased. The DTG curve analysis revealed unique decomposition patterns having characteristic peaks. The peaks were observed between 350 and 380 °C, with significant degradation taking place between 200 and 600 °C.

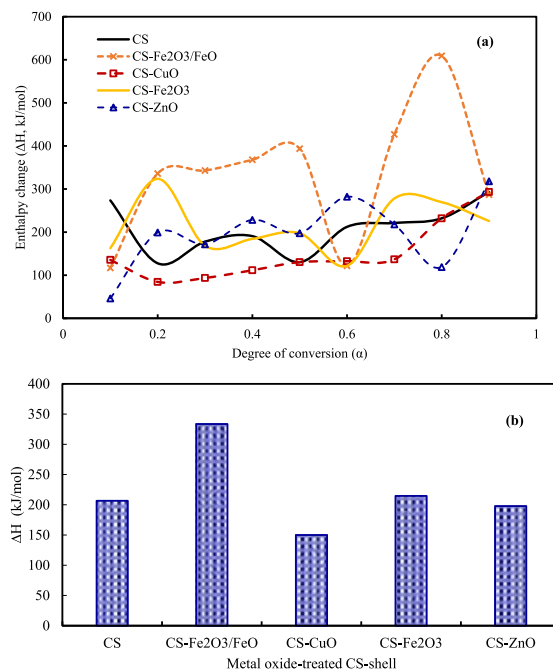


Fig. 6. Variation of (a) ΔH with the degree of conversion (α) and (b) ΔH for pyrolysis of CS-shell and metal-oxide treated CS Shells.

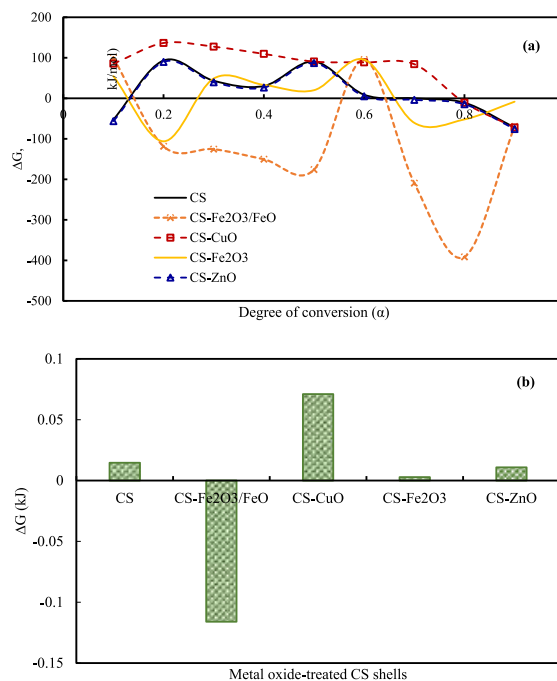


Fig. 7. Variation of (a) ΔG with the degree of conversion (α) and (b) Average ΔG for pyrolysis of CS-shell and metal-oxide treated CS Shells.

2. The activation energies for pyrolysis of CS shells treated with ZnO, CuO, Fe₂O₃, and Fe₂O₃/FeO are 118.15, 142.81, and 139.56 kJ/mol, respectively differ from CS shell pyrolysis. As a result, the metal oxide altered various pyrolysis reactions propagated by the Gistling-Brounshtein model's diffusion-controlled mechanism, as determined by Bayesian information criteria.
3. The study provides kinetics and thermodynamics parameters for pyrolysis of CS shells treated with ZnO, CuO, Fe₂O₃, and Fe₂O₃/FeO that are not well documented in the literature.

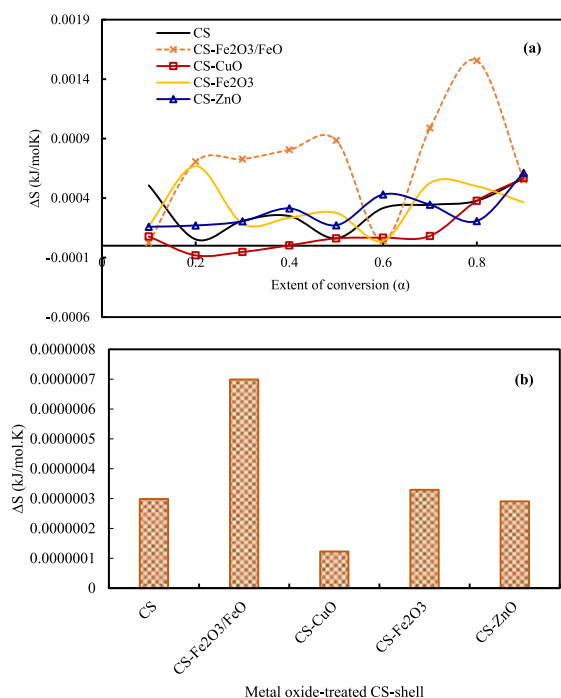


Fig. 8. Variation of (a) ΔS with a degree of conversion (α) and (b) ΔS for pyrolysis of CS-shell and metal-oxide treated CS-Shell.

- The kinetic models for the metal oxide-treated CS shell demonstrated excellent fitting performance, with R^2 values ranging up to 0.99. This suggested that kinetic modeling has the potential to be an effective tool for evaluating complex degradation processes, thus paving the way for new avenues of research into biomass utilization.
- The kinetic modeling results based on the TGA/DTG analyses revealed the understanding of metal oxide-treated CS-shell decomposition, which can inform the development of efficient thermochemical conversion systems.
- The study advocates for the extensive use of different metal oxides, especially those obtained from readily available iron ore dust, in the catalytic pyrolysis of CS shells for bioenergy and chemical recovery.

Data availability

Data will be made available on request.

CRediT authorship contribution statement

Kabir Garba: Writing – review & editing, Writing – original draft, Supervision, Methodology, Investigation, Formal analysis, Data curation, Conceptualization. **Habu Iyodo Mohammed:** Writing – review & editing, Writing – original draft, Methodology, Investigation, Formal analysis, Conceptualization. **Yusuf Makarfi Isa:** Writing – review & editing, Methodology, Investigation, Formal analysis, Conceptualization.

Declaration of competing interest

There are no competing financial or personal interests that could have appeared to affect the study reported in the research paper.

Acknowledgments

The authors acknowledge the research grants provided by the Tertiary Education Trust (TETFund) of Nigeria, under the Institutional Based Research grant (IBR) (Project No: TETFund/DR&D/CE/IBR/2023) that resulted in this article.

References

- M. Jia, B. Fong, A. Chun, M. Loy, B. Lai, F. Chin, M.K. Lam, S. Yusup, Z. Abbas, Catalytic pyrolysis of *Chlorella vulgaris*: kinetic and thermodynamic analysis, *Bioresour. Technol.* 289 (2019) 121689, <https://doi.org/10.1016/j.biortech.2019.121689>.

- [2] C. Zhang, C. Wang, R. Tao, J. Ye, Thermal stability and thermal decomposition kinetics of Ginkgo biloba leaves waste residue, *Therm. Sci.* 22 (2018) 1059–1069, <https://doi.org/10.2298/TSCT170117154Z>.
- [3] H.I. Mohammed, K. Garba, S.I. Ahmed, L.G. Abubakar, Thermodynamics and kinetics of Doum (Hyphaene thebaica) shell using thermogravimetric analysis : a study on pyrolysis pathway to produce bioenergy, *Renew. Energy* 200 (2022) 1275–1285, <https://doi.org/10.1016/j.renene.2022.10.042>.
- [4] M.A. Islam, M. Auta, G. Kabir, B.H. Hameed, A thermogravimetric analysis of the combustion kinetics of karanja (Pongamia pinnata) fruit hulls char, *Bioresour. Technol.* 200 (2016) 335–341, <https://doi.org/10.1016/j.biortech.2015.09.057>.
- [5] Z. Ma, D. Chen, J. Gu, B. Bao, Q. Zhang, Determination of pyrolysis characteristics and kinetics of palm kernel shell using TGA – FTIR and model-free integral methods, *Energy Convers. Manag.* 89 (2015) 251–259, <https://doi.org/10.1016/j.enconman.2014.09.074>.
- [6] M.S. Ahmad, M.A. Mehmood, S.T.H. Taqvi, A. Elkamel, C.G. Liu, J. Xu, S.A. Rahimuddin, M. Gull, Pyrolysis, kinetics analysis, thermodynamics parameters and reaction mechanism of Typha latifolia to evaluate its bioenergy potential, *Bioresour. Technol.* 245 (2017) 491–501, <https://doi.org/10.1016/j.biortech.2017.08.162>.
- [7] I. Jia, Y. Tan, A. Chun, M. Loy, B. Lai, F. Chin, K. Wai, Green Technologies and Sustainability Co-pyrolysis of Chlorella vulgaris with plastic wastes : thermal degradation , kinetics and Progressive Depth Swarm-Evolution (PDSE) neural network-based optimization, *Green Technol. Sustain* 2 (2024) 100077, <https://doi.org/10.1016/j.grets.2024.100077>.
- [8] K. Garba, I. Yakub, Y. Makarfi, L. Garba, Y. Abdalla, B.H. Hameed, Heliyon Pyrolysis of Canarium schweinfurthii hard-shell : thermochemical characterisation and pyrolytic kinetics studies, *Heliyon* 9 (2023) e13234, <https://doi.org/10.1016/j.heliyon.2023.e13234>.
- [9] W.A. Wibowo, R.B. Cahyono, R. Rochmadi, A. Budiman, Kinetics of in-situ catalytic pyrolysis of rice husk Pellets using a multi-Component kinetics, *Model* 18 (2023) 85–102, <https://doi.org/10.9767/bcrec.17226>.
- [10] W. Agung, R. Bakht, A. Budiman, Thermogravimetric analysis and kinetic study on catalytic pyrolysis of rice husk pellet using its ash as a low-cost in-situ, *Catalyst* 11 (2022) 207–219, <https://doi.org/10.14710/ijred.2022.41887>.
- [11] Y. Yee, C. Hoon, K. Ng, L. Yee, L. Suyin, G. Suchithra, T. Gopakumar, Kinetics and mechanisms for catalytic pyrolysis of empty fruit bunch fibre and cellulose with oxides, *SN Appl. Sci.* 2 (2020) 1–14, <https://doi.org/10.1007/s42452-020-03249-1>.
- [12] D. Kin, W. Gan, A. Chun, M. Loy, B. Lai, F. Chin, S. Yusup, P. Unrean, E. Rianawati, M.N. Acda, Bioresource Technology Kinetics and thermodynamic analysis in one-pot pyrolysis of rice hull using renewable calcium oxide based catalysts, *Bioresour. Technol.* 265 (2018) 180–190, <https://doi.org/10.1016/j.biortech.2018.06.003>.
- [13] H. Yang, G. Ji, P.T. Clough, X. Xu, M. Zhao, Kinetics of catalytic biomass pyrolysis using Ni-based functional materials, 195, <https://doi.org/10.1016/j.fuproc.2019.106145>, 2019.
- [14] M. Guida, H. Bouaik, E.M. L. A. Moubarik, A. Aboulkas, K. El harfi, A. Hannioui, Utilization of Starink approach and avrami theory to evaluate the kinetic parameters of the pyrolysis of olive mill solid waste and olive mill wastewater, *J. Adv. Chem. Eng.* 7 (2017) 1–8, <https://doi.org/10.4172/2090-4568.1000155>.
- [15] A. Ling, K. Chee, B. Lai, F. Chin, S. Meng, X. Goh, Y. Ho, A. Chun, M. Loy, K. Wai, C. Loong, S. Sow, M. Lock, Thermo-catalytic co-pyrolysis of palm kernel shell and plastic waste mixtures using bifunctional HZSM-5/limestone catalyst : kinetic and thermodynamic insights, *J. Energy Inst.* 107 (2023) 101194, <https://doi.org/10.1016/j.joei.2023.101194>.
- [16] H. Persson, I. Duman, S. Wang, L.J. Pettersson, W. Yang, Catalytic pyrolysis over transition metal-modified zeolites: a comparative study between catalyst activity and deactivation, *J. Anal. Appl. Pyrolysis* (2018), <https://doi.org/10.1016/j.jaap.2018.12.005>.
- [17] P. He, W. Shan, Y. Xiao, H. Song, Performance of Zn/ZSM-5 for in situ catalytic upgrading of pyrolysis bio-oil by methane, *Top. Catal.* (2015), <https://doi.org/10.1007/s11244-015-0508-4>.
- [18] Y. V. Lugovoy, K. V. Chalov, Y.Y. Kositsov, E.M. Sulman, G. Mikhail, Pyrolysis of Agricultural Waste in the Presence of Fe-Subgroup Metal-Containing Catalysts, *Vol. 76, 2019*, pp. 1453–1458, <https://doi.org/10.3303/CET1976243>.
- [19] H. Xia, X. Yan, S. Xu, L. Yang, Y. Ge, J. Wang, S. Zuo, Effect of Zn/ZSM-5 and FePO 4 Catalysts on Cellulose Pyrolysis, 2015, p. 2015.
- [20] V. Savou, S. Kumagai, Y. Saito, T. Kameda, T. Yoshioka, Effects of acetic acid pretreatment and pyrolysis temperatures on product recovery from Fijian sugarcane bagasse, *Waste and Biomass Valorization* (2019), <https://doi.org/10.1007/s12649-019-00866-9>.
- [21] M. Jabłońska, M. Rachwał, M. Wa, M.K. Gawel, E. Teper, Mineralogical and Chemical Specificity of Dusts Originating from Iron and Non-ferrous Metallurgy in the Light of Their Magnetic Susceptibility, 2021, pp. 1–20.
- [22] P. Wang, B.H. Howard, Impact of thermal pretreatment temperatures on woody biomass chemical composition, physical properties and microstructure, *Energies* 11 (2018) 1–20, <https://doi.org/10.3390/en11010025>.
- [23] J. Chen, X. Fan, B. Jiang, L. Mu, P. Yao, H. Yin, X. Song, Pyrolysis of oil-plant wastes in a TGA and a fixed-bed reactor : thermochemical behaviors , kinetics , and products characterization, *Bioresour. Technol.* 192 (2015) 592–602, <https://doi.org/10.1016/j.biortech.2015.05.108>.
- [24] C.L. Waters, R.R. Janupala, R.G. Mallinson, L.L. Lobban, Staged thermal fractionation for segregation of lignin and cellulose pyrolysis products: an experimental study of residence time and temperature effects, *J. Anal. Appl. Pyrolysis* 126 (2017) 380–389, <https://doi.org/10.1016/j.jaap.2017.05.008>.
- [25] S. Vyazovkin, A.K. Burnham, L. Favergeon, N. Koga, E. Moukhina, L.A. Pérez-maqueda, N. Sbirrazzuoli, Thermochimica Acta ICTAC Kinetics Committee recommendations for analysis of multi-step kinetics, *Thermochim. Acta* 689 (2020) 178597, <https://doi.org/10.1016/j.tca.2020.178597>.
- [26] S. Vyazovkin, A.K. Burnham, J.M. Criado, L.A. Pérez-maqueda, C. Popescu, N. Sbirrazzuoli, Thermochimica Acta ICTAC Kinetics Committee recommendations for performing kinetic computations on thermal analysis data, *Thermochim. Acta* 520 (2011) 1–19, <https://doi.org/10.1016/j.tca.2011.03.034>.
- [27] G. Kabir, B.H. Hameed, Recent progress on catalytic pyrolysis of lignocellulosic biomass to high- grade bio-oil and bio-chemicals, *Renew. Sustain. Energy Rev.* 70 (2016) 945–967, <https://doi.org/10.1016/j.rser.2016.12.001>.
- [28] F. Surahmanto, H. Saptoadi, H. Sulisty, T.A. Rohmat, Effect of heating rate on the slow pyrolysis behaviour and its kinetic parameters of oil-palm shell, *Int. J. Renew. Energy Res.* 7 (2017) 1138–1144.
- [29] Y. Zheng, J. Wang, C. Liu, Y. Lu, X. Lin, W. Li, Z. Zheng, Catalytic copyrolysis of metal impregnated biomass and plastic with Ni-based HZSM-5 catalyst : synergistic effects , kinetics and product distribution, *Int. J. Energy Res.* 44 (2020) 5917–5935, <https://doi.org/10.1002/er.5370>.
- [30] N. Kanari, N.E. Menad, E. Ostrosi, S. Shallari, F. Diot, E. Allain, J. Yvon, Thermal behavior of hydrated iron sulfate in various atmospheres, *Metals* 8 (2018) 1–9, <https://doi.org/10.3390/met8121084>.
- [31] Q. Lu, Z.F. Zhang, C.Q. Dong, X.F. Zhu, Catalytic upgrading of biomass fast pyrolysis vapors with nano metal oxides: an analytical Py-GC/MS study, *Energies* 3 (2010) 1805–1820, <https://doi.org/10.3390/en3111805>.
- [32] T. Li, A. Chun, M. Loy, B. Lai, F. Chin, J. Yau, H. Alhamzi, Y. Ho, C. Loong, K. Wai, M. Xin, J. Wee, M. Kee, Z. Abbas, S. Yusup, S. Sow, M. Lock, Synergistic effects of catalytic co-pyrolysis Chlorella vulgaris and polyethylene mixtures using artificial neuron network : thermodynamic and empirical kinetic analyses, *J. Environ. Chem. Eng.* 10 (2022) 107391, <https://doi.org/10.1016/j.jece.2022.107391>.
- [33] Q. Wang, H. Song, S. Pan, N. Dong, X. Wang, S. Sun, Initial pyrolysis mechanism and product formation of cellulose : an Experimental and Density functional theory (DFT) study, *Sci. Rep.* (2020) 1–18, <https://doi.org/10.1038/s41598-020-60095-2>.

Sustainable Energy Technologies and Assessments

[Submit your article](#)[Menu](#)[Search in this journal](#)

Volume 55

February 2023

[!\[\]\(faf942dc3e59ce8eb64b4ac481eca7e0_img.jpg\) Download full issue](#)[< Previous vol/issue](#)[Next vol/issue >](#)

Receive an update when the latest issues in this journal are published

[Sign in to set up alerts](#)

Full text access

Editorial Board

Article 103013

[View PDF](#)

Sustainable Energy Technologies and Assessments

Submit your article



Yidan Huang, Yi Shi, Jiuping Xu

Article 102890

Article preview

Research article ☐ Abstract only

The application of a new design of bat optimizer for energy efficiency enhancement in PEMFCs based on fractional order theory

Xuchang Hu, Weigang Jiang, Xinyang Ying, Mahdiah Eslami

Article 102904

Article preview

Research article ☐ Abstract only

Impact of solid and hollow bluff bodies on the performance and dynamics of flag-based energy harvester

U. Latif, M.Y. Younis, E. Uddin, Z. Ali, ... A. Abdelkefi

Article 102882

Article preview

Research article ☐ Abstract only

Electron transfer by ion conductance in a soil bioelectric field

Ting Han, Xiaodong Chen, Kai Wang, Iranzi Emile Rushimisha, ... Xiaojing Li

Article 102902

Article preview

Sustainable Energy Technologies and Assessments

Submit your article




Article preview 

Research article ☐ Abstract only

Cavitation diagnosis for water distribution pumps: An early-stage approach combining vibration signal-based neural network with high-speed photography

Zheming Tong, Hao Liu, Xiangkun Elvis Cao, Dane Westerdahld, Xiaofeng Jin

Article 102919

Article preview 

Research article ☐ Abstract only

Responsible ownership fostering green tech innovation

Gudrun Erla Jonsdottir, Jordan Mitchell, Throstur Olaf Sigurjonsson, Ahmad Rahnema Alavi

Article 102923

Article preview 

Research article ☐ Abstract only

Efficient and high-power subsea bubble energy harvesting by controlling flow pattern

Zhibin Guan, Ping Li, Yumei Wen, Yu Du, Guoda Wang

Article 102898

Article preview 

Research article ☐ Abstract only

Optimal energy management of nanogrid using battery storage system

Sustainable Energy Technologies and Assessments

Submit your article



System dynamics characterisation and synthesis of heating photovoltaics in terms of energy, environmental and economic parameters with WELF nexus sustainability features

F.C. Prinsloo, Peter Schmitz, Andrea Lombard

Article 102901

Article preview

Research article ☒ Open access

A geospatial assessment of the techno-economic wind and solar potential of Mongolia

Alexander Harrucksteiner, Jagruti Thakur, Katja Franke, Frank Sensfuß

Article 102889



[View PDF](#)

Article preview

Research article ☐ Abstract only

Life cycle assessment of a carbon capture utilization and storage supply chain in Italy and Germany: Comparison between carbon dioxide storage and utilization systems

Grazia Leonzio, I. David L. Bogle, Pier Ugo Foscolo

Article 102743

Article preview

Research article ☐ Abstract only

Vehicle-to-ski: A V2G optimization-based cost and environmental analysis for a ski resort

Sustainable Energy Technologies and Assessments

Submit your article



Research on a novel non-linear magnetically coupled piezoelectric self-powered mouse

Shuangjian Wang, Lipeng He, Xuejin Liu, Lei Sun, ... Guangming Cheng

Article 102940

Article preview

Research article ☐ Abstract only

Techno-economic analysis of a cooling, heating, and electricity trigeneration system based on downdraft fixed bed wood and tire gasification: Case study of a campus office building

Guiyan Zang, Jianan Zhang, Albert Ratner, Yunye Shi

Article 102939

Article preview

Research article ☐ Abstract only

Understanding the power disruption and its impact on community development: An empirical case of Pakistan

Shahid Hussain, Wang Xuetong, Rashid Maqbool

Article 102922

Article preview

Research article ☐ Abstract only

Sustainability analyses of CO₂ sequestration and CO₂ utilization as competing options for mitigating CO₂ emissions

Sustainable Energy Technologies and Assessments

Submit your article



~~A stochastic optimal scheduling of distributed energy resources with electric vehicles~~ based on microgrid considering electricity price

Tao Hai, Ammar K. Alazzawi, Jasni Mohamad Zain, Hitoshi Oikawa

Article 102879

Article preview

Research article ☒ Open access

Techno environmental assessment of Flettner rotor as assistance propulsion system for LH₂ tanker ship fuelled by hydrogen

Abdullah NFNR Alkhaledi, Suresh Sampath, Pericles Pilidis

Article 102935



[View PDF](#)

Article preview

Research article ☐ Abstract only

A low-carbon optimization design method for building roof insulation using comprehensive economic analysis model and evaluation index

Haitao Wang, Yuge Huang, Chengzhou Guo, Liu Yang, Lu Huang

Article 102937

Article preview

Research article ☐ Abstract only

Design of novel flow channels of tubular biomass-syngas fueled SOFC towards uniform temperature distribution

Zhen Wu, Pengfei Zhu, Jing Yao, Mohd Radzi Abu Mansor, ... Si-Min Huang

Article 102947

Sustainable Energy Technologies and Assessments

Submit your article



Oludamilare Bode Adewuyi, Mark Kipngetich Kiptoo, Isaiah Gbadegesin Adebayo, Oluwatobi Idowu Adewuyi, Tomonobu Senjyu
Article 102943

Article preview

Research article ☐ Abstract only

A newly developed renewable energy driven multigeneration system with hot silica sand storage for power, hydrogen, freshwater and cooling production

Arda Yapicioglu, Ibrahim Dincer
Article 102938

Article preview

Research article ☐ Abstract only

Research on thermoacoustic refrigeration system driven by waste heat of industrial buildings

Xiachen Ding, Zhuo Chen, Huifang Kang, Lingxiao Zhang
Article 102971

Article preview

Research article ☐ Abstract only

A techno-economic and socio-environmental planning of wind farms for sustainable development and transition to a decarbonized scenario: Pakistan as a case study

Mohammad Uzair Shah, Saeeda Khanum, Adeel Waqas, Abdul Kashif Janjua, Sehar Shakir
Article 102969

Sustainable Energy Technologies and Assessments

Submit your article



Anand Narhari Sonsale, Yashpal, S.D. Pohekar, J.K. Purohit

Article 102961

Article preview

Research article ☐ Abstract only

Biodegradation of mixed hydrocarbon and eicosane by novel *Enterococcus mundtii* SS1 isolated from automobile service station soil

Swati Patel, Gaurav Shah

Article 102993

Article preview

Research article ☐ Abstract only

Feasibility analysis of floating photovoltaic power plant in Bangladesh: A case study in Hatirjheel Lake, Dhaka

Md. Imamul Islam, Md Hasan Maruf, Ahmed Al Mansur, Ratil H. Ashique, ... Mohd Shawal Jadin

Article 102994

Article preview

Research article ☐ Abstract only

Diagnosis for the refrigerant undercharge fault of chiller using deep belief network enhanced extreme learning machine

Pengcheng Li, Burkay Anduv, Xu Zhu, Xinqiao Jin, Zhimin Du

Article 102977

Article preview

Sustainable Energy Technologies and Assessments

[Submit your article](#)[View PDF](#)[Article preview](#)

Research article ☐ Abstract only

Theoretical technical–economic comparison of hybrid energy for gas and solar concentration plants in the Region of Antofagasta Chile

Catalina Hernández Moris, Carlos Felbol, Maria Teresa Cerda, Mercedes Ibarra

Article 102979

[Article preview](#)

Research article ☐ Abstract only

Natural convective greenhouse vermicelli drying: Thermo-environ-econo-kinetic analyses

Mahesh Kumar, Shimpy, Ravinder Kumar Sahdev, M.A. Tawfik, Nouredine Elboughdiri

Article 103002

[Article preview](#)

Review Articles

Review article ☐ Abstract only

Solar energy: A promising renewable source for meeting energy demand in Indian agriculture applications

Ch. Mohan Sai Kumar, Suman Singh, Manglesh Kumar Gupta, Yogesh M. Nimdeo, ... Ashween Deepak Nannaware

Article 102905

[Article preview](#)

Sustainable Energy Technologies and Assessments

Submit your article



Article preview 

Review article ☐ Abstract only

A comprehensive review on the production of alternative fuel through medical plastic waste

Amit Kumar, Harveer Singh Pali, Manoj Kumar

Article 102924

Article preview 

Review article ☐ Abstract only

Green building technologies in Southeast Asia: A review

Fei Lai, Jinzhi Zhou, Lin Lu, M. Hasanuzzaman, Yanping Yuan

Article 102946

Article preview 

Review article ☐ Abstract only

Interdisciplinary analysis of wind energy - a focus on France

Khadija EL Kinani, Simon Meunier, Lionel Vido, Sandrine Le Ballois

Article 102944

Article preview 

Review article ☐ Abstract only

Photovoltaic pavement and solar road: A review and perspectives

Sustainable Energy Technologies and Assessments

Submit your article



A review on recent advances in hybrid solar updraft tower plants: Challenges and future aspects

Pritam Das, Chandramohan V.P.

Article 102978

Article preview

Review article ☐ Abstract only

Core-Shell structures for the enhancement of energy harvesting in piezoelectric Nanogenerators: A review

Sara M. AlTowireb, Souraya Goumri-Said

Article 102982

Article preview

Review article ☐ Abstract only

Recent advances on strategies for upgrading biomass pyrolysis vapour to value-added bio-oils for bioenergy and chemicals

Habu Iyodo Mohammed, Kabir Garba, Saeed Isa Ahmed, Lawan Garba Abubakar

Article 102984

Article preview

Special Section on Energy Technologies

Research article ☐ Abstract only

Does renewable energy technological innovation matter for green total factor productivity? Empirical evidence from Chinese provinces

Sustainable Energy Technologies and Assessments

Submit your article



Research article ☐ Abstract only

Spatio-temporal fluctuations analysis of land surface temperature (LST) using Remote Sensing data (LANDSAT TM5/8) and multifractal technique to characterize the urban heat Islands (UHIs)

Sanjeev Kimothi, Asha Thapliyal, Anita Gehlot, Arwa N. Aledaily, ... Shaik Vaseem Akram
Article 102956

Article preview

Research article ☐ Abstract only

Constructed wetland challenges for the treatment of industrial wastewater in smart cities: A sensitive solution

Amrutashree Hota, S Gopal Krishna Patro, Ahmed J. Obaid, Satish Khatak, Raghvendra Kumar
Article 102967

Article preview

Special Section on FREES

Research article ☐ Abstract only

Exploring the trends in construction and demolition waste (C&DW) research: A scientometric analysis approach

Ahsan Nawaz, Jian Chen, Xing Su
Article 102953

Article preview

Sustainable Energy Technologies and Assessments

Submit your article



Article 102987

Article preview

Special Section on Internet of Things

Research article ☐ Abstract only

Research on path tracking algorithm of green agricultural machinery for sustainable development

Jie Zhang, Dan Li

Article 102917

Article preview

Research article ☐ Abstract only

Driving mechanism of digital economy based on regulation algorithm for development of low-carbon industries

Xuetao Li, Hong Wang, Chengying Yang

Article 102909

Article preview

Special Section on IOT & Wirelss Energy Harvesting

Research article ☐ Abstract only

An intelligent energy efficient optimized approach to control the traffic flow in Software-Defined IoT networks

Sustainable Energy Technologies and Assessments

Submit your article



Research article ☐ Abstract only

A role distinguishing Bert model for medical dialogue system in sustainable smart city

Suixue Wang, Shuling Wang, Zhuo Liu, Qingchen Zhang

Article 102896

Article preview

Research article ☐ Abstract only

An energy cooperation method of wireless sensor networks based on partially observable Markov decision processes

Qin Zhang, Yutang Liu

Article 102997

Article preview

Research article ☐ Abstract only

A big-data-based recurrent neural network method for forest energy estimation

Yang Song, Youzhi Wang

Article 102910

Article preview

Special Section on AHU & Renewable Energies

Research article ☐ Abstract only

Sustainable Energy Technologies and Assessments

Submit your article



Special Section on BEST

Research article ☐ Abstract only

Performance and emission characteristics of micro-algae biodiesel with butanol and TiO₂ nano-additive over diesel engine

Suraj Verma, Rakesh Upadhyay, Ravi Shankar, Satya Prakash Pandey

Article 102975

Article preview

Special Section on Biomass to Biofuels

Research article ☐ Abstract only

Utilization of nanomaterials in accelerating the production process of sustainable biofuels

Shams Forruque Ahmed, J.C. Debnath, Fatema Mehejabin, Nafisa Islam, ... Dai-Viet N. Vo

Article 102894

Article preview

Research article ☐ Abstract only

A prospective study on the environmental feasibility of supplying electricity to the Brazilian Amazon through biogas power generation

Denis Silva Miranda, Luiz Kulay

Article 102962

Article preview

Sustainable Energy Technologies and Assessments

Submit your article



Article preview

Research article ☐ Abstract only

Techno-economic assessment and logistics management of biomass in the conversion progress to bioenergy

Viet Duc Bui, Hoang Phuong Vu, Hoang Phuong Nguyen, Xuan Quang Duong, ... Phuoc Quy Phong Nguyen

Article 102991

Article preview

Special Section on Green Building: TAP

Research article ☐ Abstract only

Optimization and sustainability analysis of a hybrid diesel-solar-battery energy storage structure for zero energy buildings at various reliability conditions

Zhihan Zhang, Kehuan Wen, Wenjing Sun

Article 102913

Article preview

Research article ☐ Abstract only

A comprehensive and updated review on the exergy analysis of ground source heat pumps

Rongsheng Liu, Mohamed Salem, Jaroon Rungamornrat, Mohammed Al-Bahrani

Article 102906

Article preview

Sustainable Energy Technologies and Assessments

Submit your article



Special Section on Green Energy Technologies

Research article ☐ Abstract only

Experimental and empirical analysis of performance, combustion and emission characteristics of diesel engine fueled with pyrolysis waste engine oil under single and split injection strategy

A. Santhoshkumar, Vinoth Thangarasu, Anand Ramanathan

Article 102893

Article preview

Research article ☐ Abstract only

A novel coupled microbial fuel cell operation for organic and nitrogen removal with simultaneous energy recovery from wastewater

Hoang Dung Nguyen, Sandhya Babel

Article 102981

Article preview

Special Section on Adv & FP in Energy HT

Research article ☐ Abstract only

A hybrid technique to control superheater steam temperature in power plants using multi modeling and predictive sliding mode control

S. Prasanth, S. Narayanan, N. Sivakumaran, R.S. Sharanya Rominus

Sustainable Energy Technologies and Assessments

Submit your article



Seamless plug-in plug-out enabled fully distributed peer-to-peer control of prosumer-based islanded AC microgrid

Shamsher Ansari, Aseem Chandel, Mohd Tariq

Article 102958

Article preview

Special Section on Second Law in RES

Research article ☐ Abstract only

Experimental investigation of a hybridized flat-plate solar collector/gas burner for low-carbon production of hot water – Analysis of energy, exergy, and GHG emissions

Peyman Soleymani, Seyfolah Saedodin, Seyed Hadi Rostamian, Nader Karimi

Article 102918

Article preview

Research article ☐ Abstract only

Exergy efficiency and entropy analysis of MWCNT/Water nanofluid in a thermosyphon flat plate collector

Kotturu V.V. Chnadra Mouli, L. Syam Sundar, A.M. Alklaibi, Zafar Said, ... Antonio C.M. Sousa

Article 102911

Article preview

Research article ☐ Abstract only

Sustainable Energy Technologies and Assessments

Submit your article



Special Section on Sustainable Development

Research article ☐ Abstract only

Co-digestion of domestic kitchen food waste and palm oil mill effluent for biohydrogen production

Tao Hai, Puranjan Mishra, Jasni Mohamad Zain, Karuna Saini, ... Zularisam Ab Wahid
Article 102965

Article preview

Research article ☐ Abstract only

Experimental verification of a dynamic programming and IoT-based simultaneous load-sharing controller for residential homes powered with grid and onsite solar photovoltaic electricity

Sujon Mia, Amit Kumer Podder, Nallapaneni Manoj Kumar, Ankit Bhatt, Krishna Kumar
Article 102964

Article preview

Research article ☐ Abstract only

Computational analysis of chlorella protothecoides biofuels on engine combustion, performance and emission

Sujeet Kesharvani, Tikendra Nath Verma, Gaurav Dwivedi
Article 102972

Article preview

Sustainable Energy Technologies and Assessments

Submit your article



Article preview 

Special Section on WHR Sustainable Society

Research article ☐ Abstract only

A low-temperature driven organic Rankine cycle for waste heat recovery from a geothermal driven Kalina cycle: 4E analysis and optimization based on artificial intelligence

Tao Hai, Masood Ashraf Ali, Rishabh Chaturvedi, Sattam Fahad Almojil, ... Mohamed A. Shamseldin
Article 102895

Article preview 

Research article ☐ Abstract only

Design, 3E scrutiny, and multi-criteria optimization of a trigeneration plant centered on geothermal and solar energy, using PTC and flash binary cycle

Amin Eskandari
Article 102718

Article preview 

Research article ☐ Abstract only

Techno-economic assessment of small-scale gas to liquid technology to reduce waste flare gas in a refinery plant

Kaveh Zayer Kabeh, Aidin Teimouri, Sina Changizian, P. Ahmadi
Article 102955

Article preview 

Sustainable Energy Technologies and Assessments

Submit your article



Hydrogen Energy System Considering Demand Response

Alper Çiçek

Article 102957

Article preview

Special Section on Energy Storage Systems

Research article ☐ Abstract only

A multi-agent petri net model power management strategy for wind–solar-battery driven DC microgrid

Jyotismita Mishra, Pradyumna Kumar Behera, Monalisa Pattnaik, B. Chitti Babu

Article 102859

Article preview

Special Section on PSET

Research article ☐ Abstract only

Dynamic coordinated control strategy of power on gear shifting for novel dual motor electric vehicle

Qicheng Xue, Xin Zhang, Teng Teng, Meiling Yue

Article 102941

Article preview

Research article ☐ Abstract only

Sustainable Energy Technologies and Assessments

Submit your article



Research article ☐ Abstract only

Research progress of hydrogen energy and metal hydrogen storage materials

Yongyan Xu, Yuan Deng, Wei Liu, Xin Zhao, ... Zeming Yuan

Article 102974

Article preview

Research article ☐ Abstract only

Innovation evolution of industry-university-research cooperation under low-carbon development background: In case of 2 carbon neutrality technologies

Huijie Zhou, Xinman Zhu, Jie Dai, Wenbin Wu

Article 102976

Article preview

Research article ☐ Abstract only

Comparison, evaluation and prioritization of solar photovoltaic tracking systems using multi criteria decision making methods

Seyyed Shahabaddin Hosseini Dehshiri, Bahar Firoozabadi

Article 102989

Article preview

Research article ☐ Abstract only

Sustainable Energy Technologies and Assessments

Submit your article



Special Section on DT Modern DistriGridAuto

Research article ☐ Abstract only

A two-way pre-installation assessment framework for microgrids under power systems expansion planning

Fawad Azeem, Zulfiqar Ali Memon, Sobia Baig, Ahmed Bilal Awan

Article 102920

Article preview

Special Section on Enrg Tec: BioMS Rclng

Research article ☐ Abstract only

Automated biomass recycling management system using modified grey wolf optimization with deep learning model

Sara A Althubiti, Sanjay Kumar Sen, Mohammed Altaf Ahmed, E. Laxmi Lydia, ... Deepak Gupta

Article 102936

Article preview

Special Section on Trends for R/HP systems

Research article ☐ Abstract only

Evaluation of machine learning approaches for estimating thermodynamic properties of new generation refrigerant R513A

Sustainable Energy Technologies and Assessments

Submit your article



Progressive development in hybrid liquid desiccant vapour compression cooling system: A review

Kashish Kumar, Alok Singh, Prem Kumar Chaurasiya, Kamal Kishore Pathak, Vikas Pandey

Article 102960

Article preview 

Special Section on Nanomaterials

Research article ☐ Abstract only

Generation forecasting employing Deep Recurrent Neural Network with metaheuristic feature selection methodology for Renewable energy power plants

Abdulaziz Alshammari

Article 102968

Article preview 

Special Section on Microbial & Enzymatic Bioelectrochemical Systems

Research article ☐ Abstract only

Transitional trimetallic alloy embedded polyacrylamide hydrogel derived nitrogen-doped carbon air-cathode for bioenergy generation in microbial fuel cell

Simran Kaur Dhillon, Patit Paban Kundu

Article 103001

Article preview 

Sustainable Energy Technologies and Assessments

Submit your article



All content on this site: Copyright © 2024 Elsevier B.V., its licensors, and contributors. All rights are reserved, including those for text and data mining, AI training, and similar technologies. For all open access content, the Creative Commons licensing terms apply.

